

Fall 2020

Nuclear Thermal Rocket Engine with a Toroidal Aerospike Nozzle

Kyle Stewart
San Jose State University

Follow this and additional works at: https://scholarworks.sjsu.edu/etd_theses

Recommended Citation

Stewart, Kyle, "Nuclear Thermal Rocket Engine with a Toroidal Aerospike Nozzle" (2020). *Master's Theses*. 5163.

DOI: <https://doi.org/10.31979/etd.qwkv-999v>

https://scholarworks.sjsu.edu/etd_theses/5163

This Thesis is brought to you for free and open access by the Master's Theses and Graduate Research at SJSU ScholarWorks. It has been accepted for inclusion in Master's Theses by an authorized administrator of SJSU ScholarWorks. For more information, please contact scholarworks@sjsu.edu.

NUCLEAR THERMAL ROCKET ENGINE WITH A TOROIDAL AEROSPIKE NOZZLE

A Thesis

Presented to

The Faculty of the Department of Aerospace Engineering

San José State University

In Partial Fulfillment

of the Requirements of the Degree

Master of Science in Aerospace Engineering

by

Kyle J. Stewart

December 2020

© 2020

Kyle J. Stewart

ALL RIGHTS RESERVED

The Designated Thesis Committee Approved the Thesis Titled
NUCLEAR THERMAL ROCKET ENGINE WITH A TOROIDAL AEROSPIKE NOZZLE

by

Kyle J. Stewart

APPROVED FOR THE DEPARTMENT OF AEROSPACE ENGINEERING

SAN JOSÉ STATE UNIVERSITY

December 2020

Periklis Papadopoulos, Ph. D.

Department of Aerospace Engineering

Fabrizio Vergine, Ph. D.

Department of Aerospace Engineering

Maria Chierichetti, Ph. D.

Department of Aerospace Engineering

Brian Andrade, M.S.

Department of Aerospace Engineering

ABSTRACT

NUCLEAR THERMAL ROCKET ENGINE WITH A TOROIDAL AEROSPIKE NOZZLE

by Kyle J. Stewart

This thesis describes the coupling of a nuclear thermal rocket engine with a toroidal aerospike nozzle. The coupling of the two systems consists of two phases. The first of these phases begin with top-level systems and subsystems analysis and design of the new engine. The second phase is the analysis and characterization of the major engine systems through the use of computational fluid dynamics analysis. With the coupling of the nuclear thermal rocket engine with the aerospike nozzle, the new system will be known as the Nuclear Thermal Propulsion System. Due to the uniqueness of coupling a nuclear thermal rocket engine with a toroidal aerospike nozzle, the traditional nuclear thermal rocket engine design of a cylindrical nuclear reactor had to be abandoned. This change stems from the need for cooling of the aerospike nozzle and the inherent difficulty that the nozzle support structure would cause for such a system. The redesigned nuclear reactor is known as the annulus reactor system because the nuclear core is fashioned into a hoop shape to allow for the integration with an aerospike nozzle specially configured for use with the hoop core. This innovative design represents a significant improvement over conventional chemical rockets in both the areas of providing energy for thrust generation as well as the expansion and expulsion of the exhausting propellant.

ACKNOWLEDGMENTS

I would like to express significant appreciation to Dr. Papadopoulos for his assistance and invaluable guidance throughout the research and development process related to the writing of this thesis. Additionally, I would like to express gratitude to my colleague Jordan Pollard for his assistance with the development of the content related to this thesis. I would like to express my sincere appreciation to the aerospace engineering department at San Jose State University for facilitating our work. Lastly, I would like to thank, my family. Without their support, I would have never been able to complete this thesis or pursue my dreams.

TABLE OF CONTENTS

List of Tables	viii
List of Figures	x
1 Project Motivation	1
1.1 The Dilemma	1
1.2 The Reason for Concern	3
1.3 Project Objective.....	3
1.4 Methodology	4
1.5 Background.....	5
1.5.1 Theory of Nuclear Thermal Propulsion	5
1.5.2 Theory of an Aerospike Nozzle	8
1.5.3 The U.S. Nuclear Thermal Engine Development	12
1.5.4 Historical Perspective of the Development of Nuclear Fuels.....	14
2 Theoretical Purpose	21
2.1 Mission Profile.....	21
2.2 System Decomposition	28
2.3 System Integration	30
2.4 System Architecture.....	32
3 Propellant Feed System.....	40
3.1 Propellant Feed System Profile.....	40
3.2 Propellant Feed System Decomposition	43
3.3 Propellant Feed System Integration	44
3.4 Propellant Feed System Architecture.....	46
4 Annulus Reactor System.....	50
4.1 Annulus Reactor System Profile.....	50
4.2 Annulus Reactor System Decomposition	57
4.3 Annulus Reactor System Integration	58
4.4 Annulus Reactor System Architecture.....	59
5 Nozzle System	63
5.1 Nozzle System Profile.....	63
5.2 Nozzle System Decomposition	66
5.3 Nozzle System Integration.....	68
5.4 Nozzle System Architecture	69
6 Coolant System	73
6.1 Coolant System Profile	73
6.2 Coolant System Decomposition.....	79

6.3	Coolant System Integration.....	81
6.4	Coolant System Architecture	82
7	Analysis of the Annulus Reactor and Nozzle Systems.....	87
7.1	Annulus Reactor System Analysis.....	87
7.2	Nozzle System Analysis	104
8	Discussion.....	116
9	Future work.....	118
10	Conclusion	119
	Bibliography	120
	Appendix A.....	125

LIST OF TABLES

Table 1.	Nozzle Expansion Conditions.....	9
Table 2.	Various Types of Reactor Tests.....	15
Table 3.	Fuel Types and Corresponding Operating Temperatures.....	18
Table 4.	Nuclear Fuel Geometries	18
Table 5.	Apollo Spacecrafts Mass Distribution	24
Table 6.	The Change in Velocity for Phases One Through Three.....	25
Table 7.	Mission Profile Statistics	27
Table 8.	Interface Connections for the Major Systems of the NTPS.....	33
Table 9.	Interface Connections for the Annulus Engine System.....	35
Table 10.	Interface Connections for the Propellant System.....	36
Table 11.	Inputs and Outputs of the N ² Diagram	48
Table 12.	Annular Reactor Design Data	55
Table 13.	Inputs and Outputs of the Annulus Reactor System N ² Diagram.....	61
Table 14.	Inputs and Outputs of the Nozzle System N ² Diagram.....	71
Table 15.	Inputs and Outputs of the Coolant System N ² Diagram	84
Table 16.	Annulus Reactor Analysis: General Settings.....	91
Table 17.	Annulus Reactor Analysis: Boundary Conditions	92
Table 18.	Annulus Reactor Analysis: Solution Methods.....	92
Table 19.	Annulus Reactor Physics: Solution initialization	93
Table 20.	Annulus Reactor System Simulation Test #1	94
Table 21.	Annulus Reactor System Simulation Test #2	96

Table 22.	Annulus Reactor System Simulation Test #3	97
Table 23.	Annulus Reactor System Simulation Test #4	98
Table 24.	Annulus Reactor System Simulation Test #5	99
Table 25.	Annulus Reactor System Simulation Test #6	100
Table 26.	Annulus Reactor System Simulation Test #7	100
Table 27.	Annulus Reactor System Simulation Test #8	101
Table 28.	The Test Aerospike Dimensions	107
Table 29.	Nozzle System Analysis: General Settings	109
Table 30.	Nozzle System Analysis: Boundary Conditions	110
Table 31.	Nozzle System Analysis: Solution Methods	110
Table 32.	Nozzle System Analysis: Solution Initialization	111
Table 33.	Appx. Symbol Nomenclature	125
Table 34.	Appx. Greek Symbols Nomenclature	125
Table 35.	Appx. Subscripts and Superscripts Nomenclature	126
Table 36.	Appx. Acronym Nomenclature	127

LIST OF FIGURES

Fig. 1.	The liquid-drop model.	5
Fig. 2.	The cascade effect of a fission reaction.	6
Fig. 3.	Slip-line expansion of an aerospike nozzle.....	10
Fig. 4.	Performance comparison between an aerospike and bell nozzle.....	11
Fig. 5.	Hexagonal fuel elements are arranged in a cylindrical core.	15
Fig. 6.	Various fuel endurance levels for a given operating temperature.	16
Fig. 7.	The Soviet Union’s modular twisted-ribbon reactor.	20
Fig. 8.	The theoretical mission phases.	22
Fig. 9.	The modules and stages of the Apollo spacecraft.....	23
Fig. 10.	Illustration of phase one's Hohman transfer.	25
Fig. 11.	Nuclear Thermal Propulsion System decomposition from Tier 0-3.....	28
Fig. 12.	System decomposition of the annulus engine system from Tier 3-5.....	29
Fig. 13.	System decomposition of the propellant system from Tier 3-5.....	30
Fig. 14.	The integration diagram for the main systems of the NTPS.....	31
Fig. 15.	N ² diagram of the major systems of the NTPS.....	33
Fig. 16.	N ² diagram of the subsystems of the annulus engine system.	34
Fig. 17.	N ² diagram of the subsystems of the propellant system.	36
Fig. 18.	The overall flowchart for the NTPS, part 1.	38
Fig. 19.	The overall flowchart for the NTPS, part 2.	39
Fig. 20.	Diagram of two propellant feed system configurations.....	41
Fig. 21.	Decomposition of the propellant feed system.....	44

Fig. 22.	Integration diagram of the propellant feed system.	46
Fig. 23.	The N ² diagram for the propellant feed system.	47
Fig. 24.	Flowchart of the propellant feed system.	49
Fig. 25.	Annulus reactor fuel rod cut-a-way.	51
Fig. 26.	The layout of the annulus reactor core.	52
Fig. 27.	Fuel puck orientation within the engine.	54
Fig. 28.	Tri-carbide nuclear fuel puck.	56
Fig. 29.	The annulus reactor decomposition.	58
Fig. 30.	Integration diagram for the annulus reactor system.	59
Fig. 31.	N ² diagram for the annulus reactor system.	60
Fig. 32.	Flowchart for the annulus reactor system.	62
Fig. 33.	A 2-dimensional contour plot of a nozzle aerospike.	64
Fig. 34.	A 2-dimensional contour plot of a nozzle spike with cowling.	65
Fig. 35.	The nozzle support structure system.	66
Fig. 36.	Decomposition of the nozzle system.	67
Fig. 37.	The integration diagram of the three primary nozzle systems.	69
Fig. 38.	N ² diagram for the nozzle system.	70
Fig. 39.	Flowchart for the nozzle system.	72
Fig. 40.	Coolant system directional flow diagram of the nozzle system.	76
Fig. 41.	Coolant system directional flow diagram of the annulus reactor system.	77
Fig. 42.	Coolant system directional flow diagram of the propellant feed system.	79
Fig. 43.	The coolant system decomposition.	80

Fig. 44.	The integration diagram of the coolant system.....	82
Fig. 45.	N ² diagram for the coolant system.....	83
Fig. 46.	Operational flowchart diagram of the coolant system.	86
Fig. 47.	Single tri-carbide fuel puck planar approximation.	88
Fig. 48.	The structured meshing of the tri-carbide fuel puck.....	90
Fig. 49.	Temperature profile from puck #3 test #1.	94
Fig. 50.	Total pressure profile from puck #3 test #1.....	95
Fig. 51.	Velocity profile from puck #3 test #1.	95
Fig. 52.	Temperature contours of full puck assembly.....	101
Fig. 53.	Temperature contour for non-separated configuration.	102
Fig. 54.	Annulus reactor system test #1-2 result comparison.	103
Fig. 55.	Annulus reactor system test #3-5 result comparison.	103
Fig. 56.	Annulus reactor system test #6-8 result comparison.	104
Fig. 57.	Close up view of meshing topology.....	108
Fig. 58.	Overall spike and flow field meshing topology.....	108
Fig. 59.	Mach contours with a chamber pressure of 4.1 MPa at 1 atm.....	112
Fig. 60.	Anatomy of the aerospike exhaust plume.....	112
Fig. 61.	Mach contours with a chamber pressure of 5.1 MPa at 1 atm.....	113
Fig. 62.	Temperature contours of the nozzle exhaust plume.	113
Fig. 63.	Mach contours in near-vacuum conditions at a P _c of 5.1 MPa.	114

1 PROJECT MOTIVATION

1.1 The Dilemma

Modern high thrust rocket engines all operate using the same fundamental principles. These principles hold whether the engine is a solid rocket motor or a cryogenic bi-propellant engine. The first of these principles is that the engines use combustion to add energy into the fluids contained in the rocket engine's plenum. By adding energy, the pressure of the fluid begins to increase rapidly, allowing the now highly pressurized fluid to escape through an expanding bell-shaped nozzle. The fluid expands and accelerates, giving the rocket thrust, hence completing the other fundamental principle. By the laws of physics and thermodynamics, these fundamental principles of these engines have reached their maximum potential. The technological plateau is due to the critical parameter in the study of these kinds of propulsion systems. This parameter is known as specific impulse, which is the thrust per unit of the propellant flow weight. The ideal specific impulse is proportional to the plenum temperature divided by the fluid's molecular weight, leaving the plenum. Therefore, to produce higher ideal specific impulse values, the engine must have a high operating temperature coupled with the exhausting fluid's low molecular weight. The solid rocket motors and cryogenic bi-propellant engines all have relatively the same combustion chamber temperatures. The similar chamber temperatures are because of the limiting factor of the material used for the construction of the combustion chamber. With the combustion chamber temperature relatively fixed due to the material, a reasonable way to produce a higher ideal specific

impulse is by reducing the molecular weight of the exhausting fluid. Thus, combustion as a means of adding energy into a fluid to achieve a higher specific impulse has reached the upper limit of around mid 400 sec. Therefore, combustion is a chemical reaction that will always result in a total product that is heavier than the initial reactance. The removal of combustion as a means of adding energy to a fluid is the logical way to reduce the molecular weight. The second fundamental principle is using the conservation of momentum by exhausting the high-pressure fluid out through an expanding bell-shaped nozzle. The bell-shaped nozzle works under the principle of area ratio, specifically the area ratio of the throat and nozzle exit. The desired altitude at which the engine is to produce optimum thrust will determine the area ratio. Thus, an engine using a bell-shaped nozzle will only produce optimum thrust at a single altitude, which will only occur for a moment in the use of the engine [1].

Consequently, during the vast majority of the time the engine is in use, it is not performing optimally. The underperforming will cause the overuse of fuel, which results in a lower mass that can be lifted by said engine. For the engine to produce optimum thrust, the nozzle must constantly adjust for the changing atmospheric pressure. Therefore, specific impulse is directly related to the exhausting fluid's molecular weight and indirectly related to thrust optimization. This connection affirms that molecular weight and thrust optimization are the limiting factors in achieving higher specific impulse in high thrust rocket engines [1], [2].

1.2 The Reason for Concern

The previously discussed fundamental problems have become some of the core reasons humanity is limited to only increasing the size of rockets to lift more and go further into space. Understanding these fundamental problems and the forces driving them will allow for solutions to be designed and tested. Solving the problem of the molecular weight of the exhausting fluid and ensuring that optimum thrust is produced throughout the flight will dramatically influence what humanity can accomplish in space.

1.3 Project Objective

The objective of this thesis is the coupling of a nuclear thermal rocket engine with a toroidal aerospike nozzle. The coupling of these systems will allow the fast transportation of more mass between celestial bodies by over two times that of current designs. This project will consist of two main sections: the first is the design of the systems and subsystems for the new engine; the second is be the analysis and refinement of the major systems of the engine. With the coupling of the nuclear thermal rocket engine with the aerospike nozzle, the new system will be known as the Nuclear Thermal Propulsion System (NTPS). Because of the uniqueness of coupling a nuclear thermal rocket engine (NTR) with a toroidal aerospike nozzle, the traditional NTR design of a cylindrical nuclear core had to be abandon. The abandonment stems from the need for cooling of the aerospike nozzle from the nuclear core's exhausting gas. The redesigned nuclear core is known as a hoop core because the nuclear core is fashioned into a hoop shape to allow for the cooling of the nozzle. This innovative design, as well as other systems, will be described in the subsequent chapters.

1.4 Methodology

The reasoning for using a nuclear thermal propulsion system to solve limiting factors of modern high thrust rocket engines is that the engine's fundamental principles are different. For the nuclear thermal engine, the energy is added to the plenum's fluid by forcing the fluid through the fission reacting core. Because there are no chemical reactions taking place, the exhausting fluid's molecular weight remains the same. By using a low molecular weight propellant, the resulting exhausting fluid will have the same low molecular weight. Thus, increasing the specific impulse of the propulsion system while maintaining a high thrust output. Coupling the nuclear thermal rocket engine with the toroidal aerospike nozzle will cause the engine to be at optimum thrust throughout the engines' use. By doing so, it will significantly increase performance and further increase the propulsion system's specific impulse. The analysis of this new potential design for a high thrust rocket engine will be first constructing the central systems and the corresponding subsystems of the new nuclear thermal propulsion system. With the design of the systems completed, the systems' operation and the theoretical aspects of the new propulsion system will be verified. This verification process will be conducted through the use of computational fluid dynamics. When verified, this nuclear thermal propulsion system will be the first engine to utilize the nuclear reactor's new hoop core design. This design will also be the first nuclear thermal propulsion system to employ an active cooling system for a toroidal aerospike nozzle.

1.5 Background

1.5.1 Theory of Nuclear Thermal Propulsion

The principles behind a nuclear thermal propulsion system are relatively straightforward. Thermal energy is produced in the nuclear reactor core as the core undergoes the process of nuclear fission. The process of fission is when an unstable heavy atom is split into two lighter atoms. Niels Bohr and John A. Wheeler developed a theoretical model of this kind of reaction, the “Liquid-drop model,” as in Fig. 1[3].

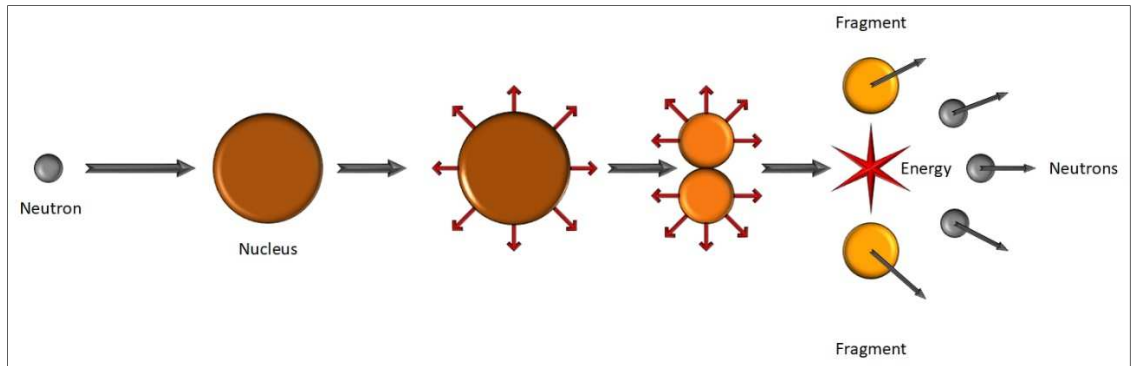


Fig. 1. The liquid-drop model.

When the heavy atom is split into the two lighter atoms, the fragmented nuclei will produce a large amount of energy and extra neutrons. The extra neutrons are the catalyst for the fission reaction. Thus, with each reaction, more neutrons are produced than were used in the reaction. This abundance of neutrons causes a cascade effect of fission reactions, as shown in Fig. 2. This cascade allows for the thermal energy of the reaction to heat the propellant [3].

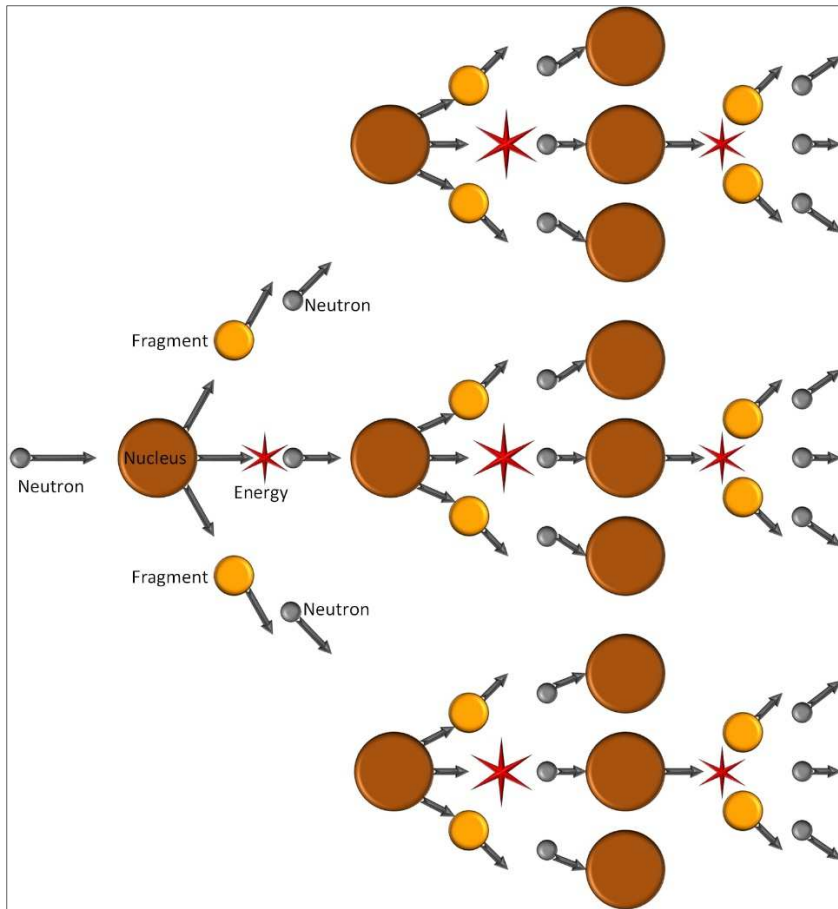


Fig. 2. The cascade effect of a fission reaction.

As the propellant is heated, the particles within the fluid obtain a large amount of kinetic energy. The manifestation of the energy is a random thermal motion, which causes the propellant fluid to expand rapidly through the nozzle. As a result of this rapidly expanding fluid, the outward pressure of the fluid increases. The propellant fluid is then allowed to expand through a nozzle. The nozzle acts as a converter by transforming the random thermal energy of the propellant fluid into a single direction of flow. By directing the rapidly expanding fluid out of the engine uniformly, a force is

created on the engine. This force acts in the opposite direction of the propellant flow, thus moving the engine forward and creating thrust [2].

A way for analyzing how well an engine can produce that thrust is needed. This parameter of engine performance is known as a specific impulse (I_{SP}). Specific impulse is a measurement of the thrust produced by a unit of propellant flow weight. With specific impulse being a measurement over a set time interval, this parameter's standard units are seconds. Through thermodynamics, specific impulse is comparable to the chamber temperature divided by the exhausting fluid's molecular weight, T_c/M_w . This relationship between chamber temperature and molecular weight, drives the specific impulse of an engine, as shown in the following equations [1], [2], [4].

$$I_{SP} = \frac{V_{eg}}{g_0} \quad (1)$$

$$V_{eg} = V_e + \frac{(P_e - P_a) \cdot A_e}{\dot{m}} \quad (2)$$

$$V_e = \sqrt{\left(\frac{2\gamma}{\gamma - 1} \cdot \frac{\mathbb{R}}{M_w} \cdot T_c \cdot \left[1 \cdot \left(\frac{P_e}{P_c} \right)^{\frac{\gamma-1}{\gamma}} \right] \right)} \quad (3)$$

$$\dot{m} = \frac{P_c \cdot A^*}{\sqrt{\left(\frac{\mathbb{R}}{M_w} \cdot T_c \right)}} \cdot \sqrt{\gamma \cdot \left(\frac{1 + \gamma}{2} \right)^{\frac{1+\gamma}{1-\gamma}}} \quad (4)$$

$$P_i = \rho_i \cdot \frac{\mathbb{R} \cdot T_i}{M_{w_i}} \quad (5)$$

To further understand how the major driving parameters of specific impulse are the quantity T_c/M_w , the definition of specific impulse must be expanded by substituting

Equation 2 into Equation 1. At this expansion, the link between the driving parameters and specific impulse is still unclear. By substituting Equations 3 and 4 into Equation 2, along with substituting Equation 5 into the expanded Equation of 1 for the pressure terms, making the majority of terms in the specific impulse equation to be T_c/M_w .

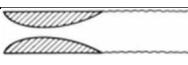
Therefore, the major driving parameters of the specific impulse are T_c/M_w , making an approximation of specific impulse from these terms becomes all the more evident, as shown in Equation 6.

$$I_{SP} = \frac{\left[\frac{(\rho_c \cdot \mathbb{R} \cdot \frac{T_c}{M_w}) \cdot A^*}{\sqrt{\mathbb{R} \cdot \frac{T_c}{M_w}}} \sqrt{\gamma \cdot \left(\frac{1+\gamma}{2}\right)^{\frac{1+\gamma}{1-\gamma}}} \right] \cdot \left[\sqrt{\left(\frac{2 \cdot \gamma}{\gamma-1}\right) \cdot \mathbb{R} \cdot \frac{T_c}{M_w}} \cdot \left[1 \cdot \frac{(\rho_e \cdot \mathbb{R} \cdot \frac{T_e}{M_w})^{\frac{\gamma-1}{\gamma}}}{(\rho_c \cdot \mathbb{R} \cdot \frac{T_c}{M_w})} \right] \right]^{\frac{\gamma-1}{\gamma}}}{g_0 \cdot \left[\frac{(\rho_c \cdot \mathbb{R} \cdot \frac{T_c}{M_w}) \cdot A^*}{\sqrt{\mathbb{R} \cdot \frac{T_c}{M_w}}} \sqrt{\gamma \cdot \left(\frac{1+\gamma}{2}\right)^{\frac{1+\gamma}{1-\gamma}}} \right]} \quad (6)$$

1.5.2 Theory of an Aerospike Nozzle

In the development of the rocket engine, the limitation of the convergent-divergent nozzle begins to appear. This limitation appears as the engine travels through changing regions of pressure. This pressure change causes the relationship between the pressure at the exit and the ambient pressure to change. To achieve the optimum thrust from a given engine, the exit and ambient pressure must be equal. When they are not equal, the exit pressure must adjust to the ambient conditions by forming shock waves resulting in a loss in performance, as seen in Table 1. Table 1 is based on an image from “Advanced Spacecraft Propulsion A.E. 267 (Class Notes)” [1], [4].

Table 1
Nozzle Expansion Conditions

Nozzle Expansion	Condition Cases
	$p_e < p_a \rightarrow$ Over-expanded
	$p_e > p_a \rightarrow$ Under-expanded
	$p_e = p_a \rightarrow$ Perfectly expanded
$p_e = \text{Exit Pressure}$ $p_a = \text{Ambient Pressure}$	

This performance loss can be resolved by constantly adjusting the area ratio between the engine's throat and exit. In terms of a convergent-divergent nozzle, the constant adjusting proves to be quite problematic. A relatively simple solution is to allow the exhausting fluid to be bounded by a free-to-move slip-line expansion surface. The slip-line boundary acts as a variable area ratio nozzle, which allows the nozzle to adjust to the changing ambient pressure, as illustrated in Fig. 3. Slip-line bounded nozzles are known as altitude compensating or aerospike nozzles [1].

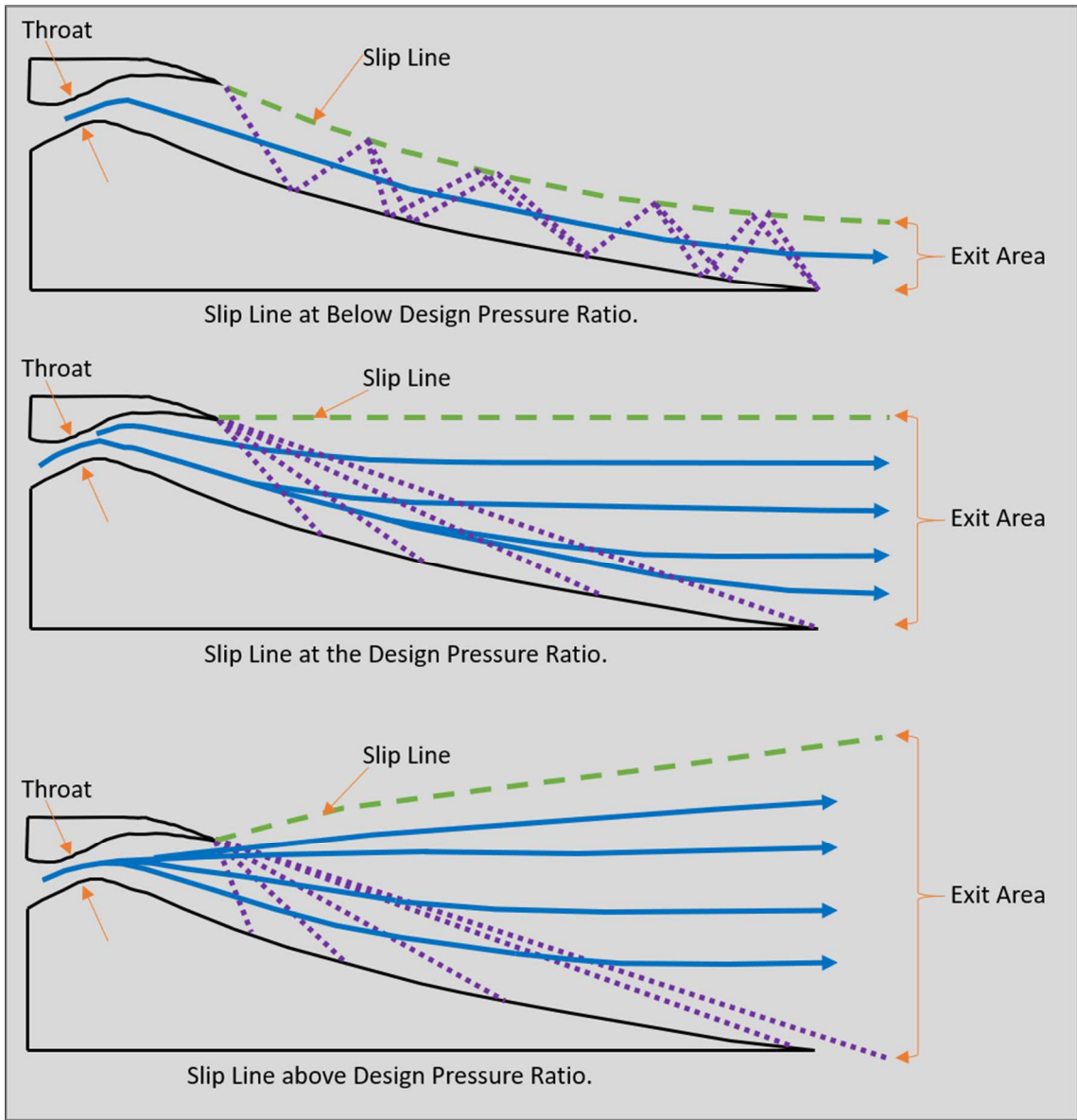


Fig. 3. Slip-line expansion of an aerospike nozzle.

This ability to operate at optimum thrust regardless of the ambient pressure gives an engine using an aerospike nozzle a significant advantage over those with the conventional convergent-divergent nozzle. An illustration of the convergent-divergent nozzle's

performance loss versus an aerospike nozzle is in Fig. 4, based on an illustration from “Modern Engineering For Design of Liquid-Propellant Rockets Engines.” [1], [2].

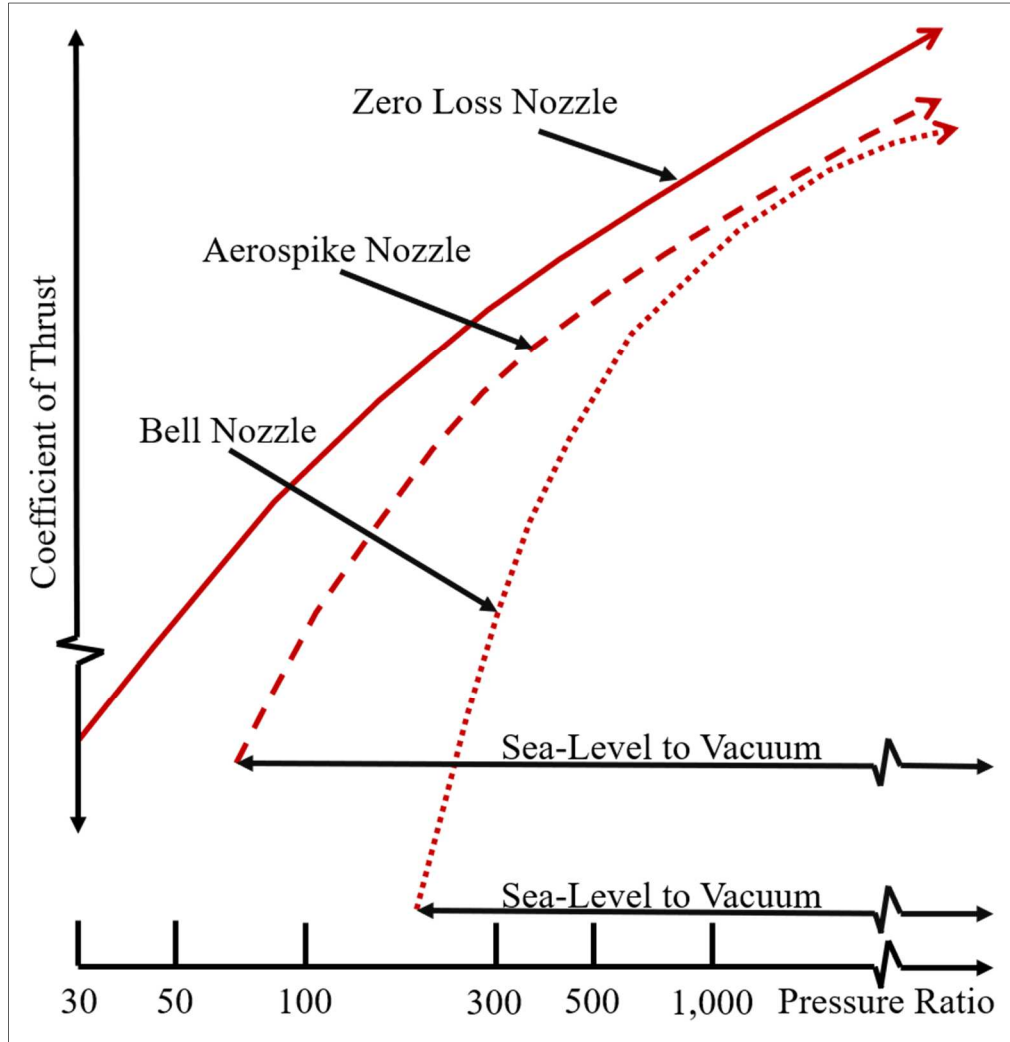


Fig. 4. Performance comparison between an aerospike and bell nozzle.

The added time at optimum thrust gives an engine the ability to use less fuel during the flight. The most significant advantage is the increase in the overall average of thrust

and specific impulse that will be produced by the engine during flight. As a result, the engine can lift larger payloads without any other changes to the craft [1], [2].

1.5.3 The U.S. Nuclear Thermal Engine Development

The notion of using nuclear thermal power as a means to produce thrust for rockets was first suggested in 1945 by Theodore Von Karman. At the time, the USAF Scientific Advisory Board deemed that the manufacturing of such a system was not needed. The rejection was due to the lack of fissionable materials and insufficient need for a system of that kind. In 1954, Von Karman once more consulted with the USAF Scientific Advisory Board to develop nuclear thermal propulsion systems. By this time, the U.S. had an ample supply of fissionable material and a new need for high thrust and high specific impulse rocket engines. This increase in fissionable material was due to the new need for better ICBMs. A year later, the advisory board gives the go-ahead to begin developing nuclear thermal propulsion systems. Thus, the establishment of the Rover Project in November 1955. The Los Alamos Scientific Laboratory would conduct the project. Los Alamos chose the hydrogen cooled, solid core reactor design over the several other conceptually studied thermal propulsion systems. The reduction in the urgency for a new kind of engine caused the first test of the nuclear thermal rocket engine in 1959. The first reactor was named the Kiwi-A, for it was named after the flightless bird from New Zealand because, like the bird, the reactor was never intended to fly [5], [6]. The Kiwi-A successfully ran for five minutes at 70 megawatts. Even though the reactor test was considered successful, the Kiwi-A did sustain structural damage to the carbide fuel particles. This damage was determined to be caused by the excessive core internal

temperatures of 2,683K. A year later, they tested the Kiwi-A's second iteration with newly improved fuel-elements in the core, eliminating damage from the core temperatures. With the second successful test by the Rover Project team, their successful research got NASA and the Atomic Energy Commission's attention. Later that year, they formed the Space Nuclear Propulsion Office. With the new backing, the Kiwi-A3 was able to be tested mere months after the second Kiwi test. The Kiwi-A3 was able to operate at 100 megawatts for five minutes. This test was the end of the Kiwi-A series, and the series was proof of the principle of all the previous research. With three hugely successful tests, the newly formed Space Nuclear Propulsion Office enlisted some of the biggest names in space research and development. In 1961, the Office contracted Aerojet-General, Westinghouse Electric Corporation, and The Lockheed Corporation to develop the Rover Program's next phase. The next phase of reactors was named Kiwi-B series; this series's second engine was the first engine to run using liquid hydrogen. All the previous engines were using gaseous hydrogen; this change proved to be very advantageous, for the Kiwi-B1B was able to run for a brief time at 900 megawatts. The next major milestone came in the next series of reactors under the name of Nuclear Engine for Rocket Vehicle Application (NERVA). The successful demonstration in 1964 of the first NERVA reactor known as NRX-A2 was operated at half and full power, all in the same run. The NRX-A2 also tested out at a vacuum specific impulse of 760s. For comparison, in that same year, the Titan rocket was the most advanced rocket of the day, but it could only produce a vacuum specific impulse of 308s. The stunning outcome helped to drive the development of nuclear engines further. Between 1964 to 1972 saw

significant advancements in the program. At the zenith of the program, saw the production of two nuclear engines that showcased the potential of this technology. The first of these two is the Phoebus-2A engine. The Phoebus boasts the title of the most powerful nuclear rocket reactor ever constructed; at only 80% power, the reactor produced 4,000 megawatts of thermal power, with a thrust output of 1,123 kN. The second of the two was the Pewee engine. The Pewee was able to have the highest core temperature of 2,750K, which also produced the highest specific impulse of 845s. This specific impulse made for the Pewee to be the most power-dense nuclear engine ever built. Despite all these incredible achievements, in January of 1973, the Rover Nuclear Rocket Program was terminated due to the changing national priorities of the time. Thus, ending the United States nuclear propulsion development [6]–[8].

1.5.4 Historical Perspective of the Development of Nuclear Fuels

By the termination in 1973 of the Rover and NERVA Programs, over 20 different prototype engines were ground tested. The 20-prototypes ranged from reactor tests to full-on prototype engines, shown in Table 2, based on a table from “Experience Gained from the Space Nuclear Rocket Program (Rover).” The most significant change over this span of test engines was the development and refinement of the reactor’s fuel elements. The fuel elements first used were of a highly enriched uranium oxide in a graphite matrix. This fuel type was formed into solid plates allowing the hydrogen propellant to pass over them. Gradually the fuel type evolved into an all carbide fuel matrix. The all carbide fuel consisted of a solid solution made of enriched uranium, zirconium, and carbon. The hexagonal tubes of the full carbide fuel would include an arrangement of the tubes in the

form of a cylindrical core, as seen in Fig. 5, which is based on images from “Experience Gained from the Space Nuclear Rocket Program (Rover)” [6], [9], [10].

Table 2
Various Types of Reactor Tests

		1959	1960	1961	1962	1963	1964	1965	1966	1967	1968	1969
Nerva Program	NRX Reactor Tests						NRX-A1 NRX-A2	NRX-A3	NRX-A5	NRX-A6		
	Engine Tests								NRX/EST		XECF	XE
Rover Research	Kiwi	KIWI-A KIWI-A2	KIWI-A3		KIWI-B1A KIWI-B4A	KIWI-B1B	KIWI-B4D KIWI-B4E					
	Phoebus						PHOEBUS-1A		PHOEBUS-1B		PHOEBUS-2A	
	Pewee										PEWEE	

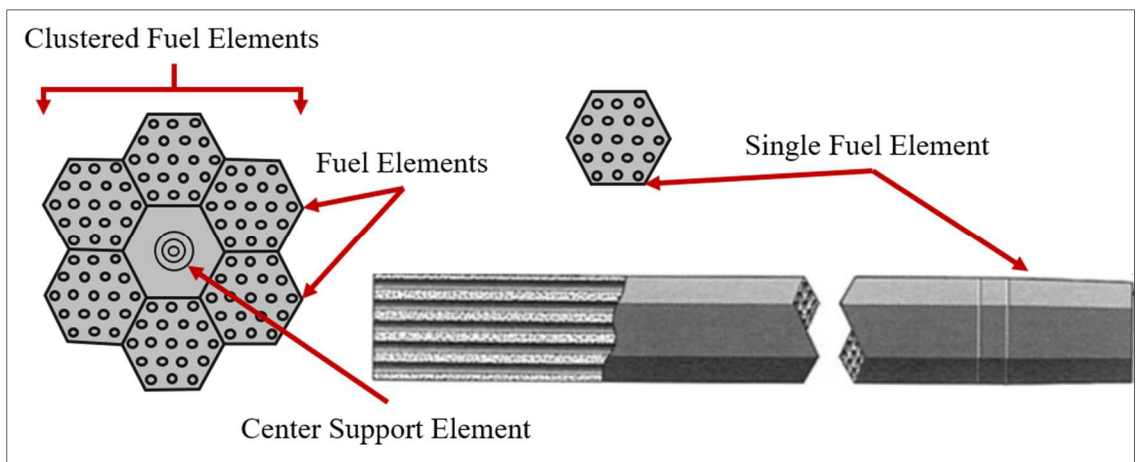


Fig. 5. Hexagonal fuel elements are arranged in a cylindrical core.

The all carbide fuel matrix was first tested in the NF-1 engine, meaning the two-record holding engines of the Phoebus-2A and the Pewee both use the less durable uranium dicarbide fuel. If the research had been allowed to continue, both the Pewee's and Phoebus's records would have quickly faded. For each iteration of fuel elements, the program attempted to raise the endurance at the operating temperature to obtain an ever higher thrust and specific impulse, as seen in Fig. 6, which is based on images from "Summary of Historical Solid Core Nuclear Thermal Propulsion Fuels" [6], [10], [11].

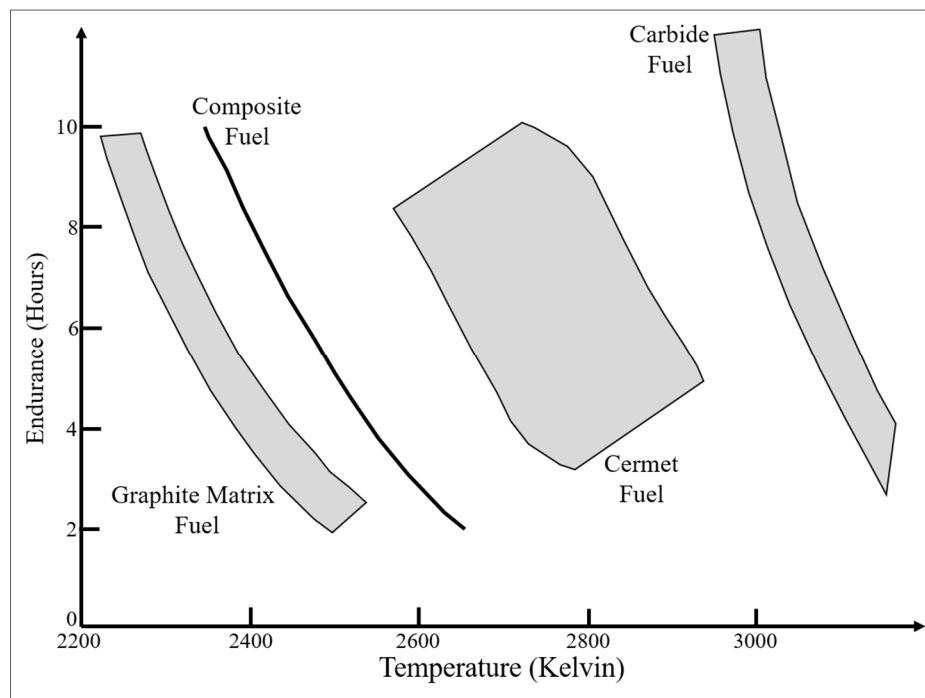


Fig. 6. Various fuel endurance levels for a given operating temperature.

While the United States Rover Program was underway, the Soviet Union was busy developing its nuclear thermal propulsion program. The Soviet Union's approach was to focus on a modular style of the reactor. The modular style of the reactor used what is

known as heterogeneous fuel. This form of fuel did not use a moderating material, thereby allowing the reactor to use a small amount of uranium as well as only having a single section of the reactor operating at high temperatures. Between 1962-1963, observed the completion of the confirmation testing on the modular reactor, which had an exit temperature of 3,000 K. With the success of this reactor, the Soviet nuclear propulsion program focused on reducing the size of the reactor and maximizing the exhaust propellant temperature. In order to do so, the soviets needed to re-think the heterogeneous fuel style of their reactors. The new fuel would need to be optimized for heat transfer while maintaining stability at the maximum operating temperature. Similar to the United States, the Soviet Union tested many configurations and permutations of fuel geometries and compositions. The significant differences between the two programs were that the soviet program continued into the early 1990s, some 20 years more than the United States. With technology advancement, the soviet program was able to achieve its desired fuel. This new kind of fuel is known as Ternary Carbides or Tri-carbides. As the name suggests, the fuel is comprised of three main elements, uranium, zirconium, and carbon, with later models adding tantalum for even higher operating temperatures. This progression of the fuel types and their corresponding operating temperature is shown in Table 3. Table 3 is a variation of a table from “Summary of Historical Solid Core Nuclear Thermal Propulsion Fuels” [10], [11].

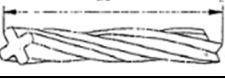
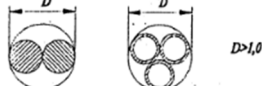
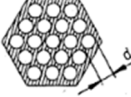
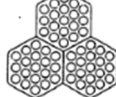
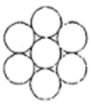
Table 3
Fuel Types and Corresponding Operating Temperatures

	Type of Fuel	Uranium Density ($\frac{g}{cm^3}$)	Maximum Operating Temperature (K)
Carbide	(U, Zr) C, C (U, Zr) C (U, Zr, Nb) C (U, Zr, Ta) C	≤ 2.5	2,500 3,300 3,500 3,700
Carbonitride	(U, Zr) C, N	6-8	3,100
CERMET Carbonitride	(U, Zr) C, N-W	≤ 6.5	2,900

With a fuel that can sustain the high operating temperatures, the soviet program needed to develop a way of maximizing the heat transfer between the fuel and propellant fluid. Thus, the development of the so-called “twisted-ribbon” geometry fuel. This geometry allowed for the best heat transfer while maintaining structural integrity at the high operating temperatures. A comparison of both the Soviet Union and the United States fuel geometries are in Table 4, which is a variation of a table from “Summary of Historical Solid Core Nuclear Thermal Propulsion Fuels.” The new fuel ribbons would be bundled into a group at the bottom of a fuel rod assembly. The reactor would then consist

of dozens of fuel rod assemblies, upholding the original design of their original reactor's modular style, as seen in Fig. 7 [10].

Table 4
Nuclear Fuel Geometries

Type of Fuel Element	General Form	Cross-section Dimensions (mm)	Fuel Arrangement & Composition
Ribbon		 $b > 1,0$ $D > 1,6$ $S = 30$	 $(Zr, U)C$ $(Zr, Nb, U)C$ $(Zr, U)C+C$ $(Zr, U, N)C$
Rod		 $b > 1,4$ $D > 1,8$ $S = 60$	 $(Nb, U)C$ $(Zr, Nb, U)C$ $(Zr, U)C+C$ $(Zr, U, N)C$
		 $D > 1,0$	 $(Zr, U)C$ $(Zr, Nb, U)C$ $(Zr, U)C+C$ $(Zr, U, N)C$
Prismatic Block		 $d > 1,0$	 $(Zr, U)C$ $(Zr, Nb, U)C$ $(Zr, U)C+C$ $(Zr, U, N)C$
Plate		 $b > 1,0$	 $(Zr, U)C$ $(Zr, Nb, U)C$ $(Zr, U)C+C$ $(Zr, U, N)C$
Spherical		 $D = 1-10 \text{ mm}$	 $(Zr, U)C$ $(Zr, U)N$ $(Zr, U, N)C$

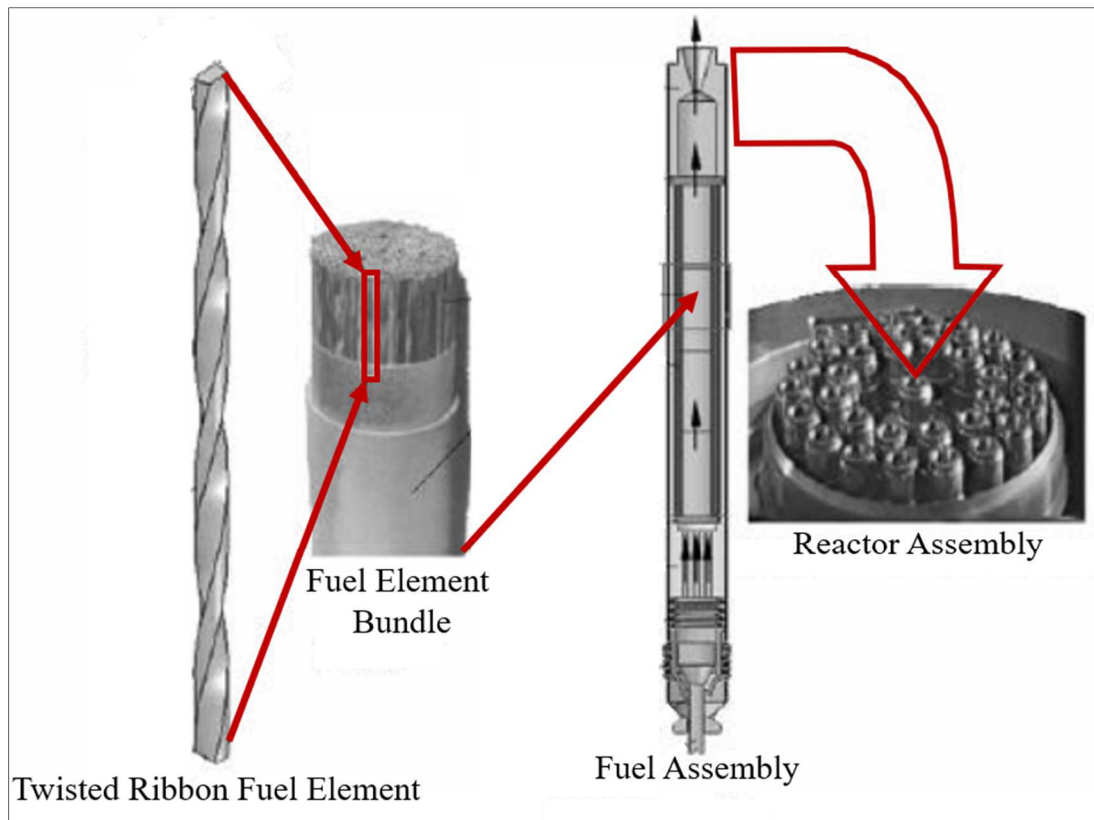


Fig. 7. The Soviet Union's modular twisted-ribbon reactor.

The new twisted-Ribbon reactor was fitted to an engine assembly in 1985 to form the RD-0410. The RD-0410 was the most successful nuclear engine developed by the Soviet Union. The engine operated for 1 hour at a core temperature of 3,500-3,700K. With such a high operating temperature, the RD-0410 achieved a specific impulse of 910s, giving it a 1.8 thrust to weight ratio. After this very successful engine test, the Soviet Union shifted its focus on the development of not only a slightly larger engine but one that could produce 20 times the thrust of the RD-0410. As the Soviet Union collapsed, so did the drive to develop nuclear thermal propulsion systems further, with the program being terminated in 1994 [10], [12], [13].

2 THEORETICAL PURPOSE

The purpose will act as a basis of the coupling of the previously discussed system of the NTR and aerospike nozzle. By having a definitive objective in mind, the design can converge on a final solution while simultaneously demonstrating the utility of the design. Therefore, throughout the remainder of this thesis, the analysis and design of the new Nuclear Thermal Propulsion System will be driven by a theoretical crewed mission to the surface of Mars.

2.1 Mission Profile

The mission that will be used to analyze and design the new Nuclear Thermal Propulsion System will be a short-term crewed mission to Mars. This mission will consist of three main phases, a departure from Low Earth Orbit (LEO) to the surface of Mars, launch from the Martian surface to Low Mars Orbit, and Low Mars Orbit back to Low Earth Orbit, as illustrated in Fig. 8.

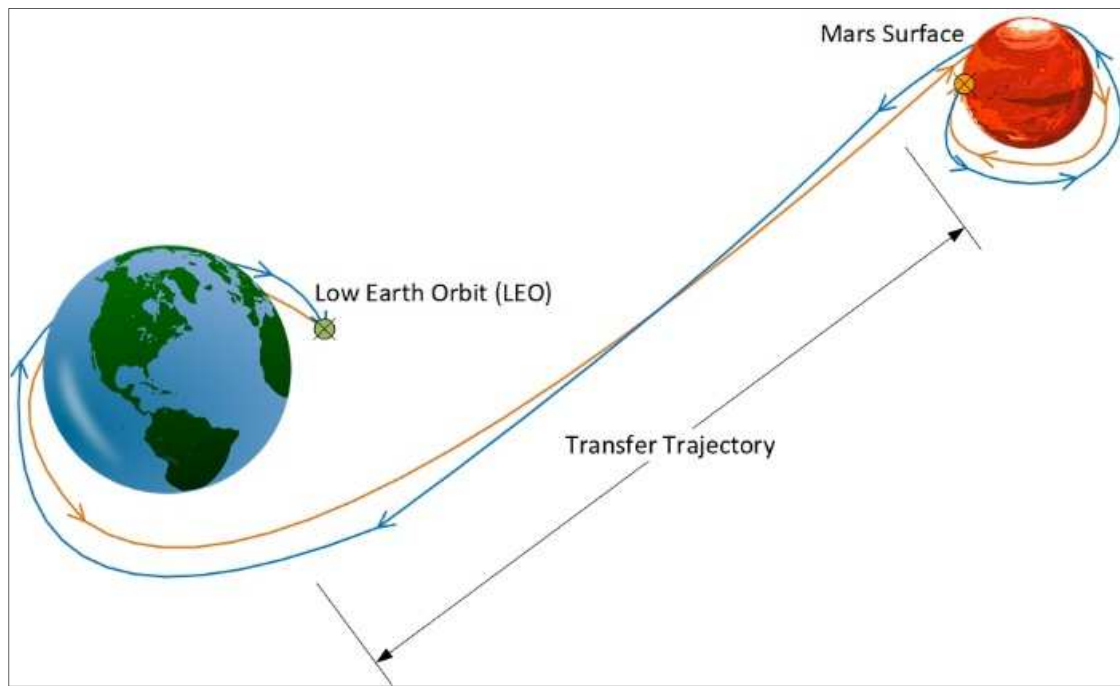


Fig. 8. The theoretical mission phases.

The purpose of starting and ending the mission in LEO is that it would be improbable in the near foreseeable future for a Nuclear Thermal Propulsion System to be allowed to operate within Earth's atmosphere. This improbability is due to a concern of a malfunction, which would cause a widespread dispersion of highly enriched nuclear material throughout Earth's atmosphere. In order to begin designing this mission, a spacecraft is needed, more specifically, the overall mass of a spacecraft that is capable of housing several astronauts to and from Mars. Because there have been no manned missions to Mars as of yet, the only referenceable spacecraft is that of the Apollo Program. Thus, a spacecraft of this mass would be appropriate for a short-term mission to Mars and back [14], [15].

The Apollo Spacecraft consisted of three separate vehicles, the Command, Service, and Lunar modules; an illustration of these three modules is in Fig. 9, based on illustrations from “History NASA” and “Apollo Spacecraft Diagram.” At the end of a particular phase of that mission, the corresponding module would be discarded to reduce mass. This method works well for a short duration flight, such as Apollo. However, the mission to Mars will be far from a short duration flight, with the estimation for flight duration being a minimum of a year. Therefore, the proposed mission will have a theoretical spacecraft with a dry mass equivalent to that of the Apollo Spacecraft's mass that left the Moons orbit with the addition of 40% of the descent stage's dry mass[16], [17].

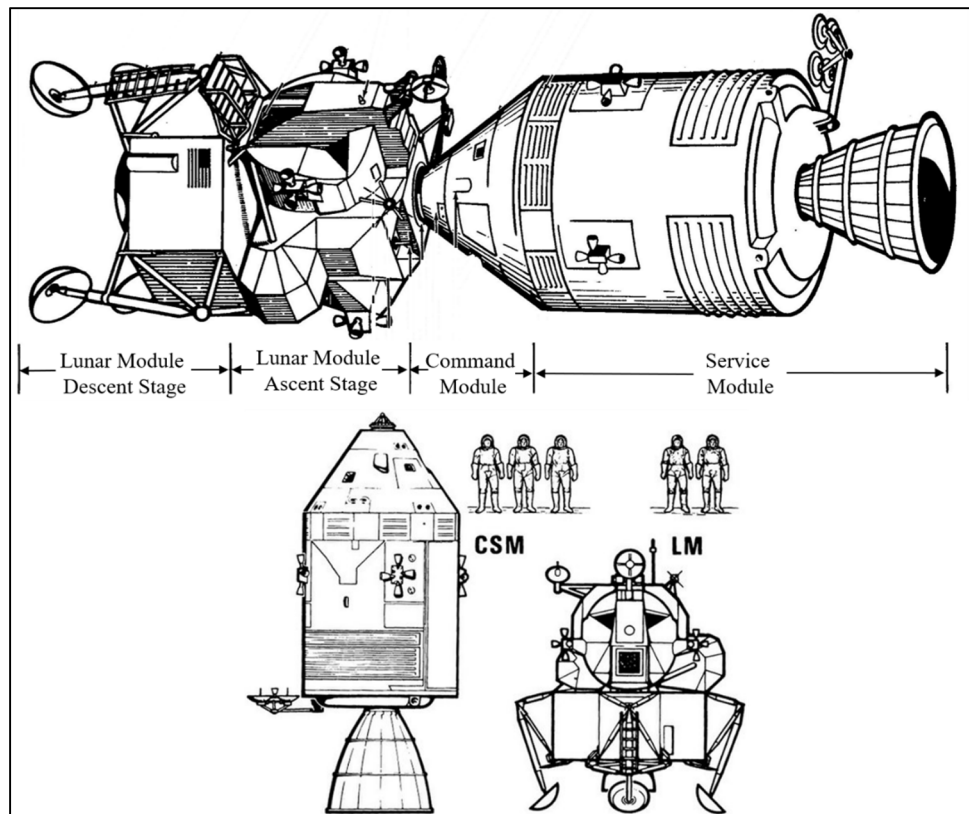


Fig. 9. The modules and stages of the Apollo spacecraft.

The addition of 40% of the descent stage is to compensate for the much longer flight duration. The decomposition of the Apollo Spacecraft mass is in Table 5. Thus, yielding a theoretical spacecraft on its return from Mars has a dry mass of 20,664.3 kg [15], [18], [19].

Table 5
Apollo Spacecrafts Mass Distribution

Module	Mass
Command Module	Dry Mass: 5,837.05 kg
Service Module	Total Mass: 24,519.5 kg
	Fuel Mass: 18,413.7 kg
	Dry Mass: 6,105.81 kg
Lunar Module	Total Mass: 16,437.144 kg
Lunar Ascent Stage	Dry Mass: 4,796.966 kg
Lunar Descent Stage	Fuel Mass: 8,836.98 kg
Lunar Descent Stage	Dry Mass: 2,803.2 kg

By having the mass of the theoretical spacecraft defined, the next major step in constructing the mission profile is to establish appropriate changes in velocity for each of the three phases of the mission. The change in velocity for phases 1 and 3 vary significantly from year to year and from month to month. An appropriate change in velocity was chosen for these phases to maintain focus on the propulsion system's design and system layout. The change in velocity for each phase relates to the amount of fuel mass needed to complete it. The use of a special kind of transfer trajectory known as a Hohman Transfer will reduce fuel mass that would be needed. An illustration of phase one's Hohman Transfer is in Fig. 10; phase three's transfer trajectory will be similar. Since the orbits of both Earth and Mars are not circular and do not lay on the same plane

in space, the change in velocity for phase 3 is slightly more significant, as seen in Table 6 [19]–[23].

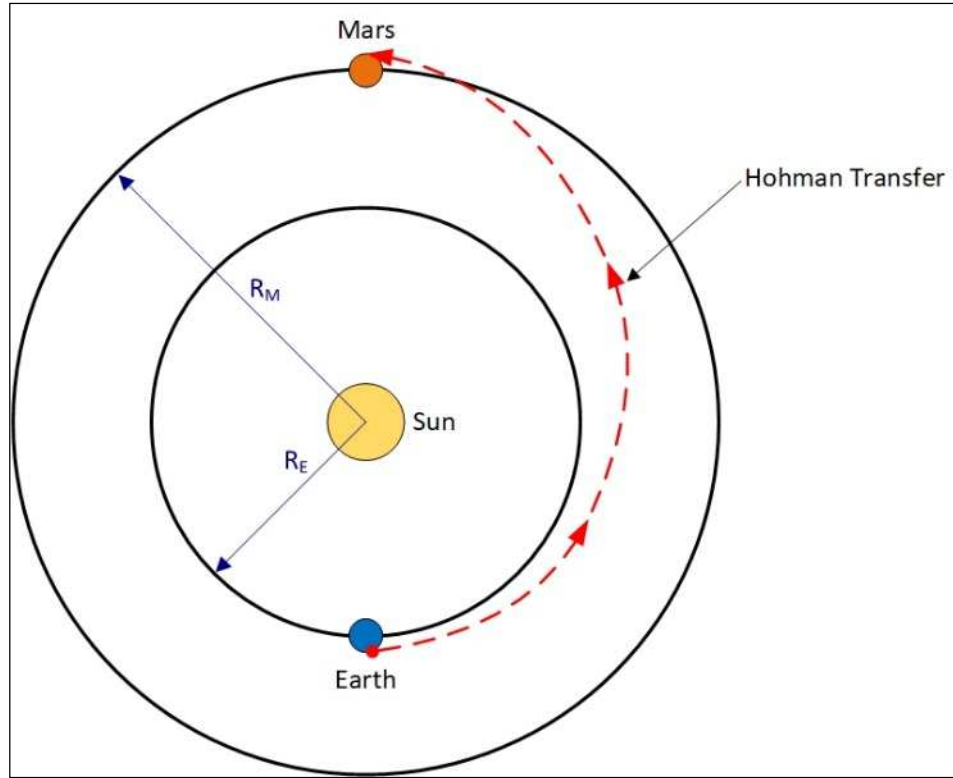


Fig. 10. Illustration of phase one's Hohman transfer.

Table 6
The Change in Velocity for Phases One Through Three

Phase Number	Starting and Ending Location	Change in Velocity (Δv)
Phase #1	Low Earth Orbit to the Surface of Mars	5.296 km/s
Phase #2	The Surface of Mars to Mars Orbit	5.578 km/s
Phase #3	Mars Orbit to Low Earth Orbit	5.5937 km/s

Therefore, with the establishment of the change in velocity for each phase, the mass per-phase can be estimated. The mass estimation is performed using Equations 7 through

(10). The estimation starts with phase three, for the reasoning that the ending payload mass, the theoretical spacecraft, is already known. By estimating an I_{sp} and deadweight ratio, the initial and propellant mass can be established for that phase's requirements. Both the I_{sp} value and deadweight ratio were estimated from characteristic tables on nuclear propulsion engines from "Elements of Propulsion, Gas Turbines and Rockets" on pages 173 and 180. For phase two, the initial mass of phase three becomes the payload mass for phase two. With the establishment of the initial mass of phase two, it is then used to establish the initial mass for phase one. Thus, starting with the last phase, the spacecraft's overall starting mass, including propellant, can be established. The specifications for each of the phases are listed in Table 7 [1], [2], [20], [22].

$$c = I_{SP} \cdot g_0 \quad (7)$$

$$MR = e^{\left(\frac{\Delta V}{c}\right)} \text{ "In vacuum only."} \quad (8)$$

$$MR = e^{\left(\frac{\Delta V + g_m \cdot t_{po}}{c}\right)} \text{ "On Mars only."} \quad (9)$$

$$MR = \frac{M_o}{M_{pl} + \delta \cdot M_o} \quad (10)$$

By establishing the starting mass for this mission, the feasibility factor for a mission of this magnitude is the last step in constructing the mission profile. Two methods of verifying this mission's feasibility should be considered, the first being the feasibility of getting a spacecraft of 226,735 kg into LEO. The second is the ability of a Nuclear Thermal Propulsion System, having the capability to lift the spacecraft off Mars and into Mars orbit. The feasibility of getting a spacecraft of such mass into LEO is entirely possible. Currently, the best launch system for a spacecraft of this size would be the

Falcon Heavy by SpaceX. With this launch system, the spacecraft's entire assembly could be in LEO with just four launches. In comparison, both the future Starship by SpaceX and the Space Launch System by NASA will be able to assemble the spacecraft in just two launches, with the Starship's estimated mass in LEO for the Mars mission ranging around 200,000 kg plus depending on the intended payload [1], [24]–[26].

Table 7
Mission Profile Statistics

Phase Number	Starting and Ending Location	Mission Data
Phase #1	Low Earth Orbit to Surface of Mars	$\Delta v = 5.296$ km/s
		$I_{sp} = 1000$ sec.
		$\delta = 0.1$
		MR = 1.71576
		$M_{pl} = 109,475$ kg
		$M_p = 94,586.6$ kg
Phase #2	The Surface of Mars to Mars Orbit	$M_o = 226,735$ kg
		$\Delta v = 5.578$ km/s
		$I_{sp} = 1000$ sec.
		$\delta = 0.1$
		$g_m = 3.71$ m/s ²
		$t_{bo} = 300$ sec.
		MR = 1.97795
		$M_{pl} = 44,400.2$ kg
$M_p = 54,127.3$ kg		
Phase #3	Mars Orbit to Low Earth Orbit	$M_o = 109,475$ kg
		$\Delta v = 5.5937$ km/s
		$I_{sp} = 1000$ sec.
		$\delta = 0.1$
		MR = 1.76863
		$M_{pl} = 20,664$ kg
$M_p = 19,296.2$ kg		
		$M_o = 44,400.2$ kg

The feasibility of a Nuclear Thermal Propulsion System being able to lift the spacecraft off Mars must now be verified. The confirmation of the feasibility was through the examination of the United States Space Nuclear Propulsion Office's most powerful engine, the Phoebus-2A. The Phoebus-2A was able to produce a thrust of 1,123 kN; by

knowing the initial mass for phase two, thus, establishing a Martian thrust to weight ratio of 2.76497, confirming that a Nuclear Thermal Propulsion System can complete this theoretical mission profile to and from Mars [6], [27].

2.2 System Decomposition

By completing the mission profile and verifying its feasibility, the focus can shift back to solving the fundamental problem with modern high thrust rocket engines. The solution being proposed is that of the coupling of a nuclear thermal rocket engine with the adaptability of an altitude compensating toroidal aerospike nozzle. A decomposition of the new proposed system is needed to begin the process of coupling these two very complex systems. The decomposition of the new Nuclear Thermal Propulsion System into systems and subsystems will allow for a more defined outline of the systems that will need to be analyzed and reconfigured. All while allowing the systems that are not directly related to the propulsion system to remain as standard systems. The new Nuclear Thermal Propulsion System is first broken down into three tiers, as seen in Fig. 11 [28]–[30].

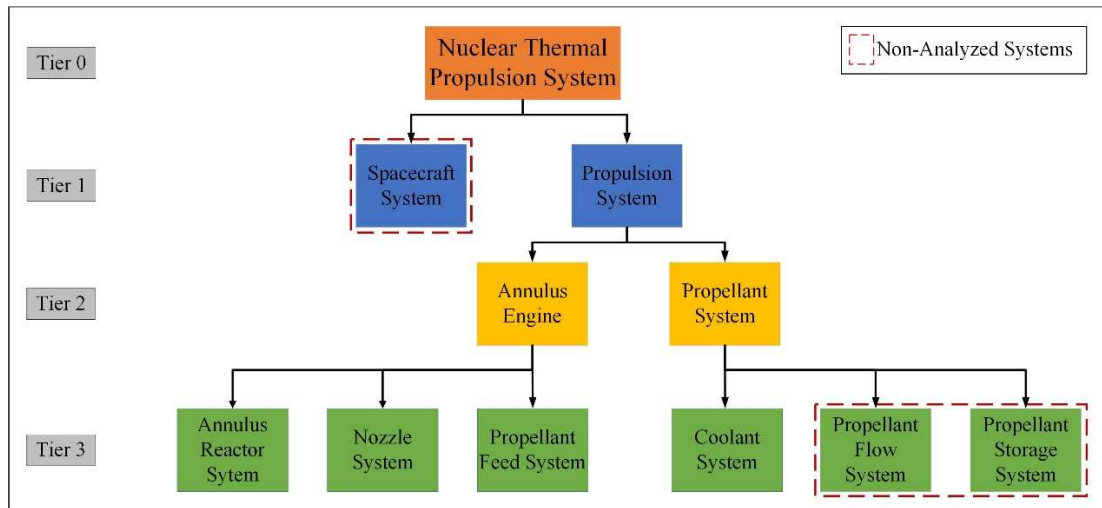


Fig. 11. Nuclear Thermal Propulsion System decomposition from Tier 0-3.

The systems and subsystems indicated above, in Fig. 11, comprise the main components of the Nuclear Thermal Propulsion System. The systems and subsystem outlined in red signify ones that will remain relatively unchanged by the new design. As shown in Fig. 11, the two central systems that will need to be considered in designing the new Nuclear Thermal Propulsion System will be the annulus engine and propellant system. With these two central systems playing such a vital role in the development and design of the new Nuclear Thermal Propulsion System, each system is further broken down into the systems and subsystems which comprise them, as seen in Fig. 12 and 13 [1], [2], [6], [30].

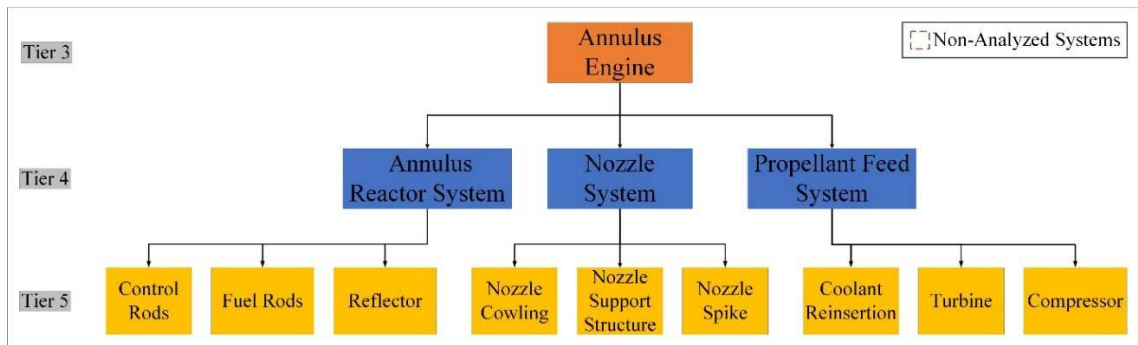


Fig. 12. System decomposition of the annulus engine system from Tier 3-5.

The annulus engine is comprised of three primary systems with nine subsystems, as seen in Fig. 12. In comparison, the propellant system, seen in Fig. 13, has three primary systems with only five subsystems. Both the annulus engine and propellant systems are of equal importance. The equal importance is due to the high degree of integration among all the systems and subsystems within the analyzed primary systems [1], [2], [30].

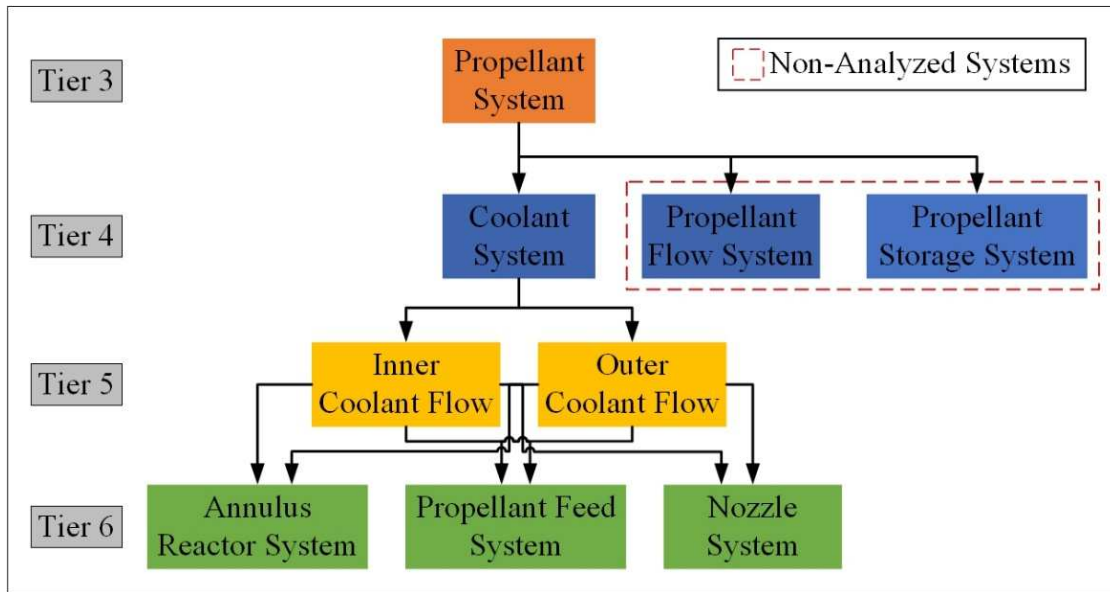


Fig. 13. System decomposition of the propellant system from Tier 3-5.

2.3 System Integration

The high degree of integration between the systems and subsystems of both the annulus engine system and the propellant system can begin to be understood through the illustration shown in Fig. 14. This illustration shows that the two most influential systems of the whole propulsion system are the coolant and reactor systems. Understanding the Nuclear Thermal Propulsion System's main driving forces and the integration between them allows for each system to be designed and refined on an individual basis. This individual refinement allows for a much higher level of complexity and refinement in the overall combined system. However, the systems' refinement can only be accomplished if the symbiotic relationship between them is well understood and defined. Thus, the definition of these relationships is through the illustration in Fig. 14. Through the now

defined relationship of each main system, the overall system architecture for the new propulsion system can be constructed [6], [29], [30].

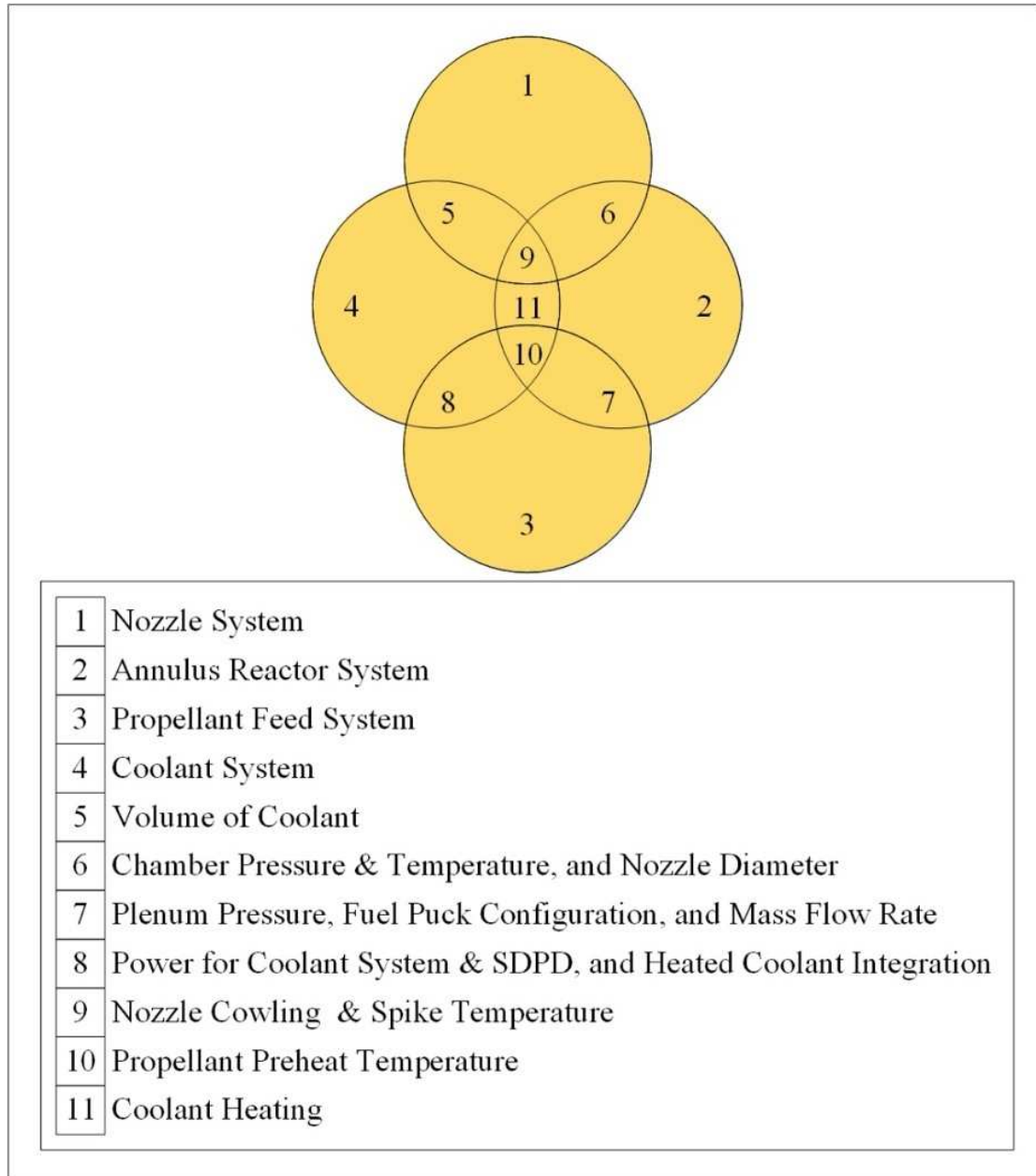


Fig. 14. The integration diagram for the main systems of the NTPS.

2.4 System Architecture

The construction of the Nuclear Thermal Propulsion System's architecture, like many other stages of design, is split into sub-sections. By dividing the architectural layout, the different aspects of the overall system can be better understood. The first aspect of the Nuclear Thermal Propulsion System that needs to be understood is the exchange between the major systems and subsystems. An N^2 diagram was constructed to convey how exchanges occur between the Propulsion System's major systems and the spacecraft. The illustration of the N^2 diagram in Fig. 15 is of the analyzed systems in Tier 1 and 2 from Fig. 11. This N^2 diagram illustrates the input and output of each system relative to each other. Table 8 houses the list of the inputs and outputs that correspond to Fig. 15. By understanding this first level of exchange between the main systems, the next logical step would be to conduct the same illustration on both the annulus engine and propellant system [2], [6], [30].

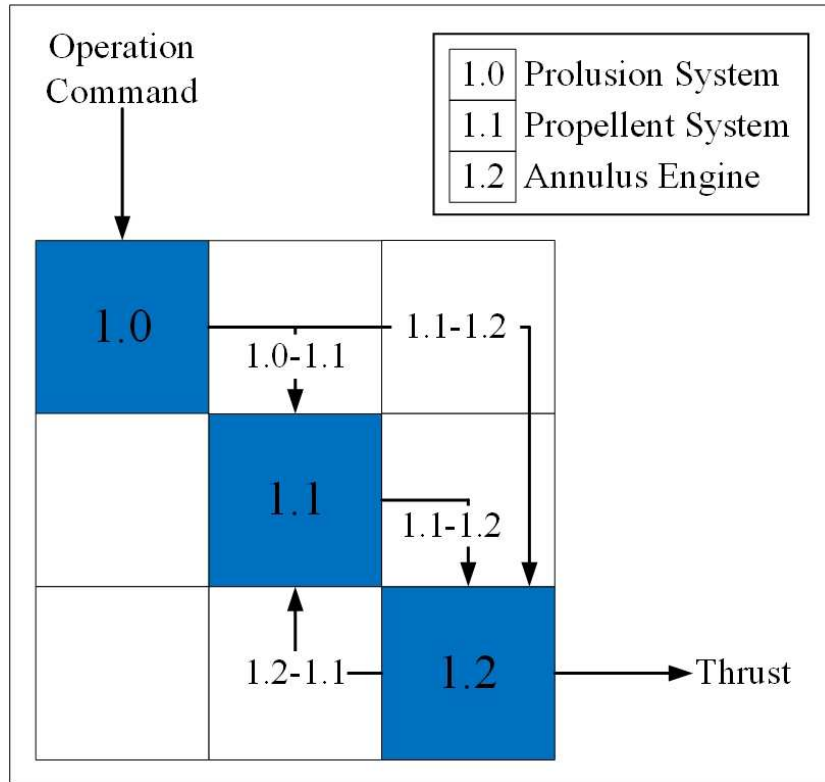


Fig. 15. N² diagram of the major systems of the NTPS.

Table 8
Interface Connections for the Major Systems of the NTPS

The direction of Input & Output	Performed Operation
In → 1.0	Operation Command
1.0 → 1.1	Flow Rate Control for Both Coolant and Propellant Systems
1.0 → 1.2	Start or Regulates Core Temperature
1.1 → 1.2	Propellant & Coolant Flow
1.2 → Out	Thrust
1.2 → 1.1	Power for Coolant & Propellant Feed System

The illustration of the annulus engine system interface connections in Fig. 16 corresponds to the inputs and outputs of Tier 3 and 4 from Fig. 12. With the annulus

engine system containing the reactor, the interactions between the other systems dramatically increase. The increase in interactions is due to the annulus reactor system being the Nuclear Thermal Propulsion System's proverbial heart. Thus, the annulus engine system will have more input and outputs amongst itself and other systems and subsystems at this level of analysis; hence the interface connections in Table 9 are more numerous than for the other N^2 diagrams [2], [6], [30].

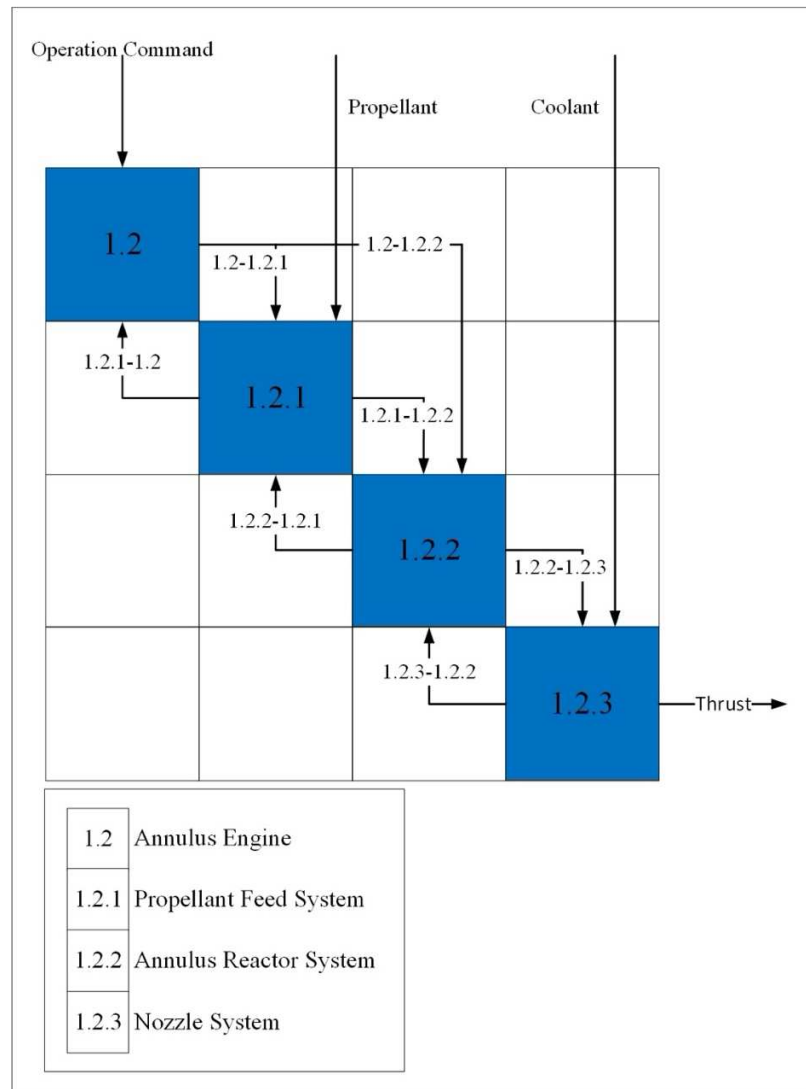


Fig. 16. N^2 diagram of the subsystems of the annulus engine system.

Table 9
Interface Connections for the Annulus Engine System

The direction of Input & Output	Performed Operation
In → 1.2	Operation Command
1.2 → 1.2.1	Flow Rate Regulation of Propellant & Coolant
1.2 → 1.2.2	Reactor Temperature Control
In → 1.2.1	Coolant Flow
In → 1.2.1	Propellant Flow
1.2.1 → 1.2.2	Pressurized Preheat Propellant
1.2.1 → 1.2	Coolant Pump Power
1.2.2 → 1.2.3	Pressurized High-Temperature Propellant
1.2.2 → 1.2.1	High-Temperature Coolant
In → 1.2.3	Coolant Flow
1.2.3 → <i>Out</i>	Thrust
1.2.3 → 1.2.2	Preheated Coolant

The illustration of the propellant system's interface connections in Fig. 17 and Table 10 are the inputs and outputs for the analyzed systems on Tier 3-5 of Fig. 13. The propellant system at this resolution of analysis has only one primary system and two subsystems that are included in Fig. 17. Both the coolant system and propellant flow system directly interface with the annulus engine system. With both the coolant system and propellant flow system using hydrogen gas to perform their operations thus, the only distinguishing factor between the two systems is the flow rate and location for which they deliver the fluid [1], [2], [6], [30].

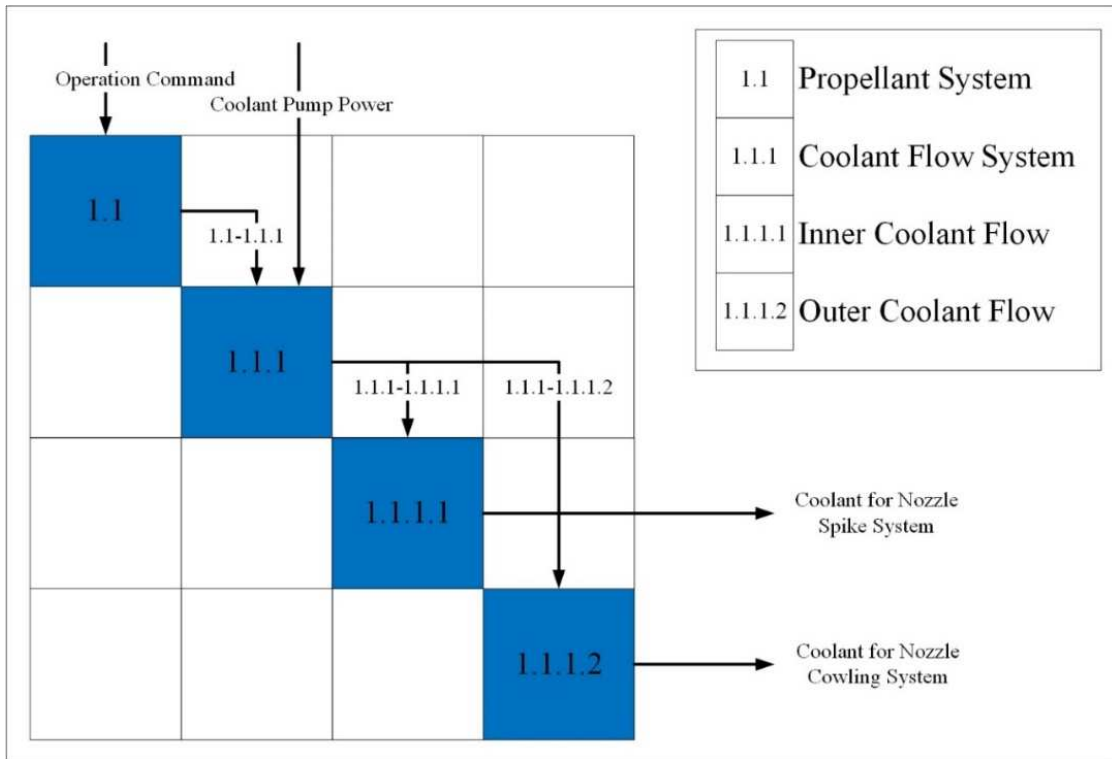


Fig. 17. N² diagram of the subsystems of the propellant system.

Table 10
Interface Connections for the Propellant System

The direction of Input & Output	Performed Operation
<i>In</i> → 1.1	Operation Command
1.1 → 1.1.1	Operation Command
<i>In</i> → 1.1.1	Coolant Pump Power
1.1.1 → 1.1.1.1	Coolant Flow Rate Command
1.1.1.1 → Out	Coolant for Nozzle Spike System
1.1.1 → 1.1.1.2	Coolant Flow Rate Command
1.1.1.2 → Out	Coolant for Nozzle Cowling System

The second significant aspect of constructing the system architecture for the Nuclear Thermal Propulsion System was the design of an overall flowchart. A flowchart

illustrates how each system and subsystem interact with each other during operation. The overall flowchart for the Propulsion System, as seen in Fig. 18 and 19, is comprised of the primary systems from Fig. 11. The advantage of constructing the flowchart based on the spacecraft decomposition diagram is that various systems can be analyzed individually. This individual analysis allows for the Propulsion System's flow to be logically arranged while better understanding the interaction between each of the primary and sub-primary systems. By setting an architectural foundation of the overall system, will yield a finer analysis and design of the four primary systems and their subsequent subsystems. Therefore, the propulsion system's flowchart is to act as a guide for the systems architecture in the following chapters [2], [6], [12], [29], [30].

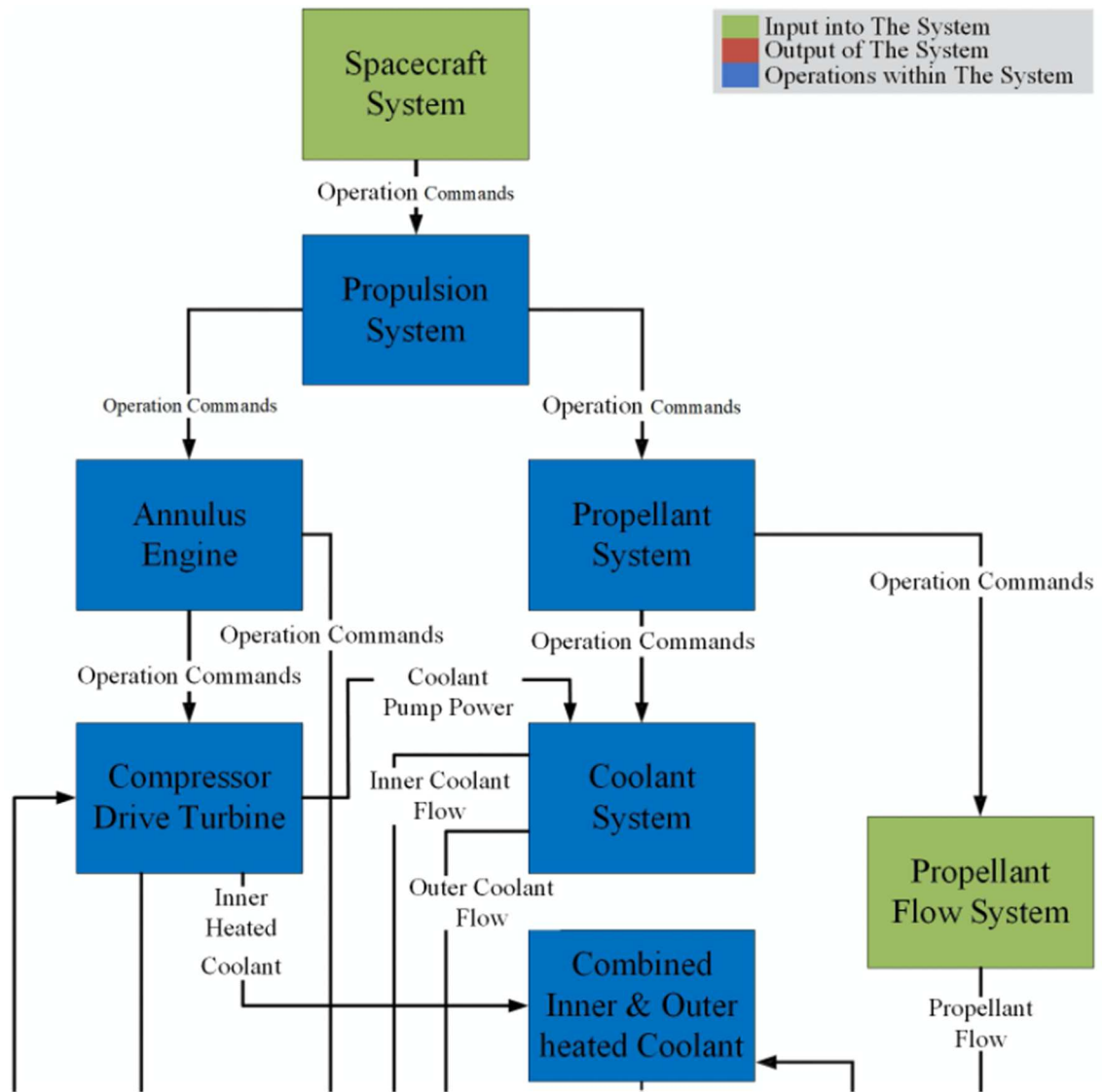


Fig. 18. The overall flowchart for the NTPS, part 1.

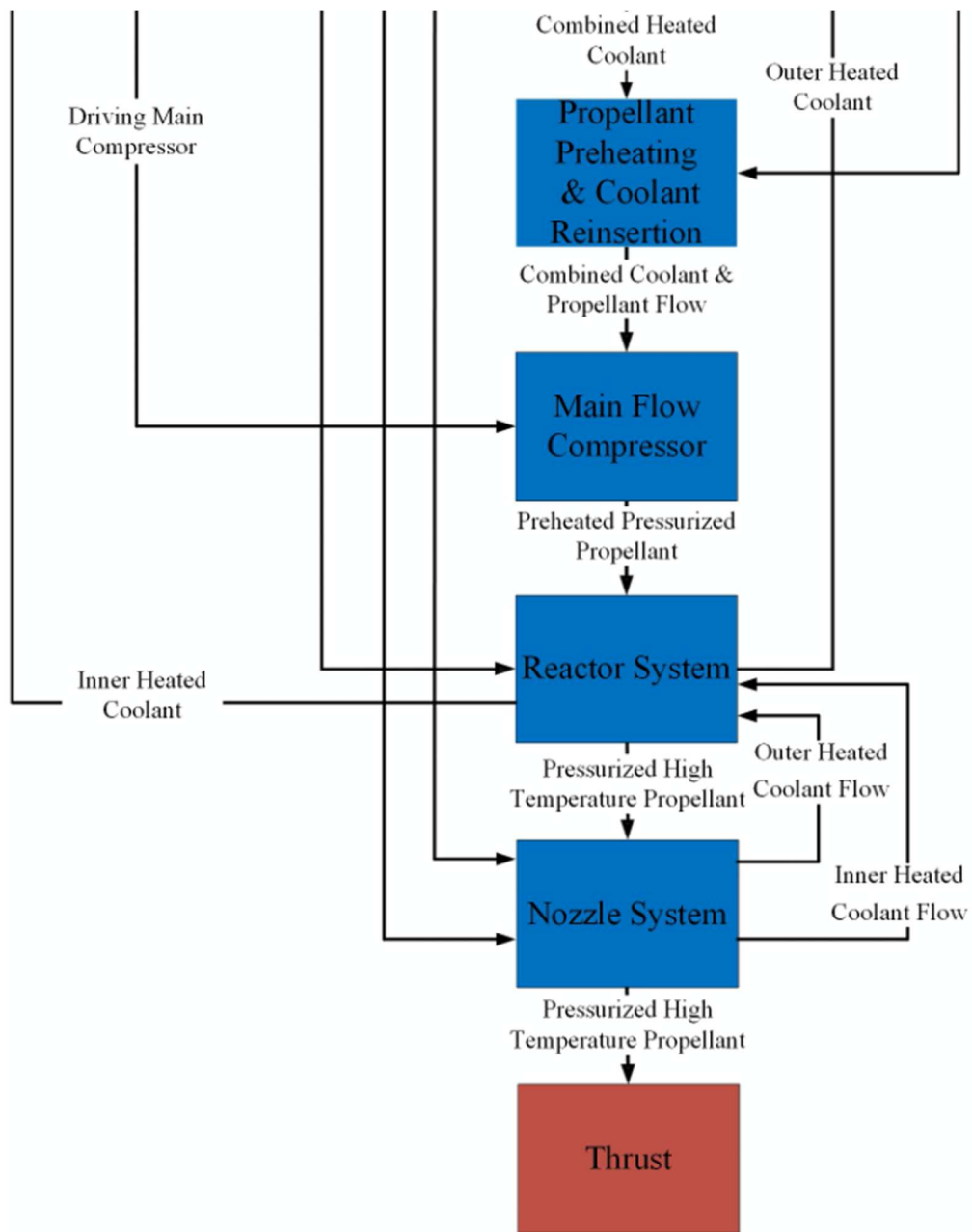


Fig. 19. The overall flowchart for the NTPS, part 2.

3 PROPELLANT FEED SYSTEM

3.1 Propellant Feed System Profile

A turbopump system is essential to increase the thrust output and lessen propellant consumption by the Nuclear Thermal Propulsion System. A turbopump system has several advantages, the first being the weight reduction of the propellant tank system. The reduction in tank weight stems from the ability to have lower propellant tank pressure by relying on the turbopump system to increase the propellant pressure to the required levels. A turbopump system also allows for much higher chamber pressure variability than what is achievable through high-pressure propellant tanks. An engine with a turbopump system would have greater flexibility and payload capacity over traditional high-pressure propellant tanks. A turbopump system consists of two main components, the pump, and the turbine. The turbine supplies the pump with rotational power; the pump translates the rotational power to the flow in the form of a pressure increase. The relationship between the pump and the turbine can take various configurations, the simplest being a direct drive system shown in Fig. 20.

Along with the pump and turbine arrangements, the pump can vary in its configuration as well. The main two styles of pumps are centrifugal and axial. The centrifugal pump is the most common pump style for rocket engines. The main reason for its extensive use is that it is very efficient at converting the incoming flow into a single direction, normal to the pump's center. Having the high-pressure flow traveling normal to the pump center allows for ease of channeling to the combustion chamber. The axial pump style can deliver much higher pressure ratios than the centrifugal pump while also

maintaining the flow parallel to the center of the pump. Thus, an axial style pump system was chosen for higher-pressure ratios and the maintaining of the flow parallel to the axis of the pump [1], [2], [31], [32].

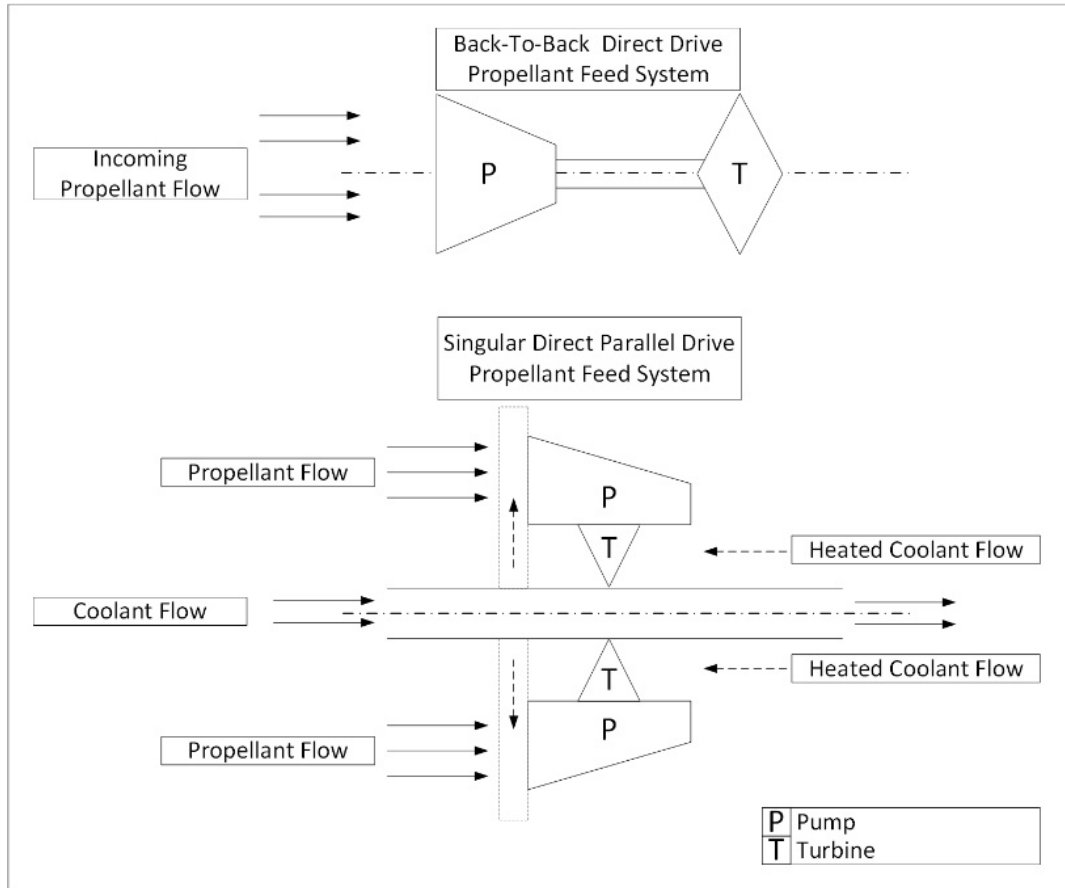


Fig. 20. Diagram of two propellant feed system configurations.

Parallel flow is ideal for the Nuclear Thermal Propulsion System due to the need for cooling of the nozzle spike system. To take advantage of this need for cooling the nozzle spike as well as the heated coolant resulting from that process, the Singular Direct Parallel Drive Propellant Feed System is being proposed. In Fig. 20, this system would allow for not only the spike to be cooled but for the heated coolant to drive the turbine.

The heated coolant would also preheat the incoming propellant to reduce the temperature gradient of the propellant entering the reactor and lessen the overall thermal strain on the annulus reactor system. This design would also allow for the use of a power generator turbine following the compressor turbine. The power generator would supply the needed power to the electric pumps of the coolant system. However, the Singular Direct Parallel Drive Propellant Feed System would only allow for power generation during the engine's use. Thus, the system would need to be complemented by another power source for various functions, such as engine startup. The proposed configuration, in theory, also have the potential for modification to allow for the generation of power in a low to no thrust state of the engine [1], [2], [31], [32].

The hypothetical nature of the Singular Direct Parallel Drive Propellant Feed System would fall between a technology readiness level of 1 and 2. Therefore, the new system must have a benchmark system to verify if the new propellant feed system is sufficient for the NTPS. The benchmark system will be the dual Mark 25 turbopump system developed by Rocketdyne. The Mark 25 was developed for the Phoebus 2A system, which is the benchmark for the Nuclear Thermal Propulsion System. The Singular Direct Parallel Drive Propellant Feed System (SDPD) must be able to meet or exceed the two primary design variables of chamber pressure and mass flow rate, established by the Mark 25. Therefore, the SDPD must be able to produce a chamber pressure of 4.30922 MPa while maintaining a mass flow rate equivalent to cryogenic hydrogen of 129.3 kg/s. Meeting these minimum design variables would ensure that the SDPD will be adequate for the Nuclear Thermal Propulsion System [1], [2], [33]–[35].

3.2 Propellant Feed System Decomposition

With the understanding of the need for the SDPD, coupled with the design variables that it must be able to meet, the next step in the design of the SDPD is to conduct a system decomposition. The system decomposition will result in a better understanding of the systems and subsystems that comprise the propellant feed system. Figure 21 illustrates the three main subsystems of the propellant feed system, which are the propellant heat exchanger, turbine, and compressor pump subsystem. The propellant heat exchanger subsystem is the byproduct of the interaction of the coolant system and the subsystems of the propellant feed system. The heated inner coolant flow provides the needed energy to drive the turbine and is mixed with the heated coolant flow in the propellant heat exchanger. While prior to the heat exchanger, the heated outer coolant flow is passed along the outer wall of the compressor to aid in the reduction of the temperature gradient encountered by the annulus reactor system. Once both inner and outer heated coolant flow are mixed within the heat exchanger, the flow is allowed to reduce in pressure to be reinserted into the propellant flow. The reinsertion of the heated coolant is the primary way the incoming propellant is preheated prior to the annulus reactor system. By reducing the temperature gradient, should lessen the overall thermal strain on the annulus reactor system. Thus, reinserting the heated coolant back into the engine to be used as fuel would make the combination of the propellant feed system and coolant system a cross between an expander and a staged cycle system. [1], [2], [29], [30], [34], [35].

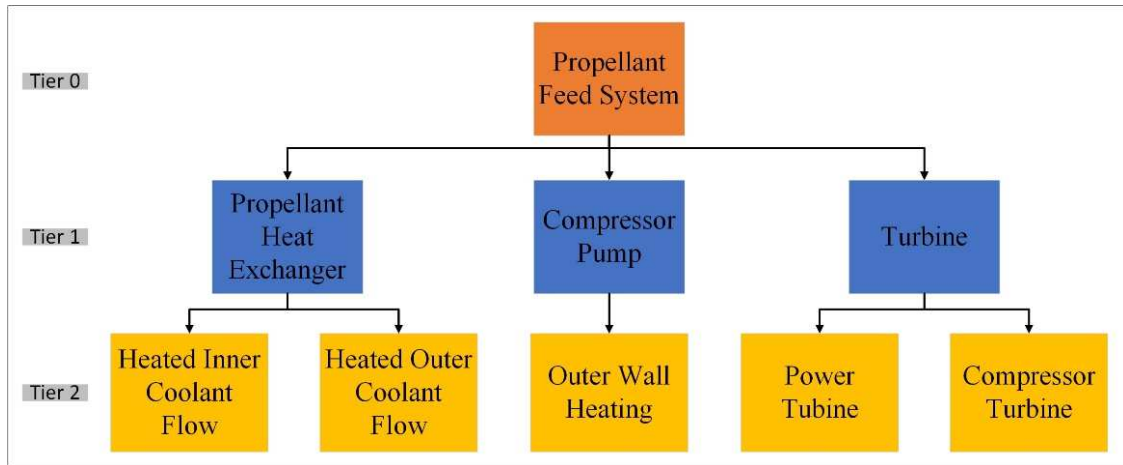


Fig. 21. Decomposition of the propellant feed system.

3.3 Propellant Feed System Integration

Understanding the integration of the SDPD is critical in grasping how the system is an entirely new kind of propellant feed system. The SDPD takes critical elements of some of the best configurations of propellant feed systems and reconfigures them to allow for the cooling of the spike by reconfiguring the propellant feed system to allow for the inner coolant flow to pass directly through its center. Thus, allowing the propellant feed system to take full advantage of the returning heated coolant from both the nozzle and annulus reactor systems. The advantage is the use of the inner heated coolant flow as the driving flow for both the compressor and power turbines. The heated coolant from both the inner and outer flows is further used as a preheater for the main propellant flow. The propellant preheating occurs as the propellant is passed through the propellant heat exchanger and mixed with reinsertion of the heated coolant flows. The main propellant is

further preheated as it compressed within the SDPD from the outer heated coolant flow channeled along the compressor's outer wall.

By integrating all the subsystems of the SDPD as well as incorporating the heated coolant flows, the SDPD would be capable of being directly mounted to the reactor system, significantly reducing the plumbing work needed for the engine. By reducing the amount of plumbing needed within the engine, the engine's overall mass is significantly lessened and allows for the simplification of the propellant flow path through the entire propulsion system. The simplification has the added benefit of reducing the number of possible failure points within the system; by reducing the distance that the high-pressure flow must travel. The integration of each aspect of the SDPD is illustrated in Fig. 22; this figure is numbered in a clockwise spiraling fashion, starting with the primary subsystems and then moving inward, illustrating the aspects that intertwine the given subsystems. Thus, the figure further reveals the depth of integration while maintaining the simplicity of the propellant flow [1], [2], [29], [30].

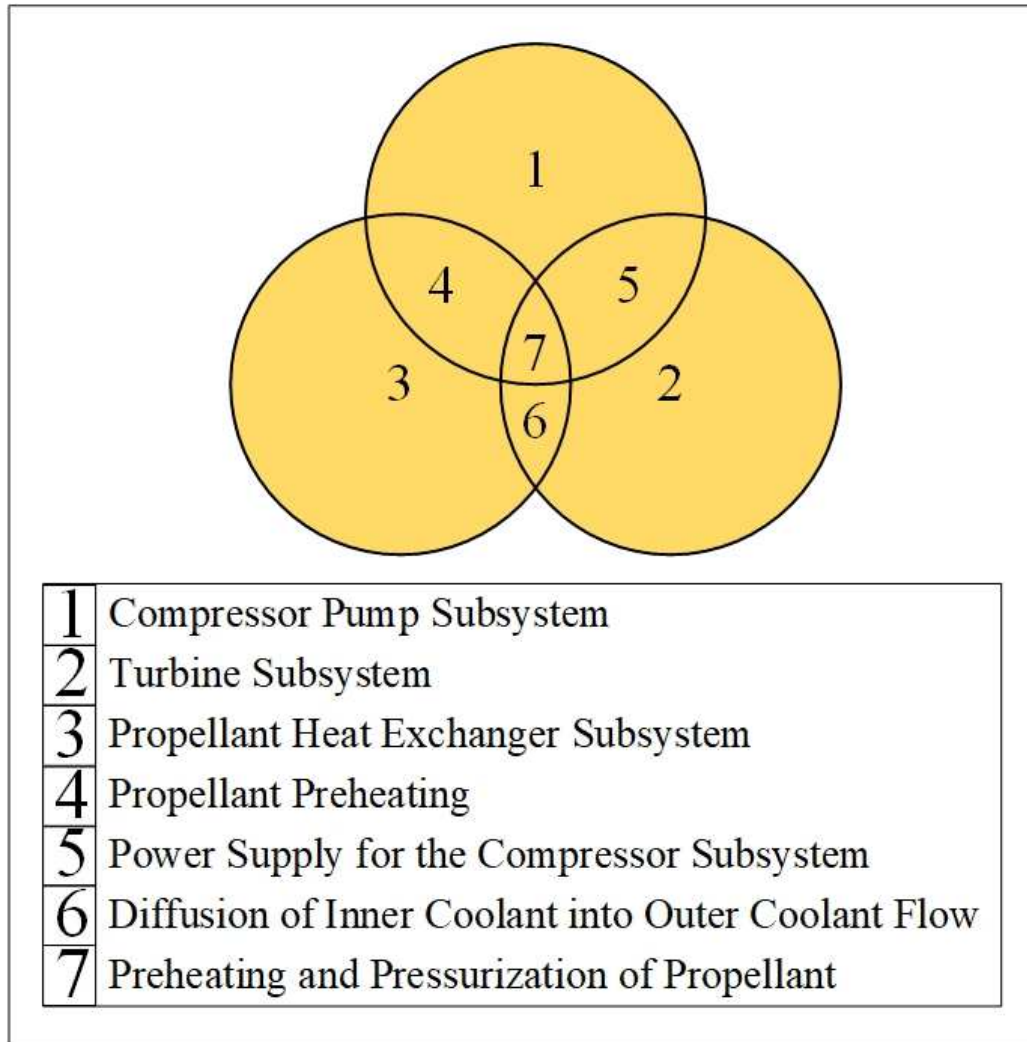


Fig. 22. Integration diagram of the propellant feed system.

3.4 Propellant Feed System Architecture

The combined understanding of the decomposition and systems integration allows for the construction of the propellant feed system's architecture. The first characteristic of the architecture is the understanding of primary inputs and outputs of the main three subsystems. Therefore, Fig. 23 illustrates the external and internal connections, whereas

Table 11 lists those connections as the inputs and outputs of the subsystems that stem from Tier 1 of Fig. 21. Other non-illustrated connections exist between the elements in Tier 2 and external systems that are out of the scope of the input and output diagram below [1], [2], [29], [30].

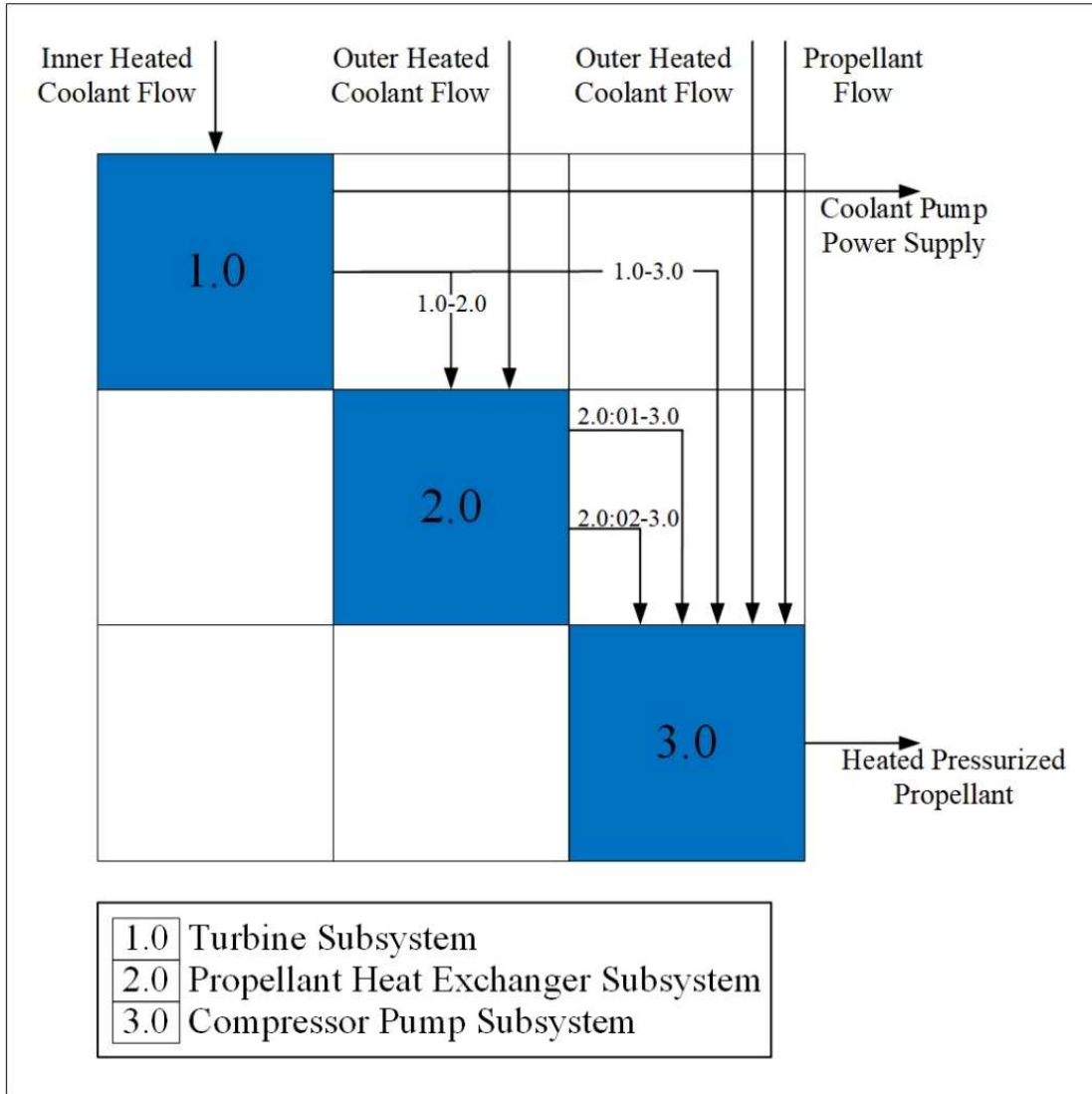


Fig. 23. The N² diagram for the propellant feed system.

Table 11
Inputs and Outputs of the N² Diagram

The direction of Input & Output	Performed Operation
In → 1.0	Inner Heated Coolant Flow
1.0 → 2.0	Inner Heated Coolant Flow
1.0 → 3.0	Drive Power to the Compressor Pump Subsystem
1.0 → Out	Coolant Pump Power Supply
In → 2.0	Outer Heated Coolant Flow
2.0: 01 → 3.0	Heated Coolant Flow Reinsertion
2.0: 02 → 3.0	Preheating of Propellant
In → 3.0	Propellant Flow
In → 3.0	Outer Heated Coolant Flow
3.0 → Out	Heated Pressurized Propellant Flow

The second characteristic of the system architecture is how the interconnection between the inputs and outputs of the different elements affects the system's propellant flow. This understanding is better grasped through a flowchart analysis of the data from Fig. 21 and 22. The flowchart analysis of the data from both figures on the propellant feed system is shown in Fig. 24. This flowchart shows how inputs of inner and outer heated coolant flows and propellant are utilized within the primary system's different main subsystems. With the input of both inner and outer heated coolant flows being fully utilized, they are diffused into the propellant within the propellant flow before the compressor pump subsystem. The newly combined propellant flow is then compressed while simultaneously being further preheated by the heated outer coolant flow. Upon exiting the compressor pump subsystem, the propellant is of high pressure and moderate temperature. The propellant's moderate temperature lessens the temperature gradient that is encountered by the annulus reactor system. By lessening the temperature gradient,

would slightly reduce the propellant’s ability to gain thermal energy; however, the slight thermal energy loss would lessen the overall thermal strain on the annulus reactor. Thus, the utilization of the SDPD configuration within the propellant feed system should allow for higher chamber pressures and greater propulsion system endurance. Therefore, the flowchart analysis below helps to solidify the understanding of the system's architecture and the function of the propellant feed system as a whole [1], [2], [29], [30].

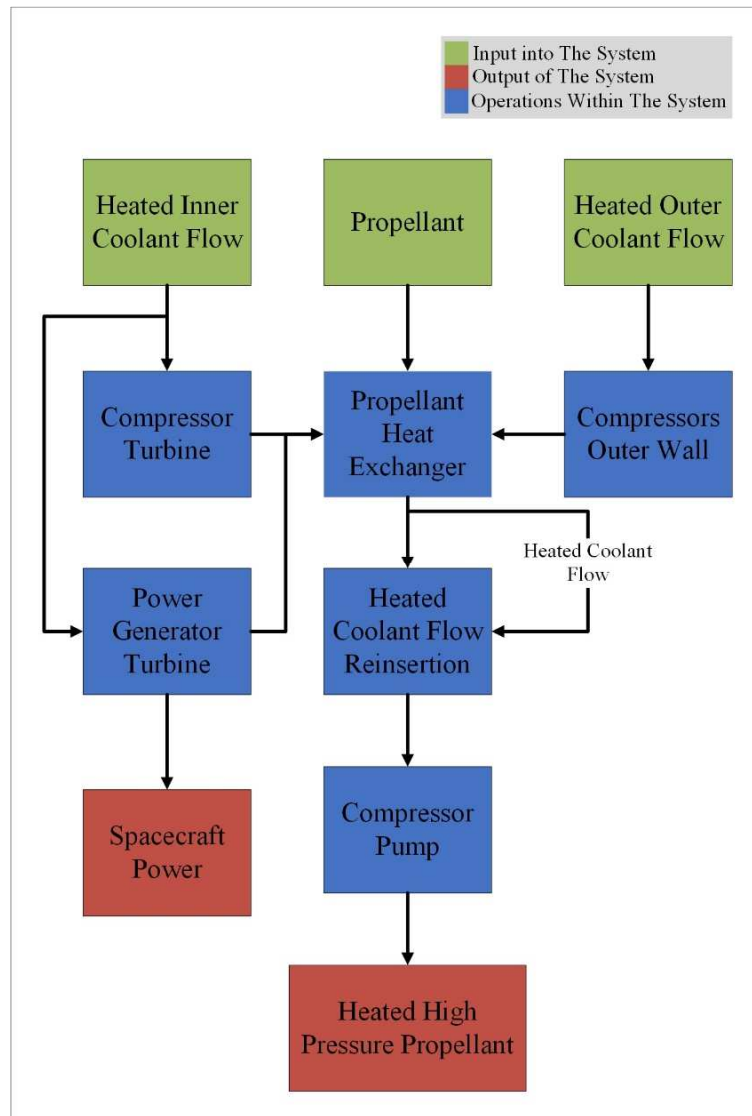


Fig. 24. Flowchart of the propellant feed system.

4 ANNULUS REACTOR SYSTEM

4.1 Annulus Reactor System Profile

The reactor system is the Nuclear Thermal Propulsion System's proverbial heart, making this system key in the redesigning process. The main two changes between the new Nuclear Thermal Propulsion System and the benchmark reactor system is the use of a new reactor fuel compound and the reconfiguration of the core. The new configuration of the core is known as the annulus reactor. As the name infers, the reactor system is fashioned into a hoop or ring shape for the primary purpose of allowing the inner coolant to pass through the reactor to cool the spike section of the nozzle. The partially heated coolant from the spike section of the nozzle is then diverted into inner cooling channels in the moderator of the reactor, as illustrated in Fig. 25. The inner and outer moderator heating channels allow the core's innermost section to remain at an adequate operating temperature. The coolant pass-through's secondary purpose is to consolidate the heated coolant flow from the reactor's inner moderator section. Thus, directing the heated inner coolant flow into the propellant feed system's drive turbine while the partially heated coolant flowing from the cowling section of the nozzle is diverted into the outer section of the moderator. The outer coolant channels function similarly to the inner channels, except the heated flow is directed to the outer wall of the compressor section of the propellant feed system. In order to accommodate the inner coolant passage, the nuclear fuel of the reactor system had to be reconfigured. The reconfiguration of the nuclear fuel was not suitable for the traditional hexagon-shaped fuel rods used in the benchmark engine. Thus, leading to the reactor system's second redesigned aspect, the annulus

reactor system would replace the hexagon-shaped uranium carbide fuel rods with Tri-Carbide fuel pucks. The Tri-Carbide fuel pucks are stacked into rods containing six pucks in each rod. The rods allow for the arrangement of nuclear fuel into a ring about the inner coolant pass-through, as illustrated in Fig. 26 [10], [36]–[38].

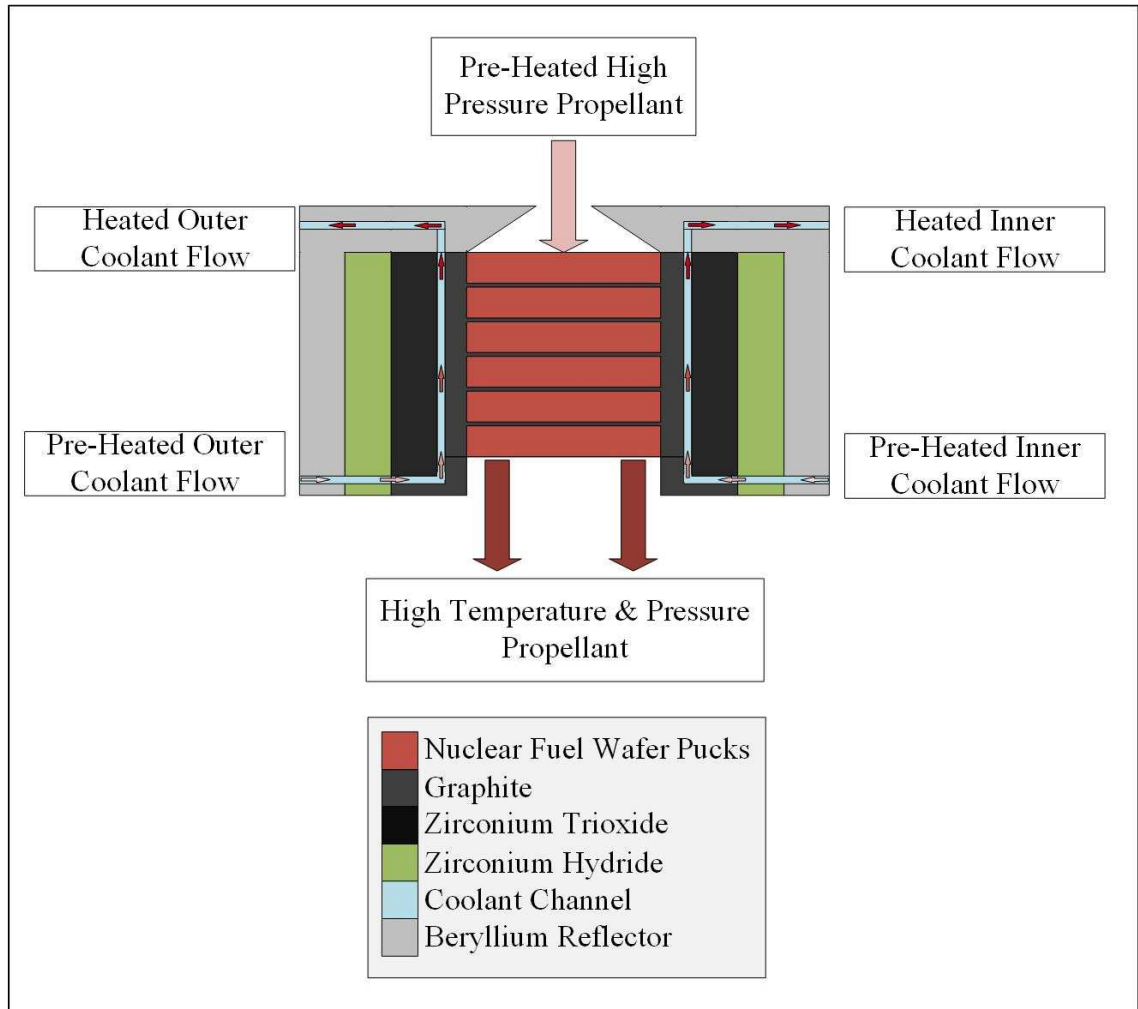


Fig. 25. Annulus reactor fuel rod cut-a-way.

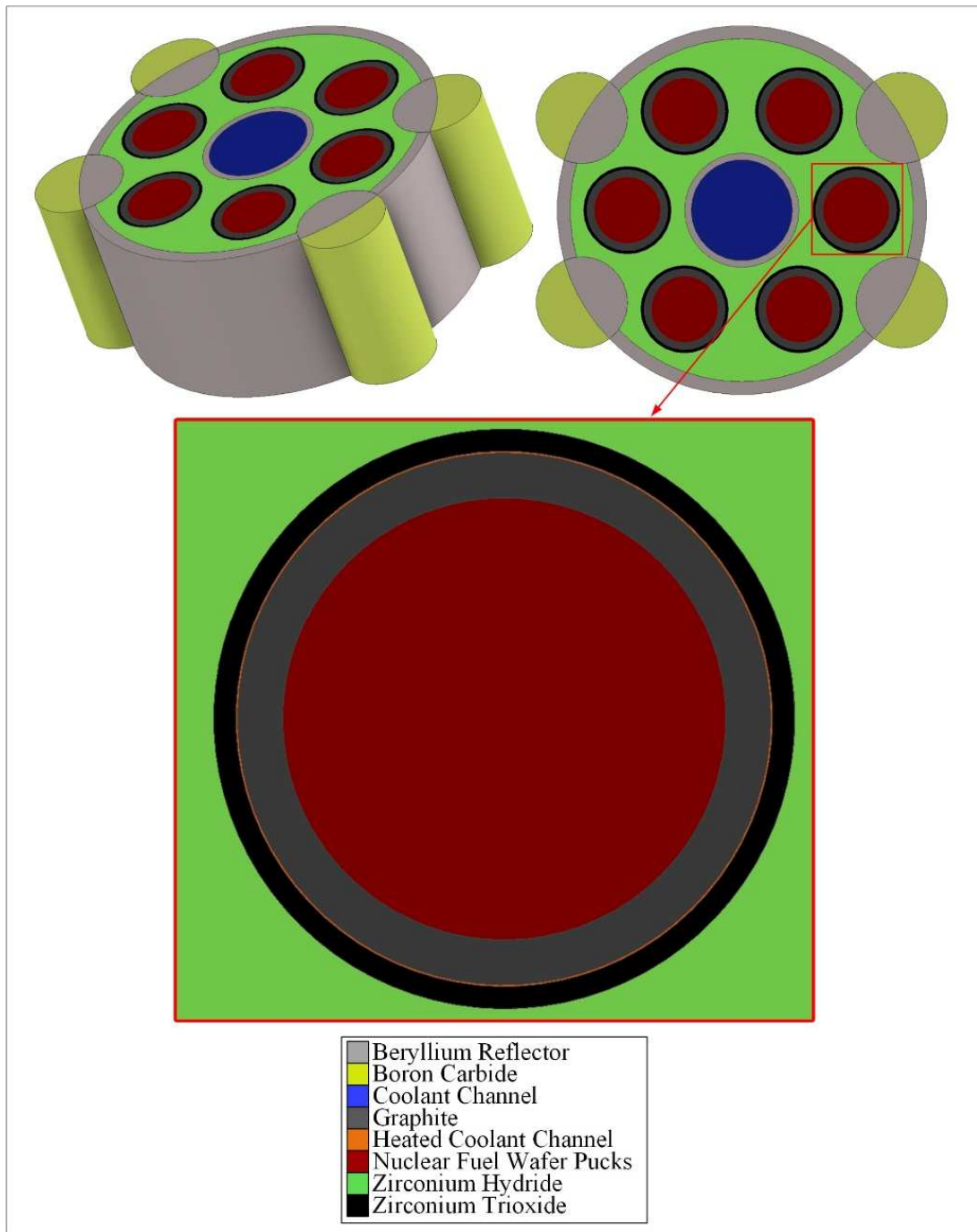


Fig. 26. The layout of the annulus reactor core.

The new fuel type and configuration have allowed for some critical advantages over the benchmark engine; the first and most significant being the estimated amount of enriched uranium required to reach critical mass. The annulus reactor would only need an estimated 97.4 kg of 93% enriched uranium for the entire reactor. The estimation was calculated by scaling the fuel puck from the Moderated Square-Lattice Honeycomb reactor to the appropriate size needed for the NTPS and compensating for the change in the cross-sectional flow area in the newly scaled fuel pucks. In comparison to the Phoebus-2A reactor, it contained around 300 kg of 93% enriched uranium. Thus, resulting in a 67.5% reduction in the needed uranium in the annulus reactor over the Phoebus-2A. The reduction is accomplished by the use of the Tri-Carbide fuel and the configuration of the moderator and reflector. In order to estimate the needed nuclear fuel and moderator for the annulus reactor, the reactor was based on the Moderated Square-Lattice honeycomb design proposed in the “Nuclear Design Analysis of Square-lattice Honeycomb Space Nuclear Rocket Engine.” However, the Moderated Square-Lattice Honeycomb reactor is relatively small, with a core diameter of just over half a meter. Were the annulus reactor would need a core diameter of 2.827 meters. The reasoning for such a large core diameter is to maintain the needed cross-sectional flow area of the core. Thus, the Moderated Square-Lattice honeycomb core's nuclear fuel dimensions were scaled by 1956.34 % to accommodate the larger cross-sectional flow area. The newly scaled fuel pucks have a total cross-sectional flow area of .0632 m² at 5.06% removal of each puck's cross-sectional area, as stated in Table12. Thus, the original fuel pucks contained 102 grams of 93% enriched uranium each. The newly scaled fuel puck will

contain, on average, 2.71 kg of uranium, which are arranged into six fuel rods, seen in Fig. 27. The implantation of the fuel pucks also allows for other critical advantages over the Phoebus engine. For instance, the Tri-Carbide compound has the potential for a safe operating temperature in excess of 3000 K, whereas the Phoebus-2A reactor core could only safely operate at 2310 K. At a core temperature of 3000 K, the annulus reactor would be, on average, 30% hotter than the benchmark engine [36].

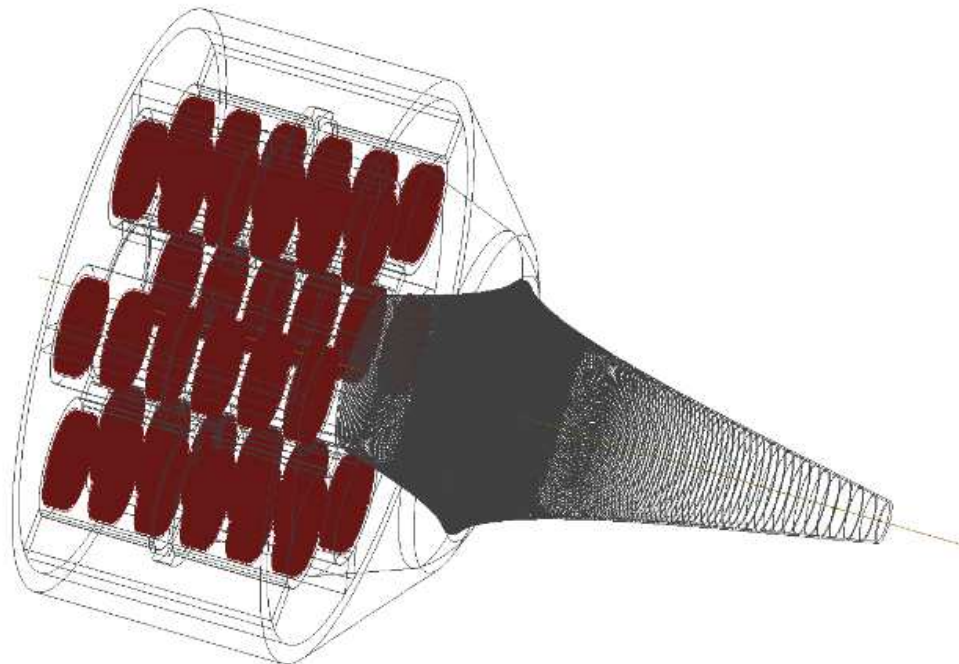


Fig. 27. Fuel puck orientation within the engine.

Table 12
Annular Reactor Design Data

Annulus Reactor Data					
Fuel Rod	Diameter (m)	Height (m)	Fuel Puck	Diameter (m)	Height (m)
	0.876	1.32		0.514	0.1
	Total Number Fuel Rods	Tri-Carbide Wafer Grid in Present of the Radius		Total Number Fuel Pucks	Cross-Sectional Flow Area (m ²)
	6	58.69%		36	0.0105
	Graphite in Present of the Radius	Coolant Channel in Present of the Radius		Total Estimated enriched U235 Per-Puck (kg)	Percent of Removal for Flow Channels
	11.74%	0.50%		2.71	5.06%
	Zirconium Tri-Oxide in Present of the Radius	Zirconium Hydride in Present of the Radius			
	5.87%	23.21%			
Annulus Core	Cross-Sectional Flow Area (m ²)	Total Estimated enriched U235 (kg)	Fuel Puck wafer Grid	Flow Channel Width (m)	Flow Channel thickness (m)
	0.0632	97.4		0.0095	0.0036
	Inner Coolant pass-through Diameter with Reflector (m)	Reflector Thickness (m)		Flow Channel Cutout Width (m)	Total Number of Flow Channels Per-Puck
	0.876	0.1		0.0022	2178
	Core Diameter with Reflector (m)	Core height without top reflector (m)			
2.827	1.3				

Starting from the flow channel size and subsequently establishing the tri-carbide thickness around each flow channel, an approximation for the number of square channels per round fuel puck is needed to equal the total cross-sectional flow area. This approximation emulates the classical mathematical problem of “squaring the circle.” Fortunately, the manufacturing of silicon chips represents a similar problem; thus, Equation 11 is used in approximating the number of flow channels. This equation yielded 2,178 channels for each fuel puck in order to match the total cross-sectional flow area need. Each puck's size was kept to the same size as initially scaled, as seen in Fig. 28 and

Table 12. In theory, the pucks should be able to handle much higher chamber pressures than the original design. Thus, by coupling, the increase in the core temperature with added strength from the puck design should enable the annulus reactor to be able to have multiple restarts while producing higher thrust and Isp levels than that of the Phoebus-2A [10], [36]–[41]

$$D_{PW} = \frac{\pi \cdot \left(\frac{W_D}{2}\right)^2}{D_A} - \frac{\pi \cdot W_D}{\sqrt{2 \cdot D_A}} \quad (11)$$

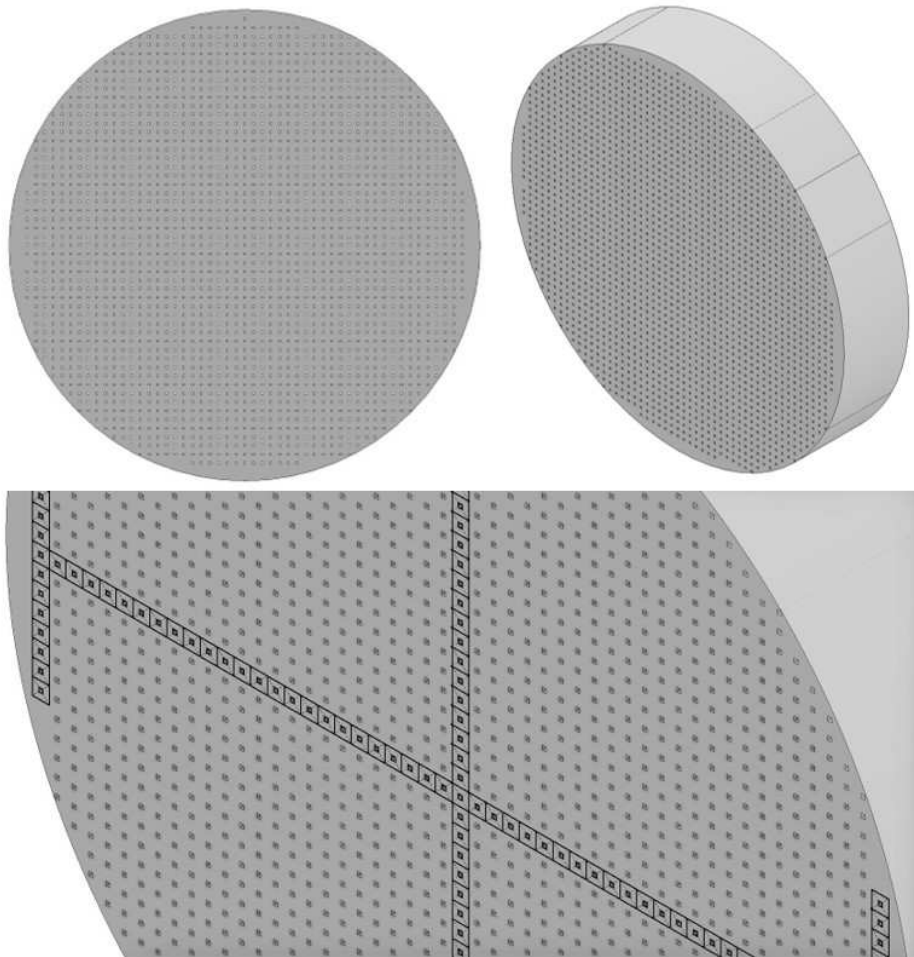


Fig. 28. Tri-carbide nuclear fuel puck.

4.2 Annulus Reactor System Decomposition

A decomposition is needed to better understand all the systems and subsystems of the new configuration that should exceed all benchmarks laid out by the previous Reactor. A decomposition of the system and the reactor's primary systems are shown in Tier 0-1 of Fig. 29. The fuel rod system, as discussed, consists of six fuel rods, and within each rod containing six nuclear fuel pucks. The pucks are stacked vertically with the flow channels aligned to allow for the maximal heat transfer between the pucks and the propellant. A subsystem of the fuel rod system is the moderator system, which is the key to reducing the needed uranium. The moderator is a zirconium hydride matrix, which facilitates the thermalization of the neutron spectrum. Thus, increasing the neutron interaction with the fuel pucks, thereby reducing the needed uranium to maintain critical mass. The reflector system also aids in the reduction of uranium by using beryllium to reflect escaping neutrons back into the core. The reflective beryllium is placed at the top of the reactor core and axially around it, and no beryllium is placed at the base of the core due to exhausting propellant temperatures. The control rod system is similar to that of the cylindrical rotating control rod system used in the Phoebus-2A reactor. The four rods are comprised of a neutron reflective and absorption material. The neutron reflective material of beryllium comprises the vast majority of each rod. Thus, only a fraction of the rod is of boron carbide, which is used as the neutron absorption material. By rotating the rod to expose more or less of the absorption material, the rate of fission can be controlled. Therefore, controlling the core temperature and allowing the Nuclear Thermal Propulsion System to be throttleable [3], [6], [10], [36]–[40], [42].

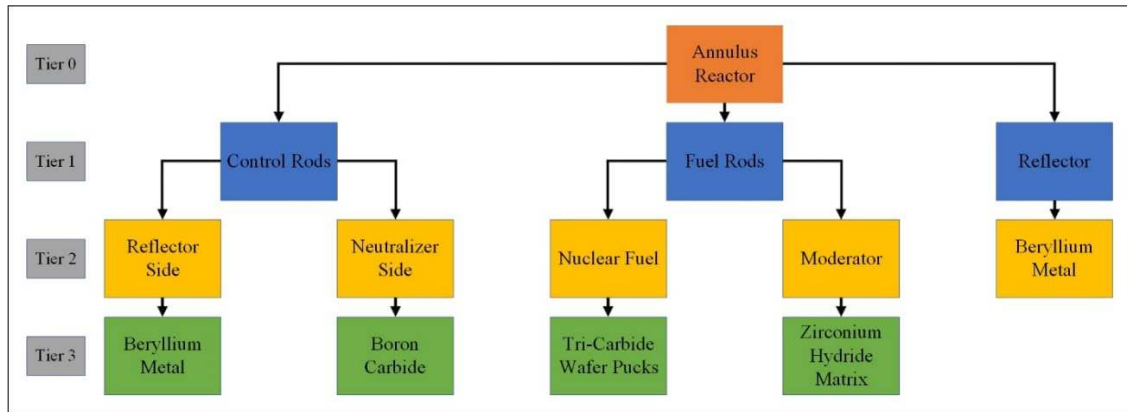


Fig. 29. The annulus reactor decomposition.

4.3 Annulus Reactor System Integration

To better comprehend how the reactor's primary systems are interconnected to form the streamlined annulus reactor, a system integration analysis was conducted. Fig. 30 illustrates the high degree of integration to maintain the compact and high performing reactor system. Thus, the figure also illustrates how the three primary systems are interconnected among one another. The central system of the annulus reactor is the fuel rods system, with both the control rods system and the reflector system interacting with the central system. The control rods and reflector systems both work in tandem to sustain the reactor's desired fission rate. However, both systems operate in different capacities to maintain the desired rate of fission. The control rod system is continually adjusting the amount of the neutron absorption material that is exposed to the core, thereby regulating the number of neutrons that can interact with the fuel rod system. Whereas the reflector system reverberates the vast majority of the free neutrons attempting to escape the core, thereby causing the reflected neutrons to interact with the fuel rods, completing how each

of the primary systems of the annulus reactor system is integrated to maintain the desired rate of fission and, subsequently, the thrust output of the engine [6], [30], [36], [38], [39].

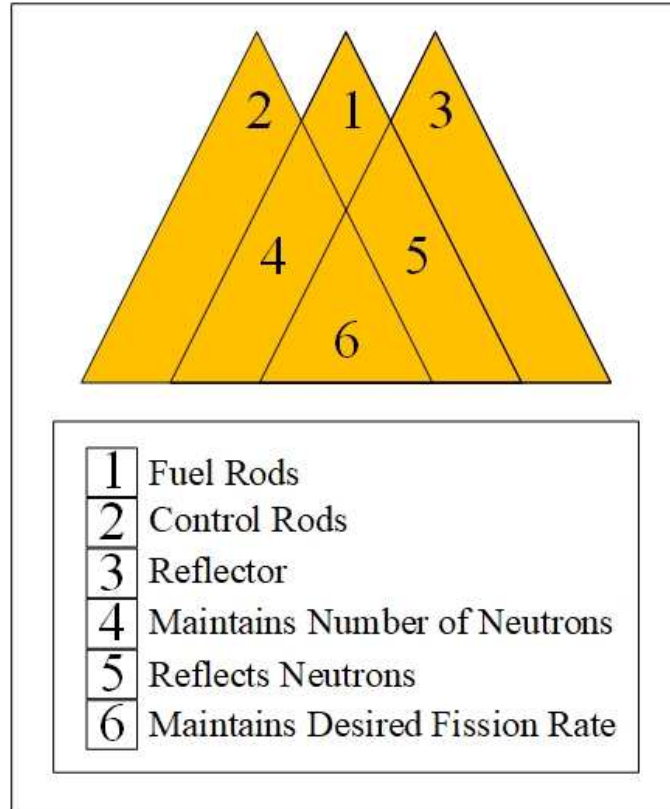


Fig. 30. Integration diagram for the annulus reactor system.

4.4 Annulus Reactor System Architecture

An architecture analysis of the annulus reactor system allows for a more precise visualization and understanding of how each system and subsystem interacts. The architecture analysis consists of two sections, the input, and output analysis, shown in Fig. 31, and the flowchart layout. The input and output analysis (N^2) conducted has a resolution level that focuses on the three primary systems discussed in the system integration analysis. The N^2 analysis begins with the central system of the fuel rods, from

which the other systems receive input or output. The other two primary systems, the reflector and control rod system, will only interact with the central system at this level of analysis. The two significant outputs based on the N^2 analysis are the high-temperature and high-pressure propellant along with the desired fission rate of the reactor, the other interactions between each system of the N^2 analysis are listed in Table 13 [29], [30], [36]–[39].

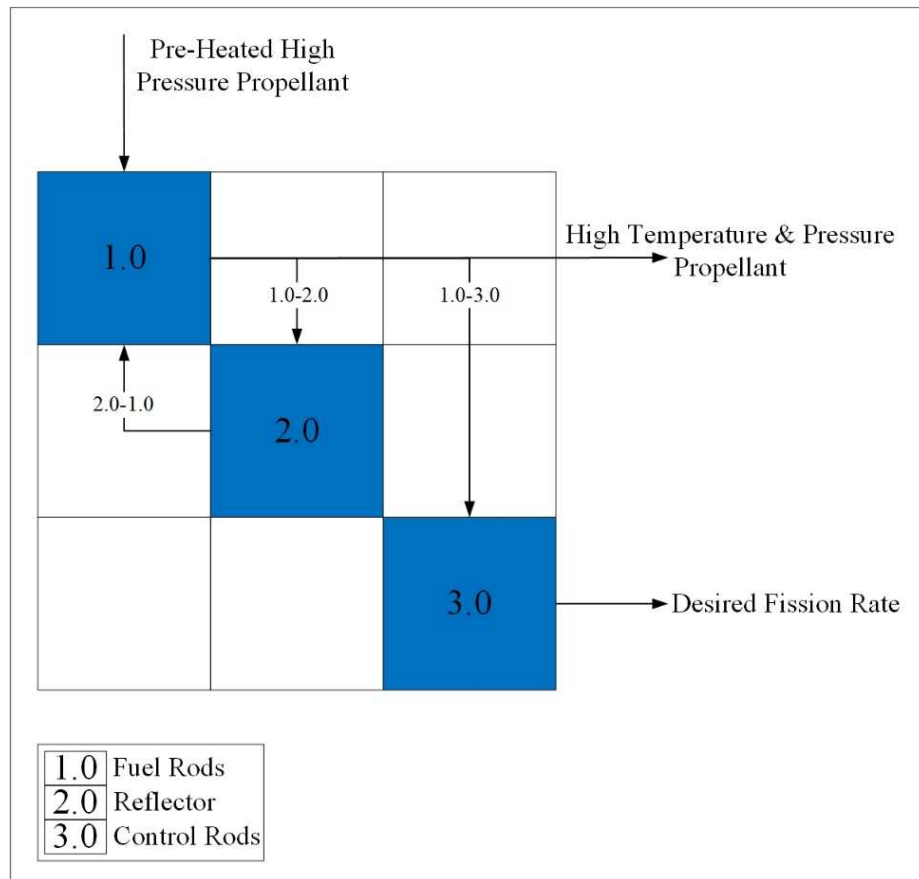


Fig. 31. N^2 diagram for the annulus reactor system.

Table 13
Inputs and Outputs of the Annulus Reactor System N² Diagram

The Direction of Input & Output	Performed Operation
In → 1.0	Preheated High-Pressure Propellant
1.0 → Out	High-Pressure and High-Temperature Propellant
1.0 → 2.0	Escaping Neutrons
1.0 → 3.0	Escaping Neutrons
2.0 → 1.0	Reflected Neutrons
3.0 → Out	Desired Fission Rate

The second level of the architecture analysis of the annulus reactor is the flowchart layout. The flowchart layout conveys the interactions between each of the primary systems of the reactor. In Fig. 32, the fuel rod system's central nature becomes prevalent, as each of the primary systems influences the fuel rod system. The fuel rod system's primary function is to transfer thermal energy from the nuclear fuel to the propellant, while the other primary systems and subsystems are to maintain or regulate the number of free neutrons that are interacting with the nuclear fuel to ensure the desired fission rate is maintained. Therefore, the Nuclear Thermal Propulsion System can produce the needed thrust output for any given stage in the mission profile [29], [30], [36]–[39].

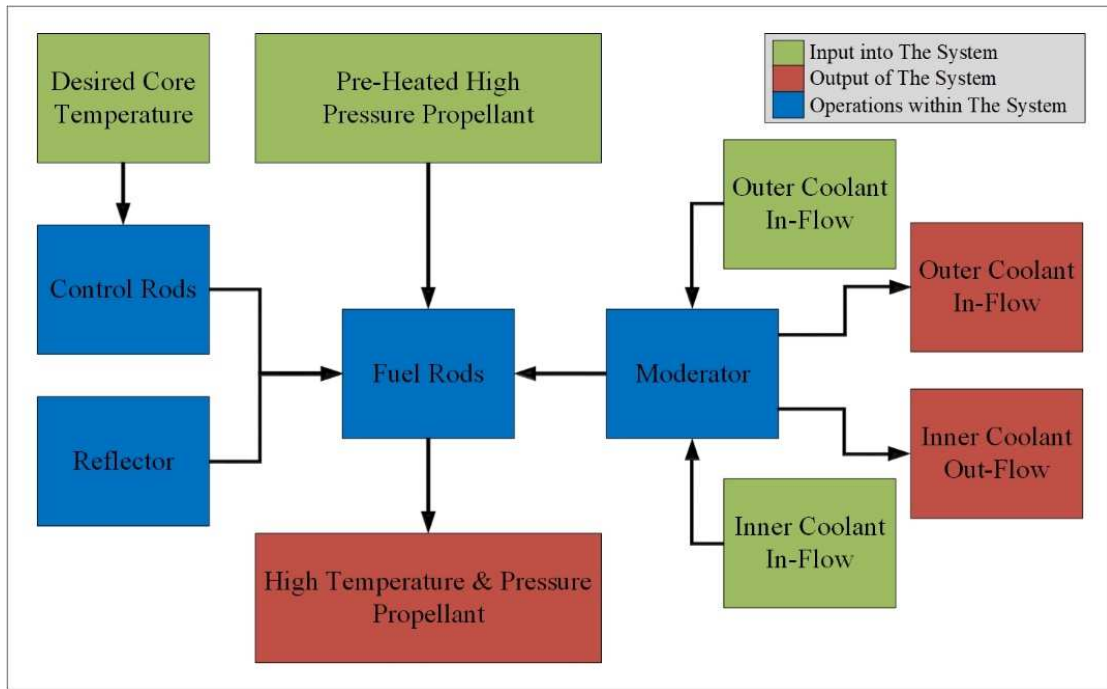


Fig. 32. Flowchart for the annulus reactor system.

5 NOZZLE SYSTEM

5.1 Nozzle System Profile

As discussed, the nozzle system is one of the critical aspects of overcoming the current limitations of modern high thrust rocket engines. Thus, the implication of an aerospike nozzle system is the logical choice for overcoming those limitations. The following is an adapted toroidal aerospike nozzle system for coupling with a nuclear thermal propulsion system. The nozzle system consists of three primary systems, the nozzle cowling, spike, and support structure. The nozzle spike system's exiting contour was designed by the use of expansion waves from the theoretical throat position relative to the cowling, and the contour design is expanded systematically in the nozzle system analysis section below. The nozzle spike system's convergent contour section is designed in the same manner as a traditional De Laval nozzle. The distinguishing difference between the De Laval nozzle convergent contour and the nozzle spike system's convergent contour is that the combustion chamber's dimensions primarily drive the De Laval nozzle geometry. With the Nuclear Thermal Propulsion System having no need for such a section of the nozzle, the annulus reactor system's geometry was used as the driving geometry for the contour. A 2-dimensional illustration of a convergent and exiting contour is shown in Fig. 33. The illustration shows the exiting contour of the nozzle spike system with a truncation. The truncation allows the coolant system to cool the end of the contour adequately, thus maintaining the nozzle spike system's structural integrity. The losses due to the truncation at 86.9% of the spike's full length would be minor. The minor losses are based on other tests that focused on an optimized spike

nozzle of varying truncations. The test results showed that significant performance losses only began to occur in designs with truncations less than 60% [2], [43], [44].

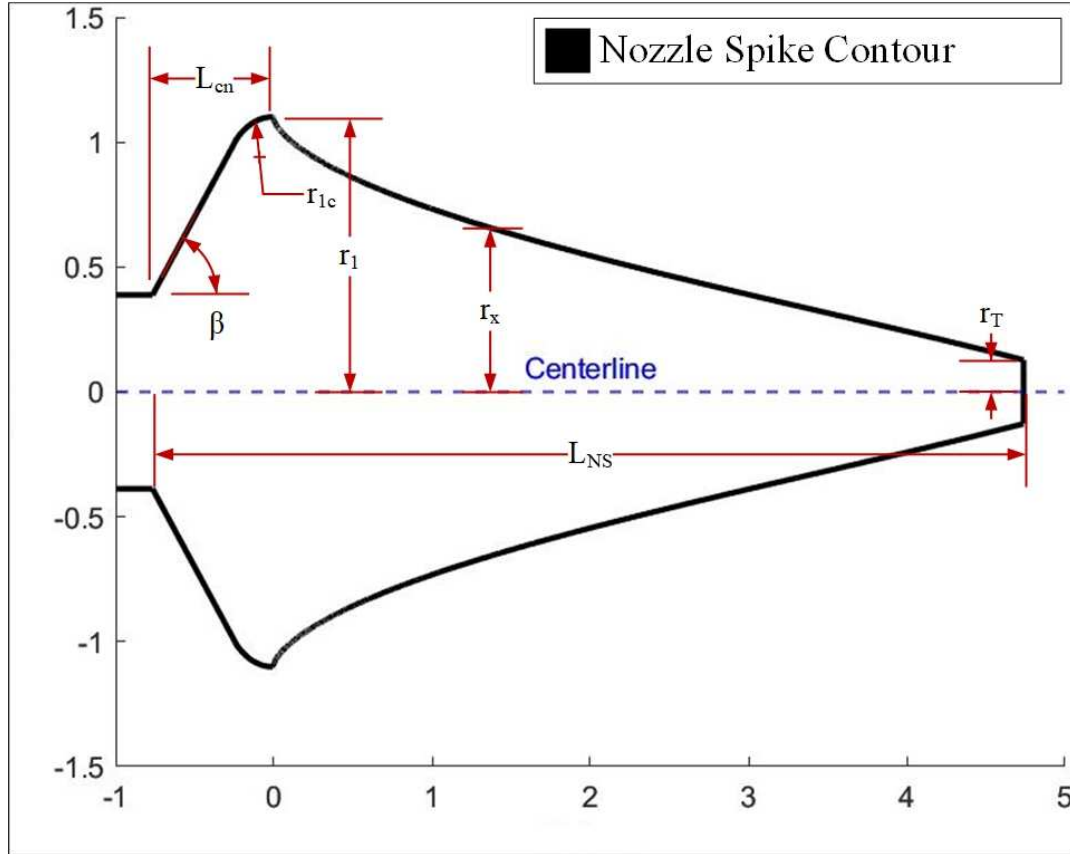


Fig. 33. A 2-dimensional contour plot of a nozzle aerospike.

The nozzle cowling system works in tandem with the nozzle spike system to optimally accelerate the high temperature and pressure propellant in a single direction to create thrust. The ending location of the nozzle cowling system is critical to the overall design of the nozzle system. This criticality stems from the fact that the exiting contour is based on the ending location to form the initial location of the throat properly, as illustrated in Fig. 34. The nozzle cowling system will be mounted to the outer and inner

sections of the annulus reactor system to uphold the needed structural integrity of the nozzle system [44].

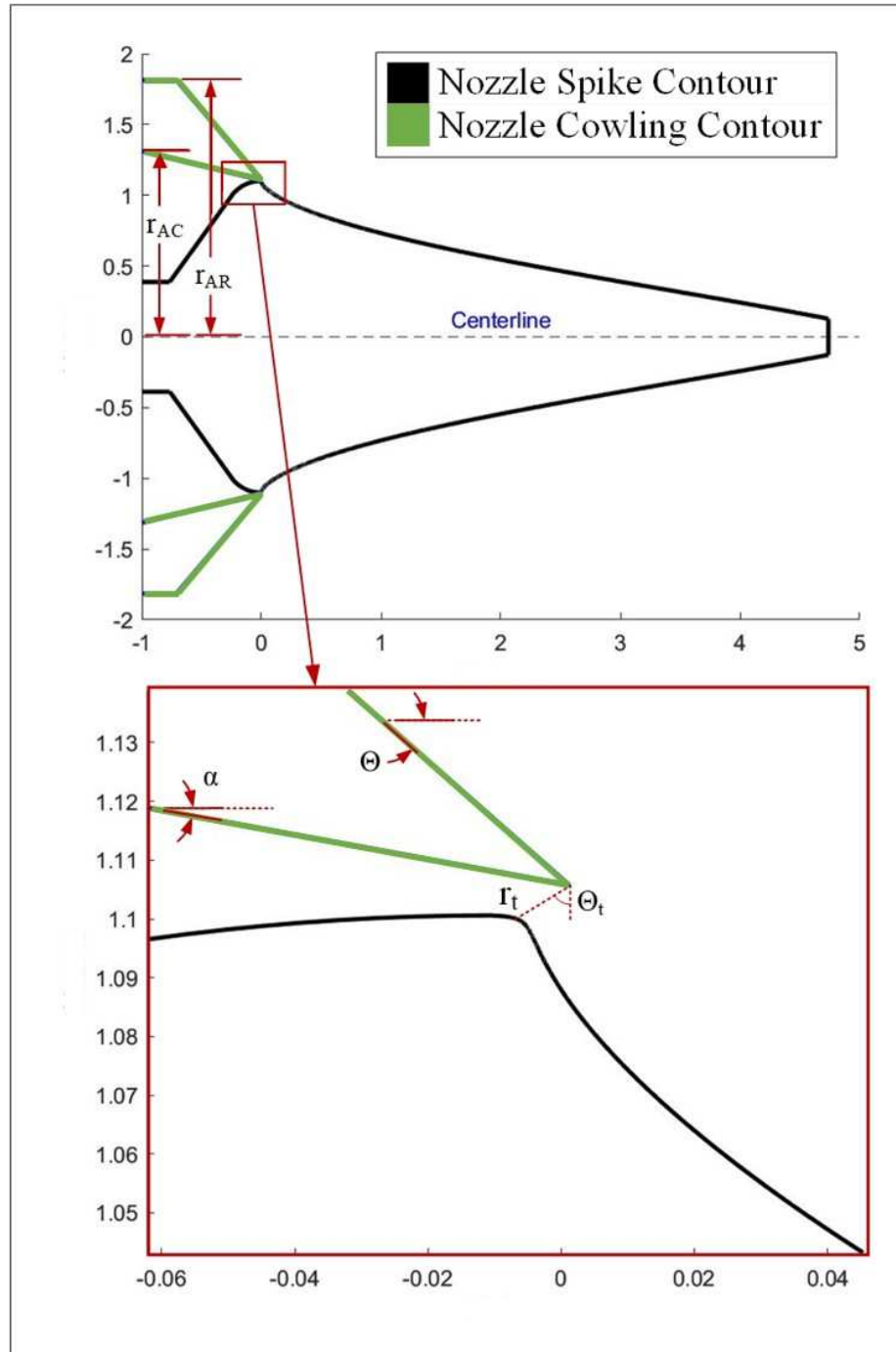


Fig. 34. A 2-dimensional contour plot of a nozzle spike with cowling.

The nozzle support structure system is designed to provide structural rigidity as well as delivering the inner and outer coolant flows to their respective areas in the annulus reactor system. The system is laid out in a spoke and hub configuration, as seen in Fig. 35. This configuration allows the nozzle system to be securely mounted into the Nuclear Thermal Propulsion System. The mounting configuration will also allow the maintaining of full integration of all four central systems of the Nuclear Thermal Propulsion System. Thus, constructing the nozzle system in this manner has maintained optimization for the annulus reactor system along with any atmospheric conditions that may be encountered [2], [45].

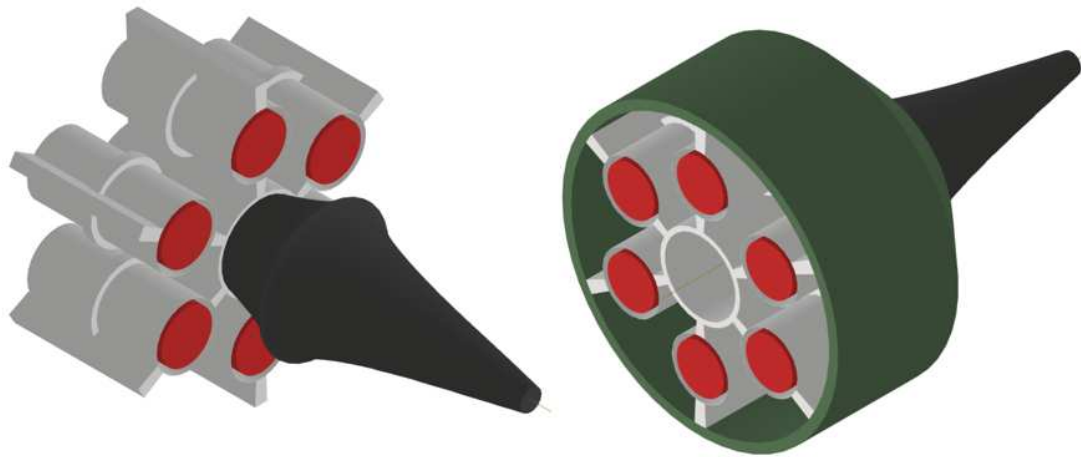


Fig. 35. The nozzle support structure system.

5.2 Nozzle System Decomposition

In order to have a better understanding of the functionality of the nozzle system, a system decomposition is needed. The decomposition enables the visualization of the primary systems and their subsequent subsystems. As illustrated in Fig. 36, Tier 0 is the

overall nozzle system, which is then separated into the three primary systems on Tier 1. The three primary systems, as discussed previously, consist of the nozzle cowling, support structure, and spike systems, which are further separated into subsystems, as shown in Tier 2 of Fig. 36. By examining Tier 2 in the figure below, it is noticeable that both the inner and outer coolant flows are the same two flows that are used by the nozzle support structure system. The use of both the inner and outer coolant flows by the nozzle support structure system is done once the cowling and spike have been adequately cooled. The two flows are then diverted into the outer and inner heating channels within the nozzle support structure system to maintain the moderator system's proper temperature while gaining a large amount of thermal energy. Thus, having each subsystem focused on channeling and using the coolant flow has allowed the nozzle system to be linked with the coolant and annulus reactor systems [29], [30], [44].

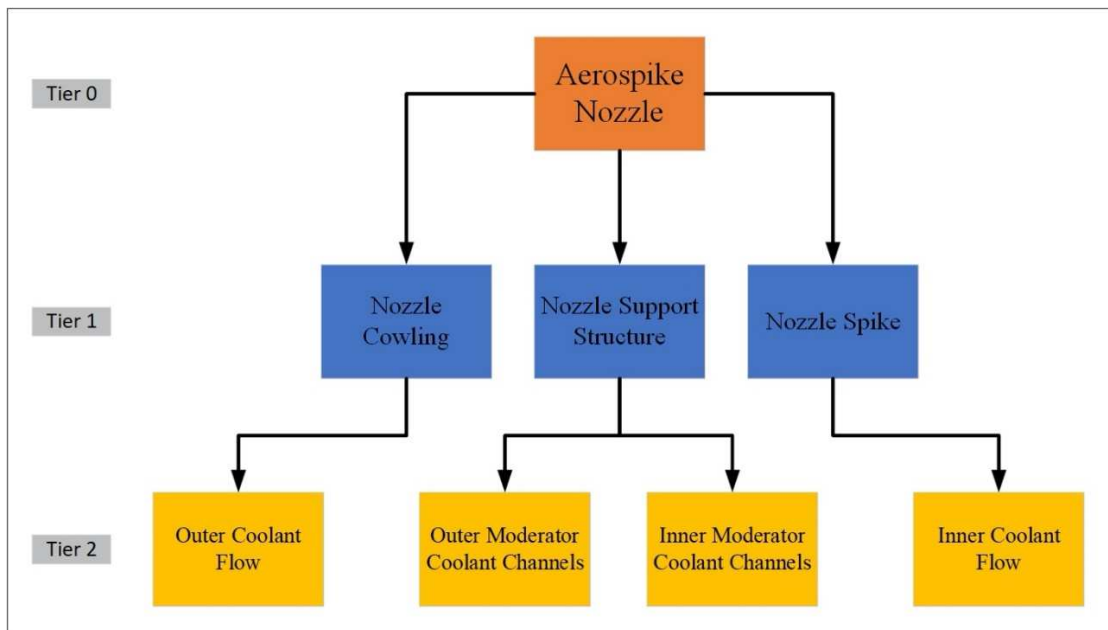


Fig. 36. Decomposition of the nozzle system.

5.3 Nozzle System Integration

As previously described, the nozzle system as a whole is highly integrated with both the annulus reactor system and coolant system. Similarly, the nozzle system's three primary systems are highly integrated to allow for the system as a whole to perform the tasks for which it was designed. Thus, Fig. 37 visually shows how each of the primary systems is integrated and the benefits of that interaction. The first primary system, the nozzle support structure, interacts with the second system in Fig. 37, which results in the needed inner channels for coolant to be supplied to the inner moderator section of the reactor. Similarly, the interaction between the first and third primary systems ensures that the moderator's outer portion can be supplied with coolant. However, the integration between the second and third primary systems performs the nozzle system's principal function, accelerating the heated pressurized propellant to create thrust. The integration of all three primary systems allows for the use and proper delivery of both the inner and outer coolant flows to their essential perspective areas of the Nuclear Thermal Propulsion System [2], [29], [30].

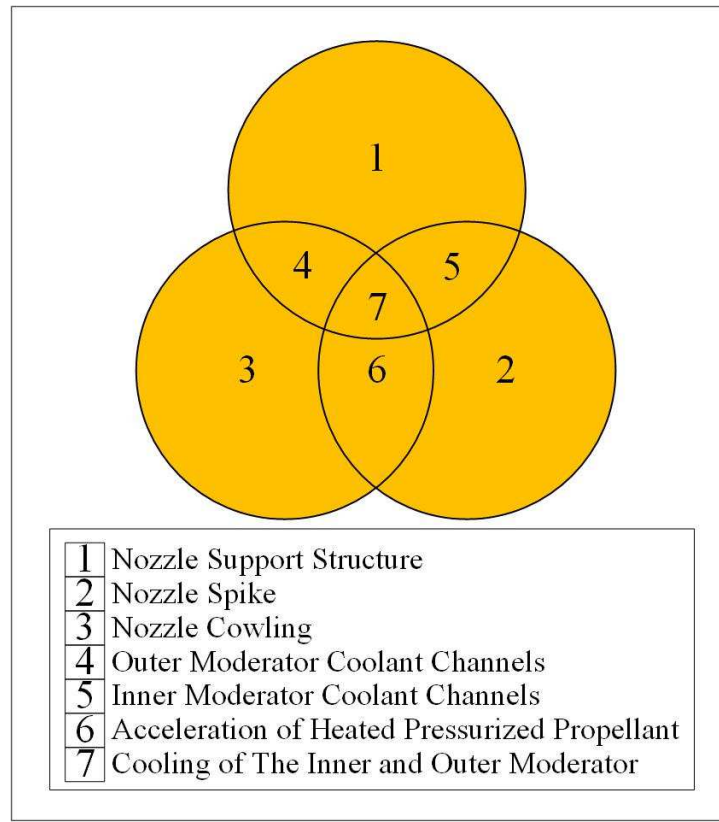


Fig. 37. The integration diagram of the three primary nozzle systems.

5.4 Nozzle System Architecture

An architecture analysis was conducted on the nozzle system to aid in the understanding of the interaction between the three primary systems. The architecture analysis consisted of two segments, the input & output analysis, followed by an operational flowchart analysis. As shown in Fig. 38 and Table 14, the input & output analysis visually illustrates the inputs to each of the primary systems and their corresponding outputs. The figure illustrates how both the nozzle cowling system and the nozzle spike system work in conjunction using the heated pressurized propellant to

produce an output of thrust. The interaction between all three primary systems, referring to the coolant flow, allows the moderator system to be adequately cooled [2], [29], [30].

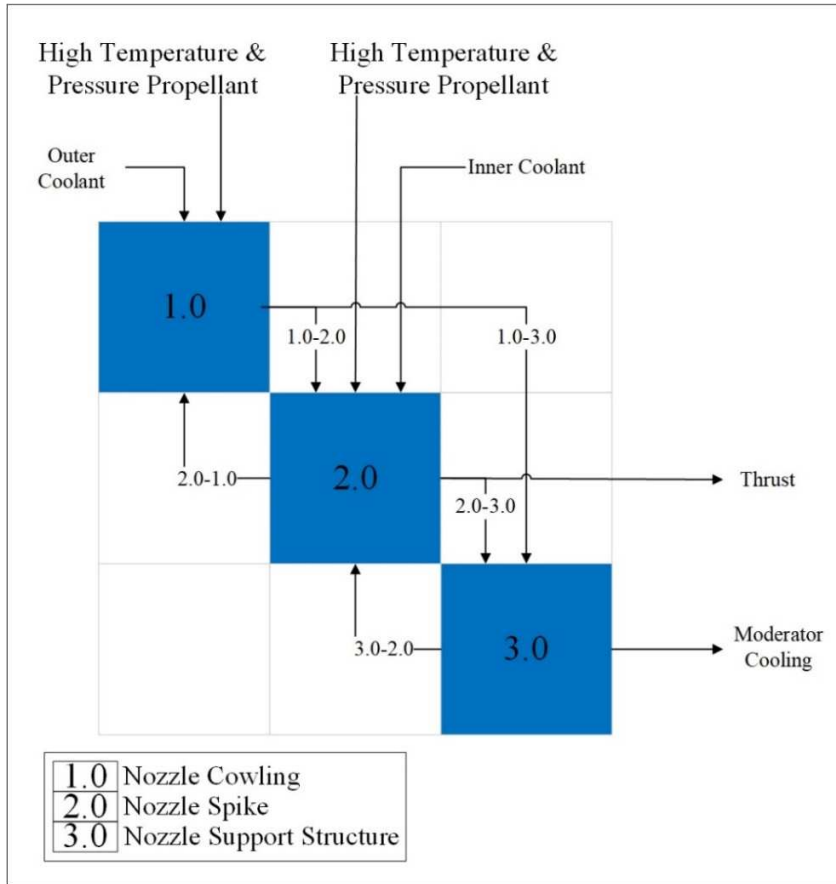


Fig. 38. N² diagram for the nozzle system.

Table 14
Inputs and Outputs of the Nozzle System N² Diagram

The Direction of Input & Output	Performed Operation
In → 1.0	Outer Coolant Flow
In → 1.0	Heated Pressurized Propellant
1.0 → 2.0	Acceleration of Propellant
1.0 → 3.0	Partially Heated Outer Coolant Flow
In → 2.0	Inner Coolant Flow
In → 2.0	Heated Pressurized Propellant
2.0 → 1.0	Acceleration of Propellant
2.0 → 3.0	Partially Heated Inner Coolant Flow
2.0 → Out	Thrust
3.0 → 2.0	Stabilization and Support for the Nozzle Spike
3.0 → Out	Coolant supplied to the Moderator System

The second analysis that was performed was the operational flowchart analysis; the analysis lends insight into how integration and the input & output of the primary systems are interconnected within the nozzle system. Fig. 39 below illustrates how the three main inputs into the nozzle system are the heated pressurized propellant, the inner coolant flow, and the outer coolant flow. The three inputs then interact with the nozzle cowling and spike systems; the inner and outer coolant flows are then directed into the nozzle support structure. The nozzle support structure channels both coolant flows to their respective areas of the moderator System. As the coolant reaches the top of the annulus reactor system, the nozzle support structure system consolidates and redirects the heated coolant flows to their corresponding areas of the propellant feed system. Simultaneously, the heated pressurized propellant is focused and accelerated axially along with the nozzle spike, creating the thrust of the Nuclear Thermal Propulsion System [2], [29], [30].

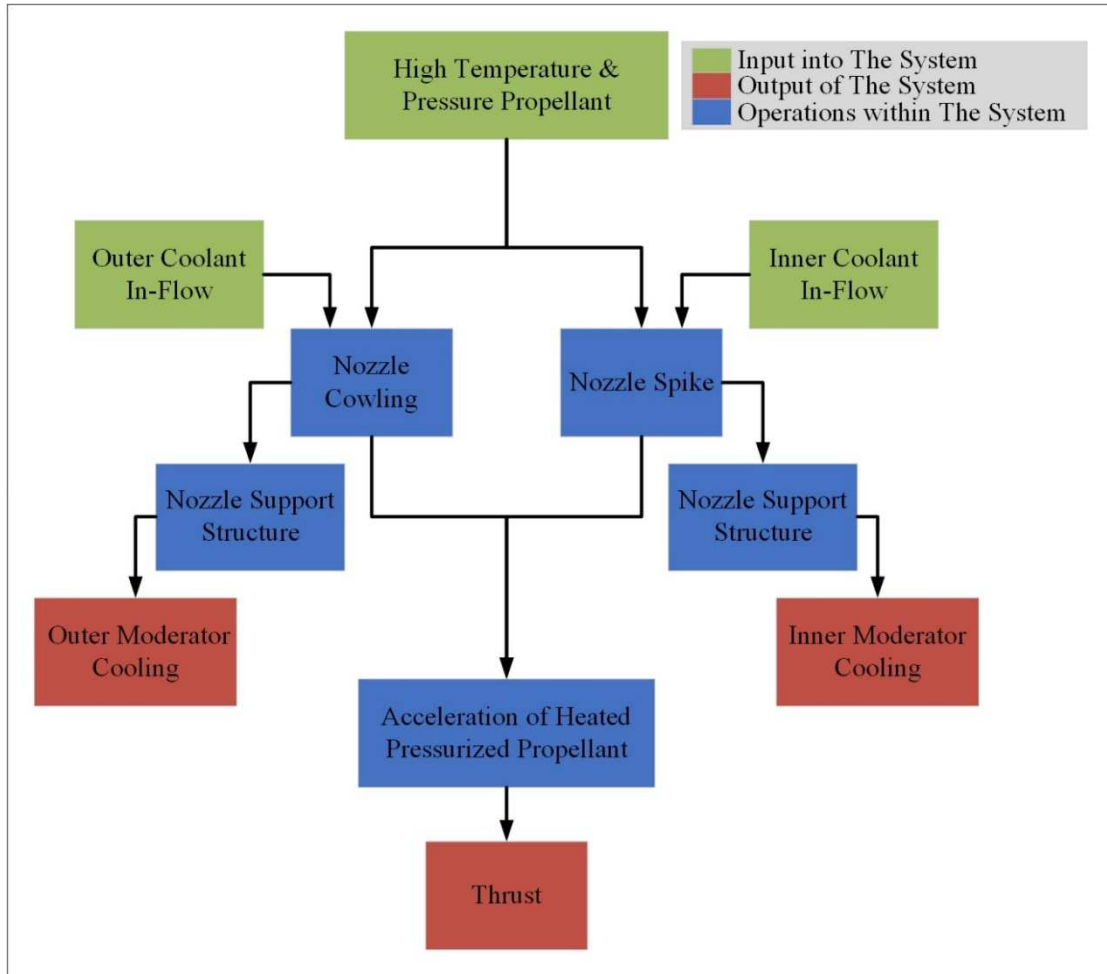


Fig. 39. Flowchart for the nozzle system.

6 COOLANT SYSTEM

6.1 Coolant System Profile

Knowing that the annulus reactor system is the proverbial heart of the Nuclear Thermal Propulsion System, therefore, in the same context, the coolant system would be the circulatory system of the whole propulsion system. The coolant system's purpose is to keep the nozzle system from overheating and supplying the needed power to the propellant feed system while preheating the incoming propellant. The coolant system that is being theorized for the Nuclear Thermal Propulsion System is a variant of a closed expander cycle. Simultaneously, a portion of the cryogenic liquid hydrogen is diverted into the outer and inner coolant channels. The hydrogen will be pressurized to a supercritical phase within the channels to allow for nucleate boiling of the coolant to occur at the point of highest temperatures within the nozzle system. Once the coolant has passed the point of its intended maximum cooling, the fluid is allowed to change from a supercritical phase into a gas phase to facilitate the increase in temperatures of the gas-like fluid. The increase in the gas-like fluid temperature allows for the coolant to be used to drive the turbines within the propellant feed system. After providing the needed energy to the propellant feed system, the heated gaseous coolant is expanded into a heat exchanger to allow for the heated coolant from both the inner and outer flows to be mixed and reinserted into the main propellant flow. By allowing for the coolant and propellant recombination, the coolant can preheat the propellant, reducing the temperature gradient that must be overcome by the annulus reactor system. The other key advantage to this configuration is that the coolant can be re-pressurized to a higher pressure than that was

used in the coolant channels. It is thereby solving one of the limiting factors of a traditional expander cycle, where the pressure of the coolant must be higher than the combustion chamber to allow for the proper flow conditions. In this configuration, the cycle can have the needed pressure for the coolant to maintain the proper heat flux for the given region while allowing the annulus reactor to have a reduced temperature gradient and to maintain the highest pressure to achieve theoretically higher performance than its predecessors [2], [45]–[47].

The interaction of the coolant system with the other three primary systems essentially begins with the cooling of the nozzle system. The inner coolant flow enters the propulsion system through a center coolant channel that runs down the center of both the propellant feed system and the annulus reactor system. Simultaneously the outer coolant flow enters the propulsion system on the outside of the nozzle cowling. The outer coolant flow enters a singular flow direction cooling jacket on the convergent side of the nozzle cowling. Upon exiting the cooling jacket, the now heated outer flow is consolidated and channeled into the nozzle support structure. The inner coolant flow is evenly dispersed into the nozzle spike's longitudinal cooling jacket, as seen in Fig. 40. The trapezoidal-shaped cooling channels allow the incoming coolant to have a wide contact area with the nozzle spike to promote maximum cooling. The adjacent heated coolant return channels are inverted to minimize the contact area of the heat transferable fluid. While the contact areas are reduced for the return channels, the coolant can still gain temperature, thus enabling the flow to be used within the propellant feed system. The inner coolant flow will enter the cooling jacket in a supercritical phase, which exhibits the low viscosity of

gas with the high density of a liquid. By forcing the coolant into this phase, the coolant can maintain the high heat-flux needed to allow the nozzle system to operate for extended durations at the propellant's high exhaust temperature. The coolant will phase change entirely into a gaseous phase near the truncation point on the nozzle spike. The phase change is due to the decrease in pressure upon leaving the cooling channels and entering the return channels. Thus, as the heated coolant flow leaves the return channels, the flow is consolidated and channeled into the nozzle support structure, in much the same way as the heated outer coolant flow [2], [45], [46].

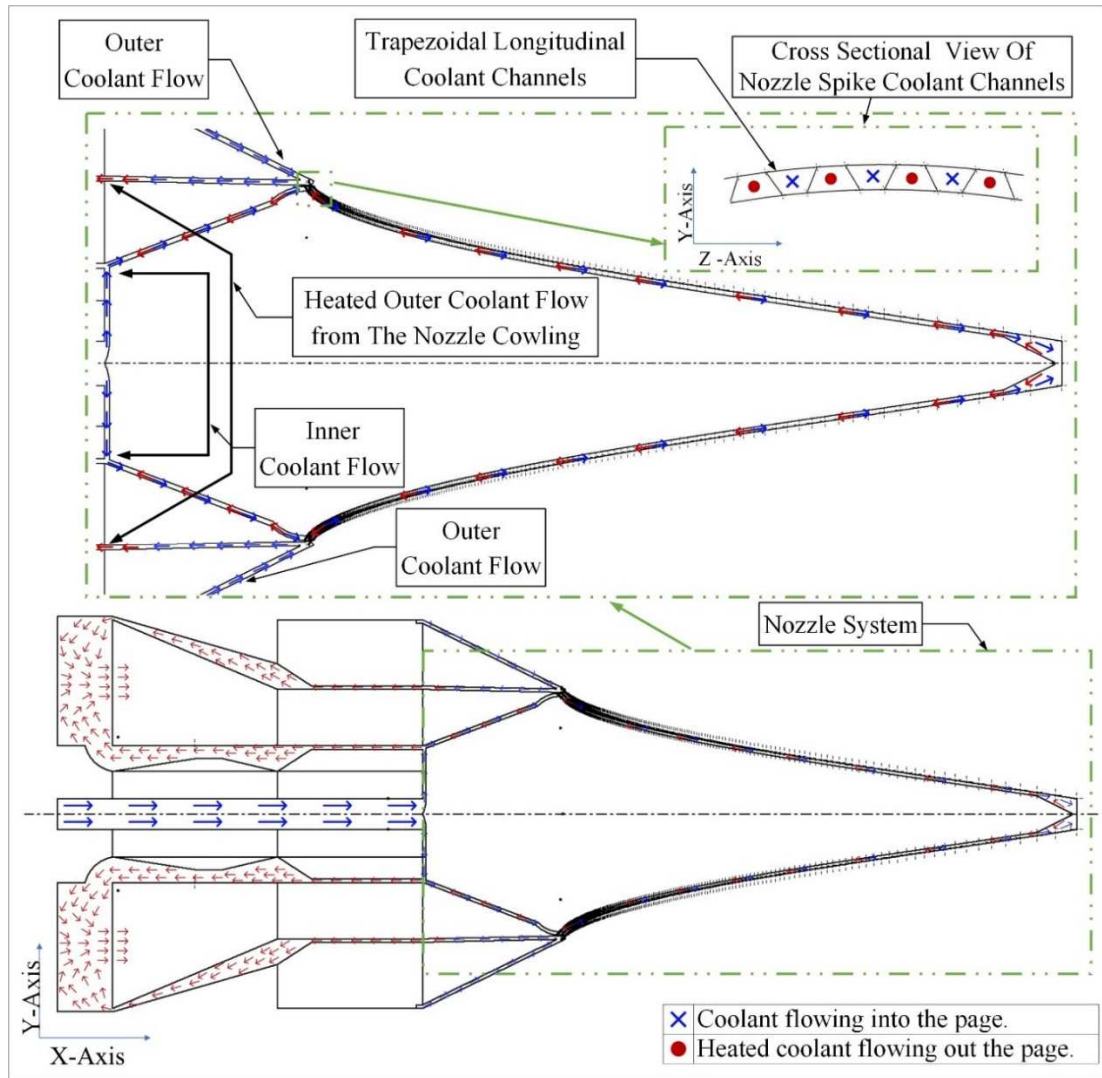


Fig. 40. Coolant system directional flow diagram of the nozzle system.

The second primary system that the coolant system will interact with is the annulus reactor system, even though the coolant flow remains separated from the physical annulus reactor. This separation is due to both heated inner and outer coolant flows being channeled within the nozzle support structure that is set within the annulus reactor. The two flows are channeled into heating jackets around each fuel rod while maintaining the

separation of both inner and outer heated coolant flows. This separation of the two flows is illustrated in Fig. 41. The heating jackets around each fuel rod will exponentially increase the temperature of the coolant. Thus, the coolant system's interaction with the annulus reactor system acts in a similar function as a pre-burner in a staged cycle system. By incorporating this function into both flows of the coolant system, the thermal energy that is gained by the system can be utilized within the propellant feed system [2], [36], [37].

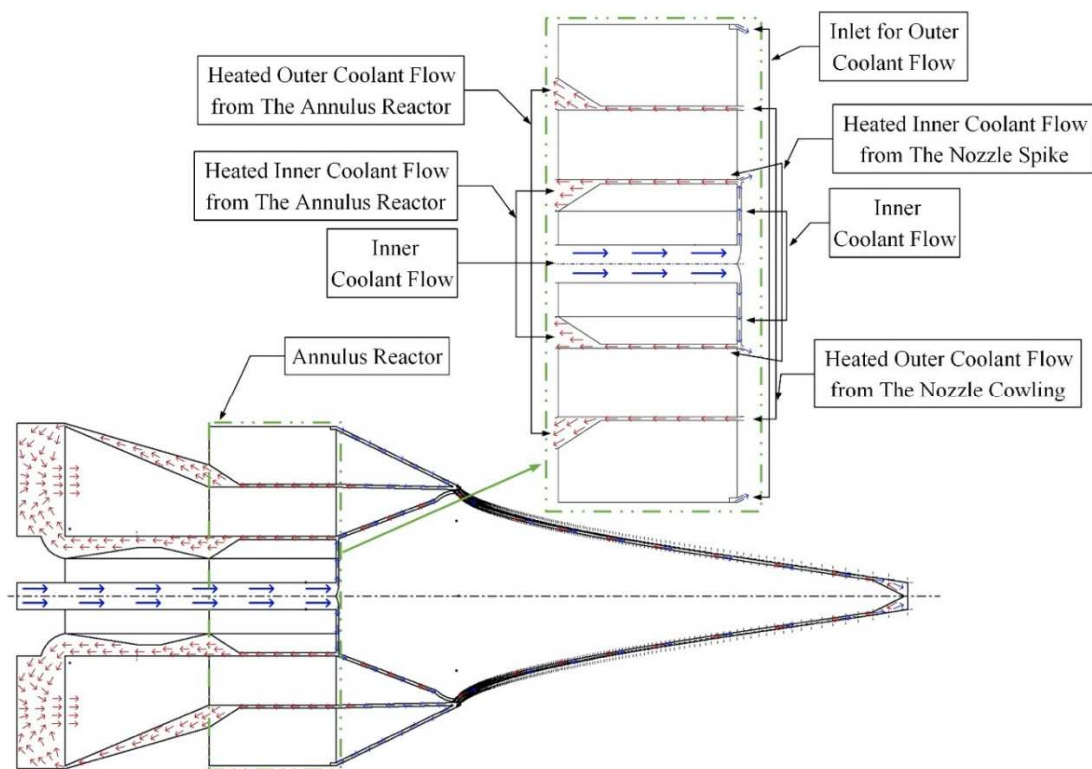


Fig. 41. Coolant system directional flow diagram of the annulus reactor system.

Upon exiting the nozzle support structure, the highly energetic coolant flows enter the propellant feed system, where the inner coolant flow is channeled along the inner wall of the SDPD compressor to the drive turbine of the propellant feed system, as seen in Fig. 42. The inner coolant flow is then diverted into the main propellant flow heat exchanger, allowing the coolant to reduce in pressure before reinsertion into the propellant flow. Simultaneously the outer coolant flow is passed along the outside of the SDPD compressor, where the thermal energy is transferred from the coolant to the compressing propellant through the stator vanes. The propellant flow is under constant preheating throughout the entire propellant feed system. The outer coolant flow will then be diverted into the same main propellant flow heat exchanger as that of the inner coolant flow. The two coolant flows are then mixed and reinserted into the propellant flow prior to entering the SDPD compressor. Thus, allowing the Nuclear Thermal Propulsion System's highest pressures to be at the annulus reactor system entrance. While simultaneously reducing the traditional expander cycle's limitations and solving the cooling issues associated with aerospike nozzles. Thus, by configuring the coolant system in this form, the system can be described as a regenerative cooled, closed staged expander cycle [1], [2], [47].

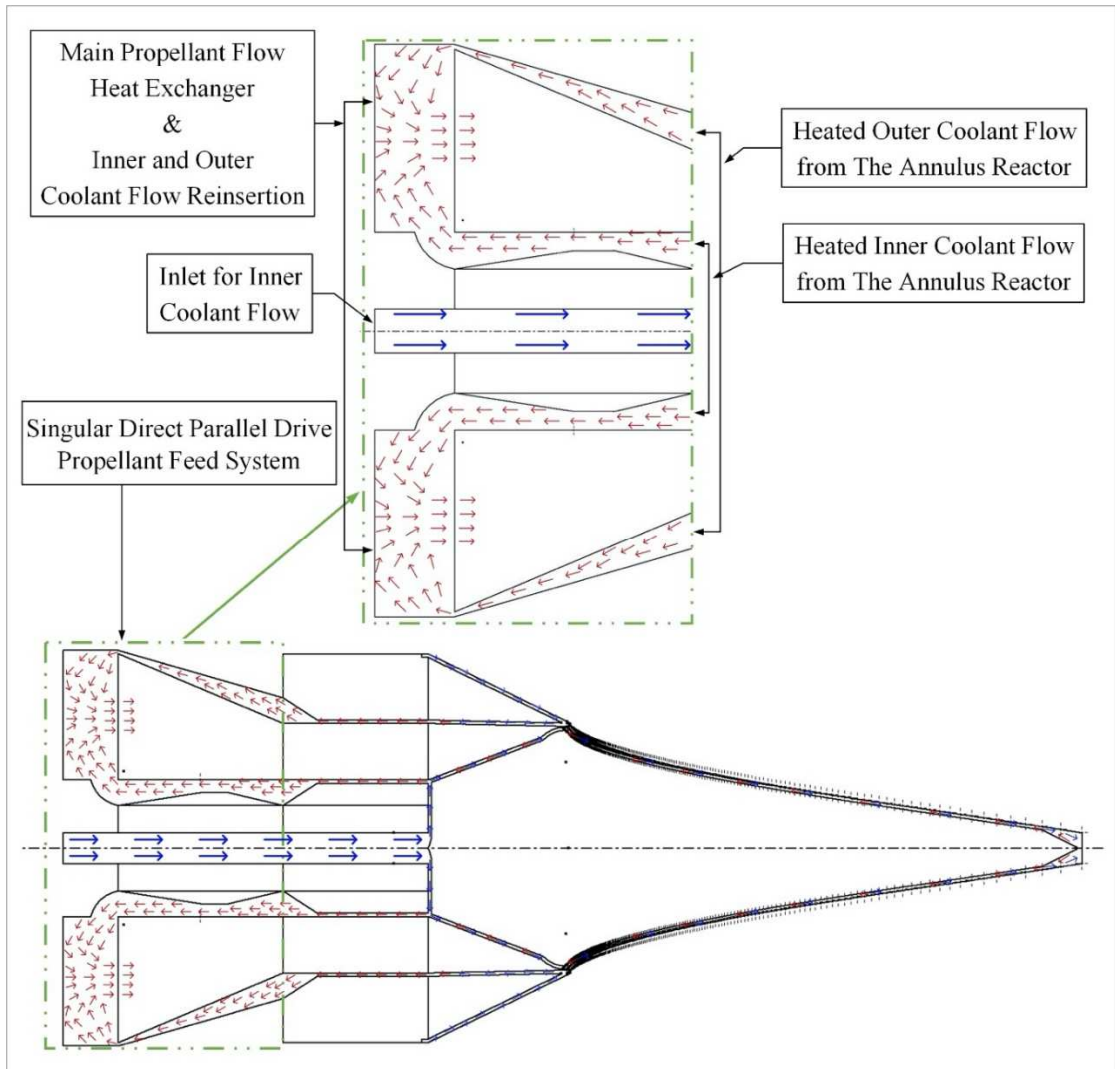


Fig. 42. Coolant system directional flow diagram of the propellant feed system.

6.2 Coolant System Decomposition

Understanding how the coolant system functions throughout the other primary systems, a decomposition of the coolant system will enable the quantification of those individual functions into systems and sub-systems. The decomposition diagram illustrated in Fig. 43 shows how the coolant system can be divided into three tiers. The

first tier is of the coolant system as one of the Nuclear Thermal Propulsion System's four primary systems. The next tier takes the coolant system and divides it into the two major systems that comprise the coolant system as a whole, the inner and outer coolant flows. The inner and outer coolant flows can be split into seven sub-systems, which comprise the decomposition's last tier. Both inner and outer coolant flows have three individual sub-systems, with one joint sub-system being the heat exchanger, where both flows are mixed and reinserted into the propellant flow. The other individual sub-system per coolant flow is directly related to the primary system in which that sub-system occurs. In order to further quantify the sub-systems, they are arranged into sets that pertain to the given primary system in which that sub-system takes place. This arrangement enables the following analysis of the coolant systems integration and architecture to be simplified into the primary systems while representing the sub-systems' interactions within the coolant system [2], [6], [29], [30].

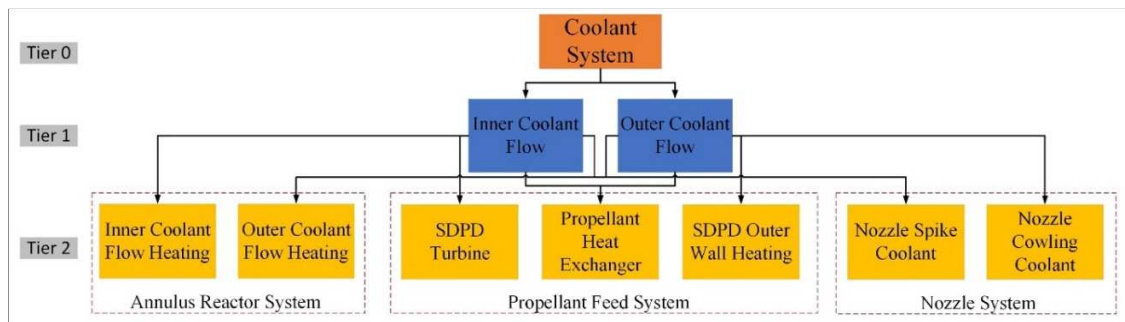


Fig. 43. The coolant system decomposition.

6.3 Coolant System Integration

The coolant system's integration is analyzed through the arranged sets of the sub-systems previously discussed in the coolant system decomposition. By conducting the integration in this manner, the analysis is simple and concise while representing all the complex sub-systems within the coolant system. Fig. 44 illustrates how the three primary systems interact in two ways pertaining to the coolant system. The coolant sub-systems within the nozzle system directly influence the annulus reactor's coolant sub-systems by preheating the incoming gaseous coolant flows, thereby reducing the temperature gradient for the annulus reactor system.

Similarly, the coolant sub-systems of the annulus reactor are integral in the proper functioning of the propellant feed system. The essential interaction between both primary systems is due to the utilization of the high thermal energy coolant flows by the propellant feed system, which the energy is used to preheat and pressurize the incoming propellant to the annulus reactor system, followed by the acceleration of that heated pressurized propellant by the nozzle system to produce thrust [2], [6], [29], [30].

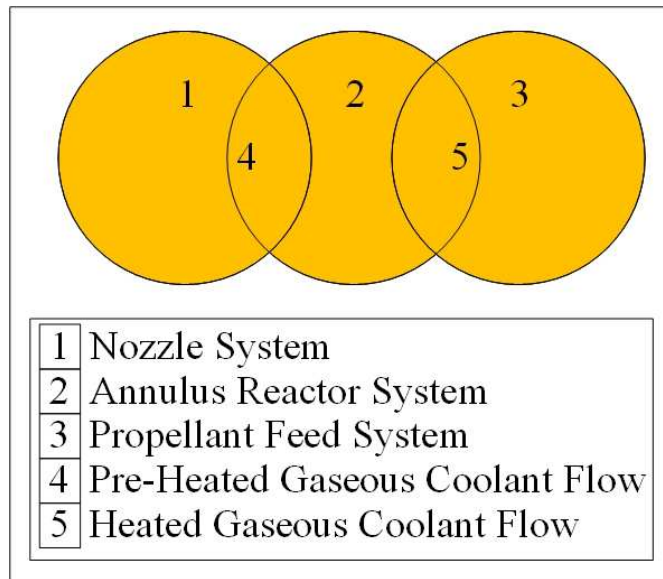


Fig. 44. The integration diagram of the coolant system.

6.4 Coolant System Architecture

An analysis of the coolant system's architecture was constructed to understand how various inputs and outputs into the system maintain the functionality of the Nuclear Thermal Propulsion System. The architecture analysis consists of two stages: the input and output analysis, shown in Fig. 45, and the operational flowchart analysis. The coolant system's input and output analysis comprise the same three sub-systems used in the integration analysis. Upon inspection of the analysis, the progressional flow of both the inner and outer coolant flows from one primary system to the next is all the more apparent. This progression is the sequence, as previously described in the coolant system profile section of this chapter. This sequence represented in Fig. 45, and Table 15 below illustrates how the coolant system can simultaneously provide the needed power, propellant preheating, and structural integrity. Although the system is complex, through

Fig. 45, the coolant flows' progression is refined to a simple and concise form, allowing for a better understanding of the coolant system's inputs and outputs [29], [30].

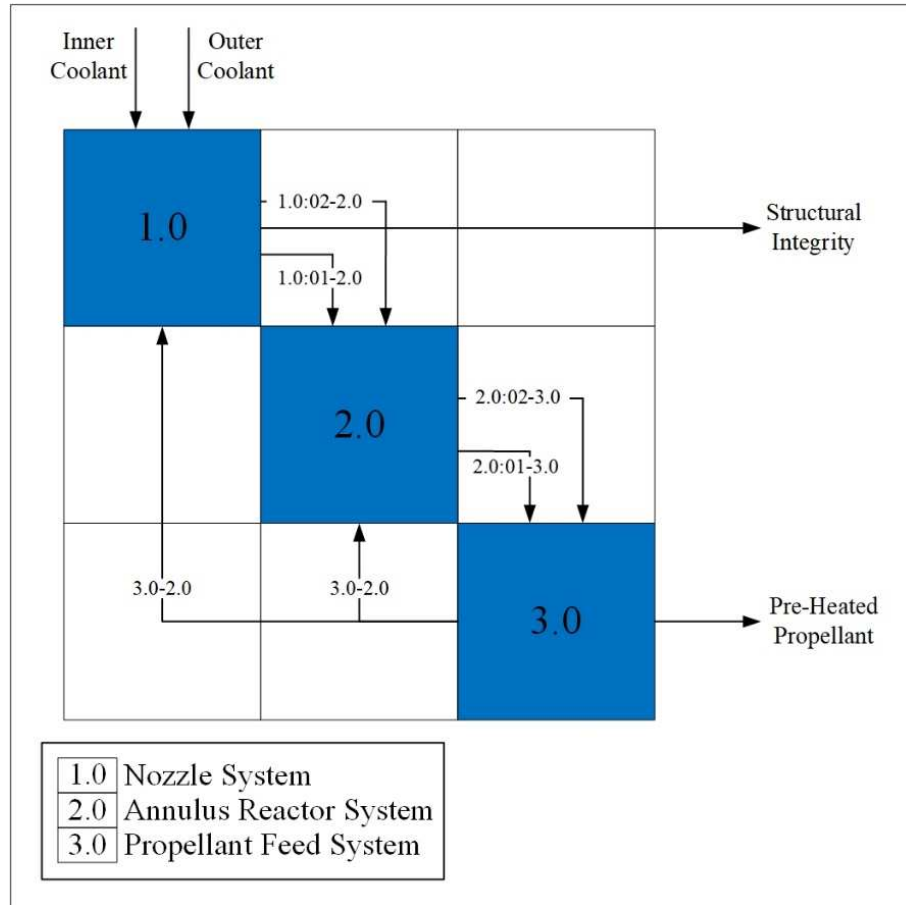


Fig. 45. N² diagram for the coolant system.

Table 15
Inputs and Outputs of the Coolant System N² Diagram

The Direction of Input & Output	Performed Operation
In → 1.0	Inner Coolant Flow
In → 1.0	Outer Coolant Flow
1.0: 01 → 2.0	Preheated Inner Coolant Flow
1.0: 02 → 2.0	Preheated Outer Coolant Flow
1.0 → Out	Structural Integrity
2.0: 01 → 3.0	Heated Inner Coolant Flow
2.0: 02 → 3.0	Heated Outer Coolant Flow
3.0 → Out	Preheated Propellant
3.0 → 1.0	Pressurized Coolant
3.0 → 2.0	Pressurized Propellant

The operational flowchart analysis of the coolant system architecture enables a more comprehensive understanding of how it maintains the Nuclear Thermal Propulsion System's functionality. The operational flowchart also combines aspects of the decomposition and the coolant system's input and output analysis to define individual sub-system interactions. Therefore, to conduct this analysis, the operational flowchart is orientated in the same progression sequence that has been used throughout the other system analysis. Fig. 46 illustrates the flow in combination with various inputs and outputs to the coolant sub-systems. Through the figure below, the reasoning of the flow sequence orientation becomes more prevalent. This prevalence is due to the emergence of the dominating functions of the coolant sub-system within the nozzle and annulus reactor systems. The operational flowchart analysis illustrates that the coolant sub-systems' first function within these two primary systems is to gain the needed thermal energy for the propellant feed system. Thus, the inputs into the coolant sub-system within the nozzle

and annulus reactor systems are thermal energy, either from the nozzle or reactor. The thermal energy gain by the coolant system is distributed throughout various aspects of the propellant feed system. It is thereby enabling the propellant feed system to preheat and pressurize the propellant prior to the annulus reactor system. Thus, it completes the operational flowchart analysis and solidifies the coolant system's functionality within the Nuclear Thermal Propulsion System [29], [30].

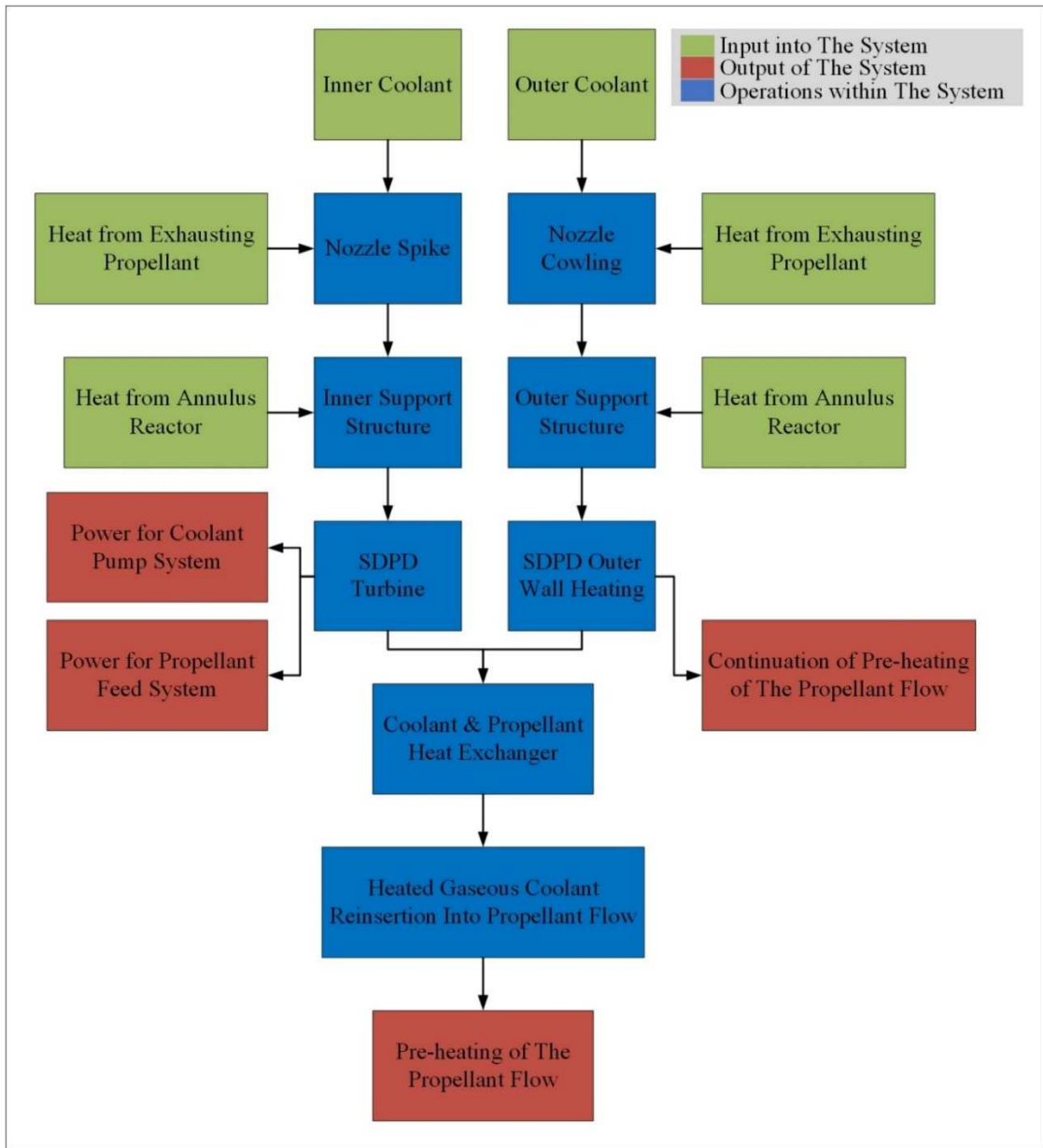


Fig. 46. Operational flowchart diagram of the coolant system.

7 ANALYSIS OF THE ANNULUS REACTOR AND NOZZLE SYSTEMS

The following analysis was conducted with the assistance of Jordan Pollard, who aided in constructing the computational fluid dynamics models and running the simulations for both the annulus reactor and nozzle systems.

7.1 Annulus Reactor System Analysis

To aid in designing the annulus reactor system, an investigation into the characteristics of heat transfer and flow through the six fuel rods was undertaken using the computational fluid dynamics (CFD) program ANSYS Fluent. The analysis was accomplished with a two-dimensional symmetry model of the center channels across a puck diameter, as illustrated below. In order to fully determine the performance and capabilities of the annulus reactor, the implementation of different model configurations was required. The differing models were tested at varying conditions for comparison of the capabilities of each model. The first configuration model consisted of each fuel puck separated from each other. The second model was an arrangement of all six fuel pucks as a non-separated, solid length reactor. The separated fuel puck model analysis had to be conducted as a separate performance run due to the CFD software's limitations. The limitations were averted by using a fuel puck's existing conditions as the following one's initial condition. The CFD software did not limit the non-separated model; therefore, the varying conditions were run individually for each case. The subsequent sections describe the process by which the geometry of the fuel puck was created, grid generation, topology, and physics are also discussed.

The two configurations use a planar approximation of the fuel puck geometry, where the center 49 channels that comprise the diameter is used as the planar profile. The 49 channels are further divided into half of 24.5 channels comprising a radius combined, allowing the planar approximation to be fully symmetric, as seen in Fig. 47. The use of symmetry allowed for the increase in the mesh generation fidelity while simultaneously reducing the computational requirements associated with each simulation. The symmetric planar view geometry and the spacing at the front and back of the fuel pucks were created through ANSYS Spaceclaim and modified in ANSYS Design Modeler to distinguish the solid and fluid cell zones of each model. The non-separated configuration was constructed using the same method, excluding the separation between each puck.

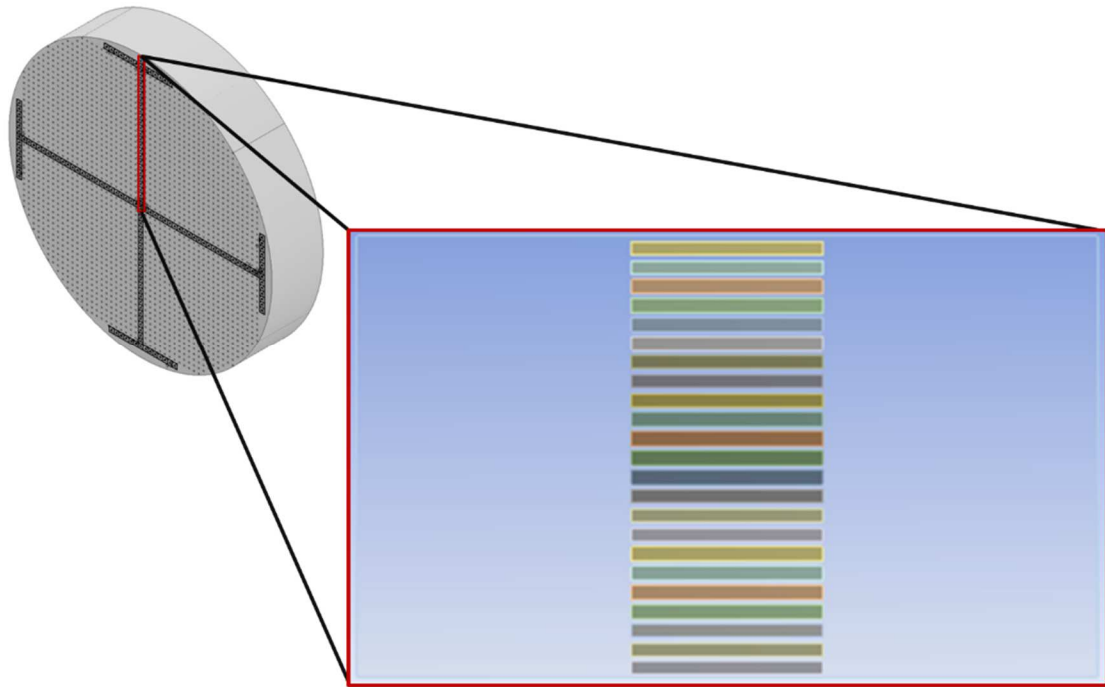


Fig. 47. Single tri-carbide fuel puck planar approximation.

Utilizing the geometry generation method discussed earlier, a 2D mesh was created in ANSYS Fluent Meshing. The structured mesh is an H-mesh configuration, with the center channels having a higher cell count to account for boundary layer formation across the geometry. However, the solid cell zones within the model received a lower fidelity meshing. The constant values enable a structure without sacrificing the accuracy of the model. In order to create a viable mesh, the following settings were used to generate the mesh.

1. Face Meshing was applied to each of the separated interior faces and set to quadratic.
2. The edge sizing function was applied to some 2D geometry edges and set to the different element sizes.
3. The Automatic Method function was implemented to ensure the mesh quality, mainly skewness, and orthogonality separation.

The fore and aft sections of the individual fuel puck and non-separated model were segmented with interior lines for the mesh's topology. The now structured topological configuration allows for a reasonably dense mesh around areas that experience a gradient in the boundary flow. The topology used within both separated and non-separated models can be seen in Fig. 48 [48].

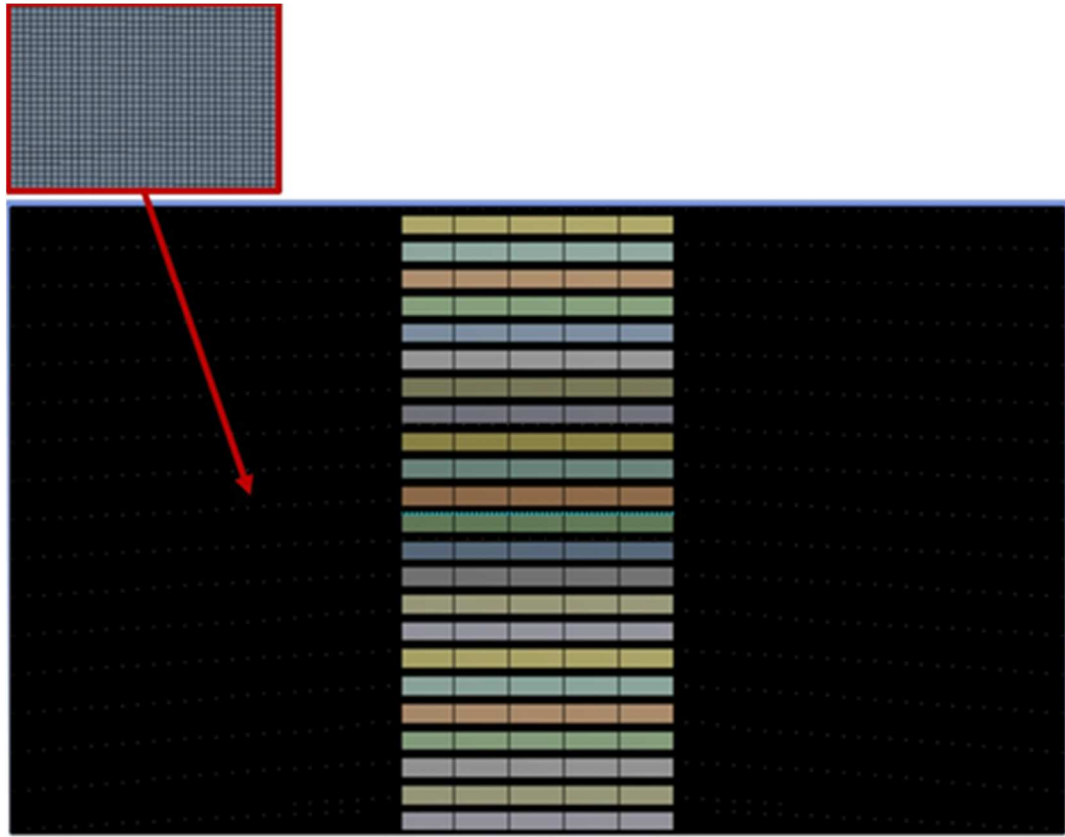


Fig. 48. The structured meshing of the tri-carbide fuel puck.

The physics conditions for both the separated and non-separated reactor models included the following general settings, boundary conditions, operating conditions, solution methods, and solution initialization outlined in Tables 16-19 for each field. The reactor model's general settings utilize a pressure-based, steady-state solver with a K-Epsilon Realizable turbulence model. The pressure-based solver was chosen for its frequent utilization in low-velocity flows, such as the sub-sonic flows within the fuel pucks' heating channel. The pressure-based solver is solved sequentially due to the nonlinear governing equations. The K-Epsilon Realizable is an improved version of one

of the first complete turbulence models and is reasonably accurate for a wide range of turbulent flow analyses. Ideal hydrogen gas was chosen as the fluid model to reflect the propellant used within the NTPS and compressibility within the annulus reactor system. The P1 radiation model was then implemented as it is the simplest case of the more general P-N model; thus, the model is oriented around expanding the radiation intensity I into an orthogonal series [48].

Table 16
Annulus Reactor Analysis: General Settings

General Settings	
Conditions	Settings
General Solver	Pressure Based
Simulation State	Steady State
Velocity Formulation	Absolute
Geometric settings	Symmetric about the X-axis
Energy equation	On
Viscous Model	K-epsilon Realizable
Fluid Model	Hydrogen Gas (Ideal Gas)
Radiation Model	P1 Radiation

The model's boundary conditions reflect the annulus reactor system's desired conditions as approximated for a fuel puck's center 49 channels. The inlet conditions are the exiting condition of the propellant feed system such that the pressure is 6.89 MPa, a temperature of 300 K, and a total mass flow rate of 129 kg/s. The mass flow rate was then approximated to be 0.74 kg/s experienced by the 49 center channels. The outlet conditions were set to compliment the inlet conditions of pressure and temperature to ensure the proper flow conditions. The wall conditions were set such that the cell zone

temperature was a constant 3000 K, with heat generation and heat transfer coefficients set to 3000 W/m³ and 50 W/m² K to emulate the annulus reactor system correctly.

Table 17
Annulus Reactor Analysis: Boundary Conditions

Boundary Conditions			
Settings	Inlet (Mass Flow)	Outlet (Pressure)	Walls (Mixed)
Gauge Pressure	6,890,000 Pa	6,860,000 Pa	N/A
Operating Pressure	0 Pa	0 Pa	0 Pa
Total Temperature	300 K	300 K	3000 K
Mass Flow Rate	0.74 kg/s	N/A	N/A
Heat transfer coefficient	N/A	N/A	50 W/m ² K
Free Stream Temperature	300 K	300 K	300 K
Heat Generation Rate	N/A	N/A	3000 W/m ³

In the case of the solution methods, the settings for the simulation are in Table 18. The Second-Order Upwind formulation was utilized to provide greater accuracy in the results. The use of the above formulation is more crucial, given that a structured mesh was utilized, meaning that the convergence discrepancy is mostly offset.

Table 18
Annulus Reactor Analysis: Solution Methods

Solution Methods	
Settings	Type
Formulation	Implicit Formulation
Flux type	Roe-FDS
Gradient	Least Squares Cell-Based
Flow	Second-Order Upwind

In order to ensure accurate analysis results, a grid independence study was conducted to generate several independent meshes in ANSYS Fluent and test the results from each against the primary case. The testing process determined a minimum of approximately 85000 nodes for the simulation to exhibit the desired heat transfer and flow properties

characteristics. Finally, the simulation accuracy was simulated until the convergence of at least three orders of magnitude [48].

Table 19
Annulus Reactor Physics: Solution initialization

Solution Initialization	
Settings	Type
Initialization Method	Standard Initialization
Computation Reference	From Inlet
Reference Frame	Relative to Cell Zone
Number of Iterations	2000

Through the utilization of the simulation methodology, eight annulus reactor system simulation tests were constructed to ascertain the capabilities and limits of the fuel puck geometry and configuration. The results of each simulation are tabulated in Tables 20-27, in which the temperature is listed as the exit temperature per puck as well as the total exit temperature of the non-separated model. The related contours and graphs of pressure, velocity, and temperature within each model are shown below in Fig. 49-51.

The first simulation initial values are meant to reflect the baseline operating conditions of the NTPS. The hydrogen experienced a temperature increase on average of 427.5 K as it passed through each puck's heating channels, culminating in a total temperature of 2865 K at the exit of the core assembly. This value was corroborated through the non-separated model producing a final exit temperature of 2863 K. Due to the large cross-sectional flow area of each fuel puck, the flow did not experience a significant increase in velocity and accelerated only to 5.0m/s though each channel. The minimal change in velocity resulted in a negligible pressure drop experienced across each fuel puck. Fig. 49-51 represent the values change for the temperature, pressure, and

velocity in Test # 1 across the planar approximation of fuel puck three within the fuel rod.

Table 20
Annulus Reactor System Simulation Test #1

Reactor Test #1: Baseline Core Run	
Conditions	Values
Wall Temperature (K)	3000
Mass flow Rate (Kg/s)	129
Pressure (MPa)	6.89
Core inlet Temperature (K)	300
Temperature after Puck 1 (K)	1245
Temperature after Puck 2 (K)	1785
Temperature after Puck 3 (K)	2325
Temperature after Puck 4 (K)	2460
Temperature after Puck 5 (K)	2595
Temperature after Puck 6 (K) - Exit	2865
Exit Temperature of the Non-Separated model (K)	2863

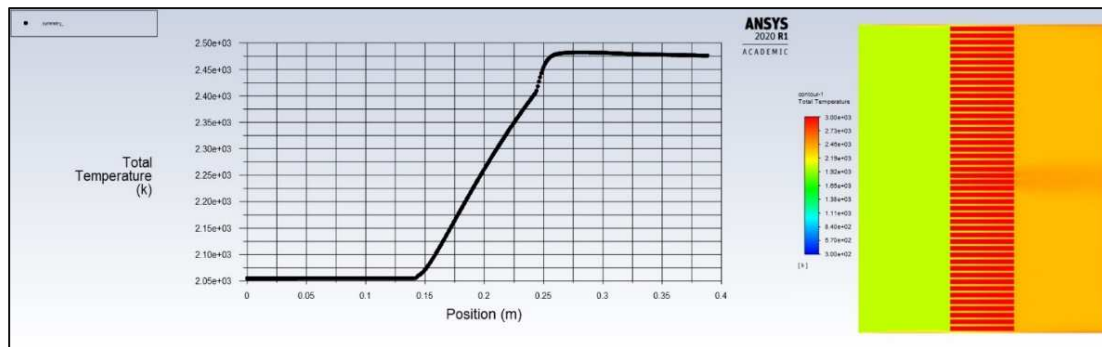


Fig. 49. Temperature profile from puck #3 test #1.

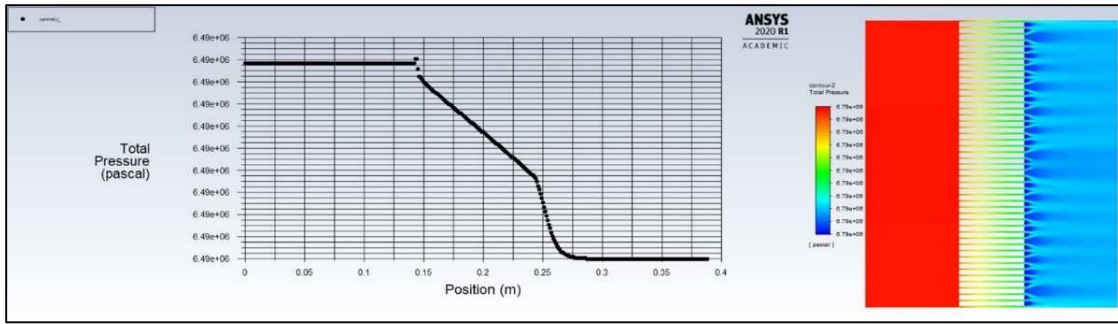


Fig. 50. Total pressure profile from puck #3 test #1.

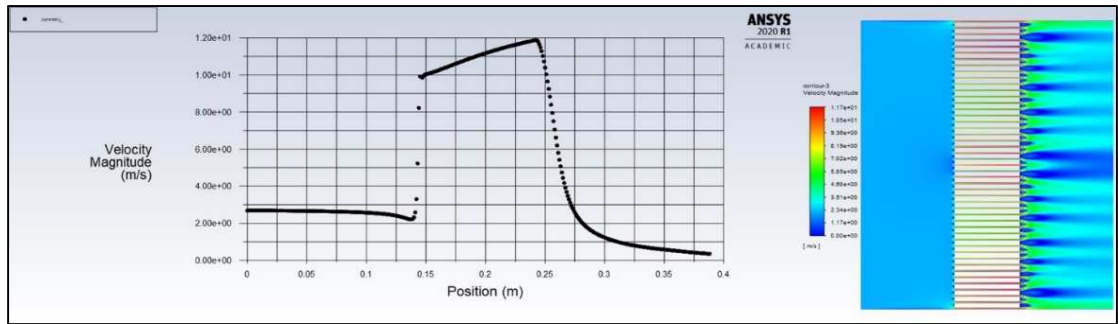


Fig. 51. Velocity profile from puck #3 test #1.

The second test was conducted at the actual operating conditions produced by the Phoebus-2A engine, where the wall temperature of the model was set to the reactor core temperature of the Phoebus-2A during testing. Test #2 established a benchmark simulation to determine the accuracy of its results of the ANSYS model. The propellant experienced a temperature increase of 309.5 K on average as it passed through the heating channels of each fuel puck, culminating in a total exit temperature of 1929 K; additionally, it was noted that the increase in temperature attenuated as the flow passed through the channels of each puck, as seen in Table 21. In the non-separated model, the

annulus reactor system produced a final exit temperature of 2147 K, resulting in a much closer value to that of the historical value of the Phoebus-2A. Similarly to Test #1, the flow did not experience a significant increase in velocity resulting in a negligible average pressure drop experienced by the annulus reactor system, ensuring minimal losses throughout the system [49].

Table 21
Annulus Reactor System Simulation Test #2

Reactor Test #2: Reflecting Phoebus-2A Performance	
Conditions	Values
Wall Temperature (K)	2256
Propellant Temperature Benchmark(K)	2158.2
Mass flow Rate (Kg/s)	119
Pressure (MPa)	3.827
Core inlet Temperature (K)	77.6
Temperature after Puck 1 (K)	731.1
Temperature after Puck 2 (K)	1166.8
Temperature after Puck 3 (K)	1493.5
Temperature after Puck 4 (K)	1711.4
Temperature after Puck 5 (K)	1820.3
Temperature after Puck 6 (K) - Exit	1929.2
Exit Temperature of the Non-Separated Model (K)	2147
Historical Exit Temperature	2283

The third test of the annulus reactor system was run at the determined fissile material temperature required to reach the ideal propellant exit temperature of approximately 3000 K. The needed wall temperature was determined to be 3350 K; the average temperature increase experienced by the hydrogen was 457.5 K as it passed through each fuel puck, resulting in an exit temperature of 3045 K and 3197 K, as seen in Table 22. In Test #3, it

was noted that the non-separated model provided better performance at the higher wall temperatures.

Table 22
Annulus Reactor System Simulation Test #3

Reactor Test #3: Finding Wall Temp. For Propellant Temp.	
Conditions	Values
Wall Temperature (K)	3350
Mass flow Rate (Kg/s)	129
Pressure (MPa)	6.89
Core inlet Temperature (K)	300
Temperature after Puck 1 (K)	1367.5
Temperature after Puck 2 (K)	2130
Temperature after Puck 3 (K)	2587.5
Temperature after Puck 4 (K)	2730
Temperature after Puck 5 (K)	2892.5
Temperature after Puck 6 (K) - Exit	3045
Exit Temperature of the Non-Separated Model (K)	3197.5

Test #4 evaluated the reactor core assembly at half of the maximum operating temperature, such that the constant wall temperature was set to be 3250 K with the inlet pressure set to 6.89 MPa. The average increase in propellant temperature was observed to be 449.2 K, with the final exit temperatures of both separated and non-separated models exhibiting exit temperatures of 2955 K and 3102.5 K, respectively, as seen in Table 23 below.

Table 23
Annulus Reactor System Simulation Test #4

Reactor Test #4: Half Max Wall Temp	
Conditions	Values
Wall Temperature (K)	3250
Mass flow Rate (Kg/s)	129
Pressure (MPa)	6.89
Core inlet Temperature (K)	300
Temperature after Puck 1 (K)	1380
Temperature after Puck 2 (K)	2070
Temperature after Puck 3 (K)	2512.5
Temperature after Puck 4 (K)	2660
Temperature after Puck 5 (K)	2807.5
Temperature after Puck 6 (K) - Exit	2955
Exit Temperature of the Non-Separated Model (K)	3102.5

The fifth test consisted of the fissile material at the maximum allowable operating temperature for the annulus reactor system of 3500 K. While simultaneously allowing inlet pressure to remain at the nominal operating pressure of 6.89 MPa. At the maximum allowable operating wall temperature, the average increase in propellant temperature between the fuel pucks was 480 K. The final exit temperatures of both separated and non-separated models were 3180 K and 3340 K, as displayed in Table 24.

Table 24
Annulus Reactor System Simulation Test #5

Reactor Test #5: Max Wall Temp.	
Conditions	Values
Wall Temperature (K)	3500
Mass flow Rate (Kg/s)	129
Pressure (MPa)	6.89
Core inlet Temperature (K)	300
Temperature after Puck 1 (K)	1520
Temperature after Puck 2 (K)	2220
Temperature after Puck 3 (K)	2700
Temperature after Puck 4 (K)	2860
Temperature after Puck 5 (K)	3020
Temperature after Puck 6 (K) - Exit	3180
Exit Temperature of the Non-Separated Model (K)	3340

Test #6 and # 7 were constructed in much the same way as Test #1, with the fissile material at the nominal operating temperature of 3000 K; however, the pressure was set to half, and the maximum allowable operating pressures of 15.71 MPa and 24.52 MPa. The performance reflected in Test #6 and #7 is nearly identical to that of Test #1, such that the average and final temperatures of the tests, in particular the non-separated model, are negligible. As a result, it was noted that there was no performance degradation in the heat transfer between the propellant and fissile material due to the increase in the inlet pressure, shown in Tables 25 and 26.

Table 25
Annulus Reactor System Simulation Test #6

Reactor Test #6: Half Max inlet Pressure	
Conditions	Values
Wall Temperature (K)	3000
Mass flow Rate (Kg/s)	129
Pressure (MPa)	15.71
Core inlet Temperature (K)	300
Temperature after Puck 1 (K)	1245
Temperature after Puck 2 (K)	1920
Temperature after Puck 3 (K)	2190
Temperature after Puck 4 (K)	2460
Temperature after Puck 5 (K)	2595
Temperature after Puck 6 (K) - Exit	2730
Exit Temperature of the Non-Separated Model (K)	2865

Table 26
Annulus Reactor System Simulation Test #7

Reactor Test #7: Max inlet Pressure	
Conditions	Values
Wall Temperature (K)	3000
Mass flow Rate (Kg/s)	129
Pressure (MPa)	24.52
Core inlet Temperature (K)	300
Temperature after Puck 1 (K)	1245
Temperature after Puck 2 (K)	1920
Temperature after Puck 3 (K)	2325
Temperature after Puck 4 (K)	2460
Temperature after Puck 5 (K)	2595
Temperature after Puck 6 (K) - Exit	2730
Exit Temperature of the Non-Separated Model (K)	2865

The final test consisted of the maximum allowable operating values for both temperature and pressure, such that the constant wall temperature was set to be 3500 K, and the pressure was set to 24.52 MPa. As with the other pressure variant tests, the increase in propellant temperature was driven by the fissile material, and the increase in

the inlet pressure conditions resulted in no performance degradation in the heat transfer to the propellant, as seen in Table 27.

Table 27
Annulus Reactor System Simulation Test #8

Reactor Test #8: Max Inlet Pressure & Wall Temp.	
Conditions	Values
Wall Temperature (K)	3500
Mass flow Rate (Kg/s)	129
Pressure (MPa)	24.52
Core inlet Temperature (K)	300
Temperature after Puck 1 (K)	1520
Temperature after Puck 2 (K)	2220
Temperature after Puck 3 (K)	2700
Temperature after Puck 4 (K)	2860
Temperature after Puck 5 (K)	3020
Temperature after Puck 6 (K) - Exit	3180
Exit Temperature of the Non-Separated Model (K)	3340

The following figures represent the two tested annulus reactor system configurations, the separated and non-separated models, in regards to the temperature contours of the eight conducted tests. Fig. 52 and 53 provide a detailed view of the flow physics, specifically the boundary layer formation and heat transfer within the center flow channels.

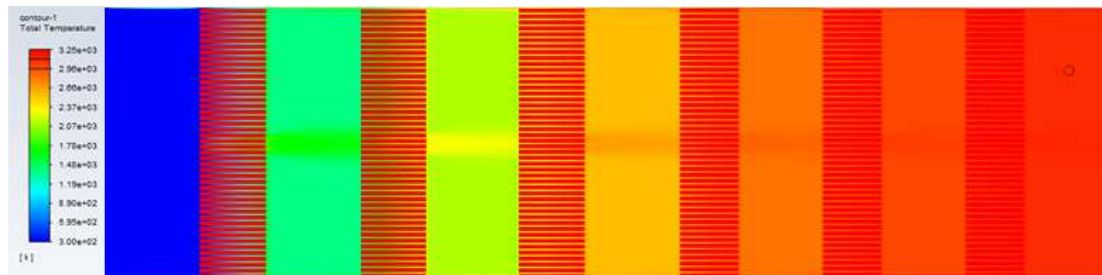


Fig. 52. Temperature contours of full puck assembly.

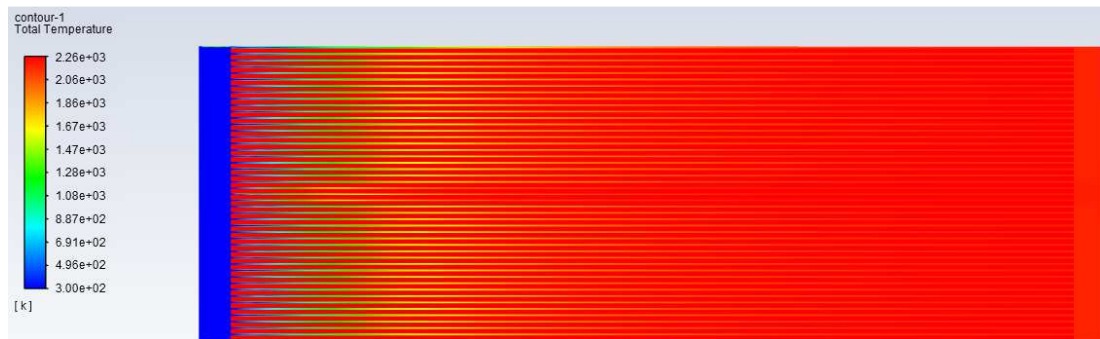


Fig. 53. Temperature contour for non-separated configuration.

The results of the annulus reactor system analysis yielded the trends seen in Fig. 54-56 below. These figures show the temperature increase along the X-axis of the models highlighted by the fuel puck order number. It was observed that the temperature increase of the propellant attenuates across the fissile material, with a steady increase in temperature. However, it was noted that in the separated model, temperatures reducing sharply just passed the third puck of each test. The non-separated model exhibited similar behavior at the equivalent point in the model during each analysis. The test results show that the highest performing model is the baseline separated model with a wall temperature of 3000 K, which outperforms both the non-separated model and historical data for similar conditions.

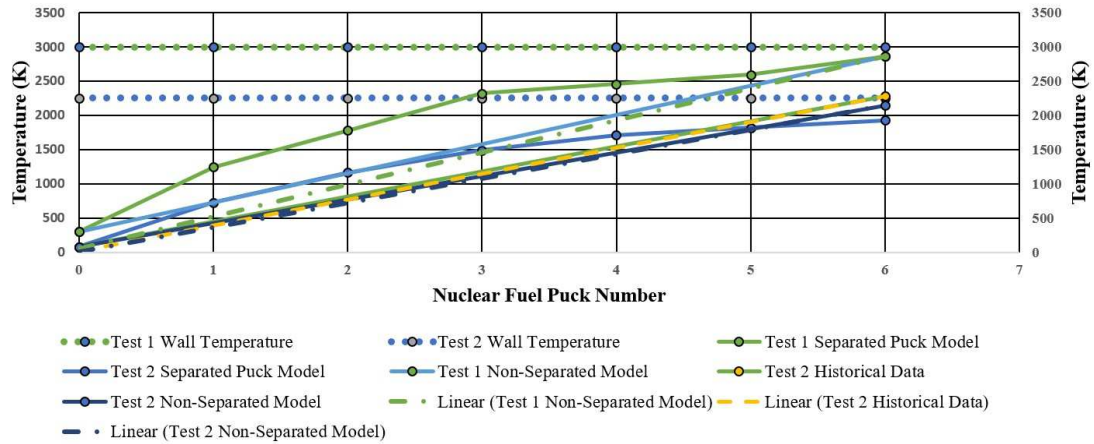


Fig. 54. Annulus reactor system test #1-2 result comparison.

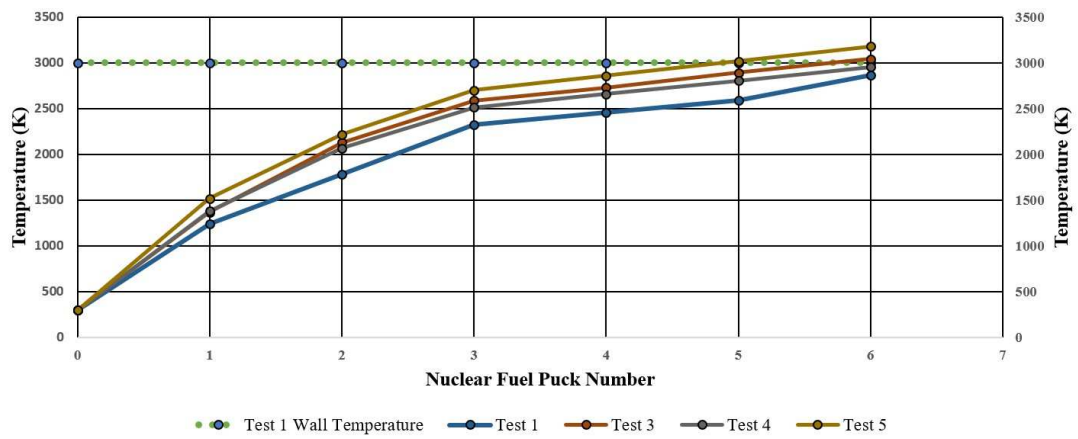


Fig. 55. Annulus reactor system test #3-5 result comparison.

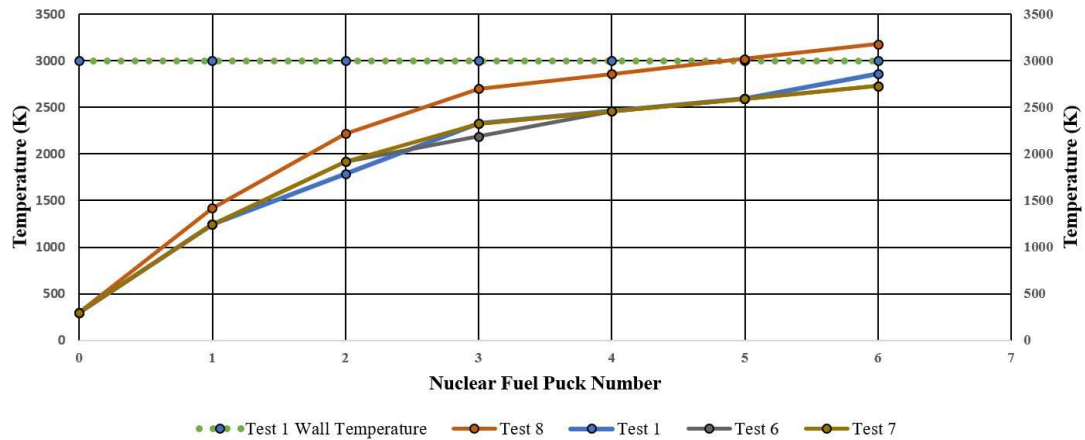


Fig. 56. Annulus reactor system test #6-8 result comparison.

7.2 Nozzle System Analysis

A nozzle system performance characterization was performed using ANSYS Fluent in addition to analyzing the characteristics of flow and heat transfer in the annulus reactor system. The subsequent analysis was constructed as a two-dimensional axisymmetric profile of the nozzle spike and cowling geometry under various atmospheric conditions and chamber pressures. The nozzle geometry was generated in a MATLAB program using a step-by-step method outlined below and in the “Optimal Design of Annular Aerospike Engine Nozzle.” The article implemented a Prandtl–Meyer expansion fan calculation method using the equations listed in Equation 12-23.

The following is a step-by-step outline of the method used to construct the exit contour of the nozzle. The nozzle set parameters were a mass flow rate of 129 kg/s, a gamma equal to 1.405, the chamber temperature set to 3000 K, and a chamber pressure of 6.8 MPa.

1. The throat area was calculated based on the set parameters and Equation 12.

$$A^* = \frac{T}{P_0 \cdot C_F} \quad (12)$$

2. An appropriate exit Mach number was selected and verified for the nozzle with Equation 13.

$$M_e = \sqrt{\left\{ \left(\frac{P_t}{P_{inf}} \right)^{\frac{\gamma-1}{\gamma}} - 1 \right\} \cdot \frac{2}{\gamma-1}} \quad (13)$$

3. An array of ν values were calculated with a changing Mach number starting at 1 and increasing to the exit Mach number of 3.98 with Equation 14.

$$\nu = \sqrt{\frac{\gamma+1}{\gamma-1}} \cdot \tan^{-1} \sqrt{\frac{\gamma-1}{\gamma+1} (M^2 - 1)} - \tan^{-1} \sqrt{M^2 - 1} \quad (14)$$

4. An array of μ values were calculated in the same manner as the ν values with Equation 15.

$$\mu = \sin^{-1} \left(\frac{1}{M} \right) \quad (15)$$

5. The α angle and throat area ratio was established with the Equations 16-18.

$$\alpha = \theta_t - \nu + \mu \quad (16)$$

$$\frac{A^*}{A} = M \cdot \left[\frac{2}{\gamma + 1} \cdot \left(1 + \frac{\gamma - 1}{2} \cdot M^2 \right) \right]^{-\frac{\gamma + 1}{2 \cdot (\gamma - 1)}} \quad (17)$$

$$\beta = \frac{A}{A^*} \quad (18)$$

6. The exit area was established with the manipulation of the above equations.

7. The exit radius, exit area ratio, and the contour radius at various X-axis locations were calculated with the following Equations 19-21.

$$r_2 = \sqrt{\frac{A_e}{\pi}} \quad (19)$$

$$\epsilon = \frac{A_e}{A^*} \quad (20)$$

$$r_x = r_2 \cdot \sqrt{1 - \frac{\beta}{\epsilon} \cdot \cos(\theta_t - \nu)} \quad (21)$$

8. The length for a given expansion fan wave emanating from the tip of the nozzle cowl to the contour of the spike was calculated with Equation 22.

$$l = \frac{r_2 - r_x}{\sin \alpha} \quad (22)$$

9. The contour's full length was established when X was set to 0 with Equation 23.

$$X_{end} = l \cdot \cos \alpha \quad (23)$$

10. The above step-by-step method was used to generate a contour in MATLAB, which was mirrored over the X-axis to complete the nozzle spike contour. The nozzle's convergent slope section was formed using a small section of the spike contour mirrored over the Y-axis. Thus, the following aerospike dimensions are stated in Table 28, which corresponds to the 2-dimensional contour diagrams in Fig. 33 and 34 [44].

Table 28
The Test Aerospike Dimensions

Dimension	Length (meters)
L_{NS}	2.752
L_{cn}	.639
r_1	.660
r_T	.109
r_t	.037362
r_{AC}	.653

The expansion fan calculations are based on the nozzle cowling's location and distances relative to the nozzle spike. The two-dimensional geometry was imported as a series of points into a CAD program, which was then used to generate the geometry within ANSYS Spaceclaim, seen in Fig. 57 and 58 below [44].

Once the geometry was imported into ANSYS, a cartesian structured mesh was generated of the nozzle and flow field. The mesh generation was done by separating the body topology into a series of interior faces to ensure a reasonably dense mesh quality at the desired areas across the two-dimensional profile. The mesh cell density was concentrated closer to the nozzle throat and long spike to characterize fluid flow within

the nozzle system and the exhausting propellant as accurately as possible. The subsequent mesh generated can be seen in the following two figures below.

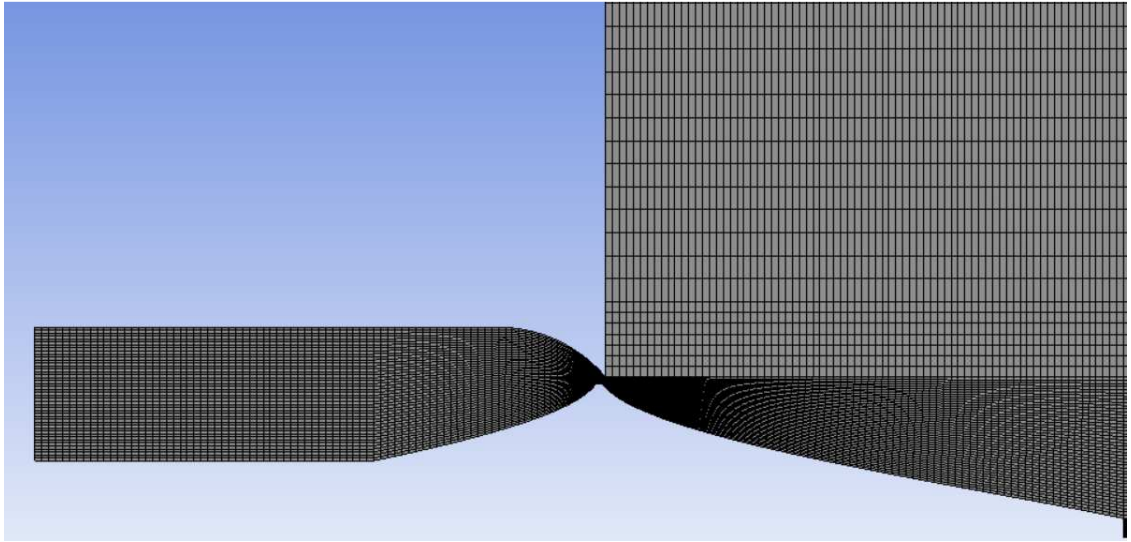


Fig. 57. Close up view of meshing topology.

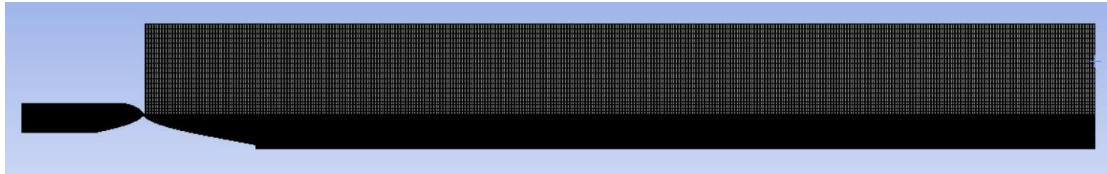


Fig. 58. Overall spike and flow field meshing topology.

The nozzle systems' general settings were set to a density-based, steady-state solver with a K-Epsilon RNG model, as stated in Table 29. The density-based and steady-solver are particularly useful for high-speed compressible fluids, making them particularly useful for analyzing the nozzle system. Ideal air was used as both the propellant and ambient fluid in the analysis due to air possessing a similar gamma to that of hydrogen

gas, thus, simplifying the total simulation. The K-Epsilon RNG model is a form of the standard K-epsilon model; however, it is based on the statistical technique of renormalization group theory and incorporates the following refinements. [48]

1. An additional term in the equation that improves accuracy
2. The effect of swirl turbulence is included
3. Includes an analytical formula for turbulent within the Prandtl–Meyer equation

Table 29
Nozzle System Analysis: General Settings

General Settings: Aerospike Case	
Conditions	Settings
General Solver	Density-Based
Simulation State	Steady State
Velocity Formulation	Absolute
Geometric settings	Axisymmetric about the X-axis
Energy equation	On
Viscous Model	K-epsilon RNG
Fluid Model	Air (Ideal Gas)

The nozzle system had boundary conditions set to reflect the operating conditions of the NTPS and set in a static outflow environment. The nozzle inlet conditions reflect the annulus reactor system's exiting conditions, such that the propellant pressure ranges from 4.1-6.9 MPa, as seen in Table 30. The temperature of the incoming flow from the annulus reactor was set to 3000 K. The outlet conditions were set to reflect the ambient pressure and temperature conditions expected at operating conditions, such as ambient air pressure ranging from 500-101,325 Pa.

Table 30
Nozzle System Analysis: Boundary Conditions

Boundary Conditions		
Settings	Inlet (Pressure)	Outlet (Pressure)
Gauge Pressure	4-6.9 MPa	500-101325 Pa
Operating Pressure	0 Pa	0 Pa
Total Temperature	300 K	300 K
Supersonic gauge pressure	5000-101325 Pa	N/A
Free Stream Temperature	300 K	300 K

The nozzle system's solution methods utilize similar conditions as that of the annulus reactor system analysis, of which the settings can be seen in Table 31. Second-Order Upwind formulation was utilized as while the first-order discretization generally yields better convergence. However, Second-Order Upwind formulation provided greater accuracy in the results, given that a structured mesh was utilized.

Table 31
Nozzle System Analysis: Solution Methods

Solution Methods	
Settings	Type
Formulation	Implicit Formulation
Flux type	Roe-FDS
Gradient	Least Squares Cell-Based
Flow	Second-Order Upwind

Like the annulus reactor system analysis, a grid independence study was conducted to generate several independent meshes in ANSYS Fluent and test the results from each against the primary case. Through the independence study, it was found that much like the annulus reactor system analysis, there is a minimum of approximately 85000 nodes

for the simulation to exhibit the desired heat transfer and flow properties, as seen in Table 32. Every simulation was conducted to the standard simulation accuracy convergence of three orders of magnitude or greater. [48]

Table 32
Nozzle System Analysis: Solution Initialization

Solution Initialization	
Settings	Type
Initialization Method	Standard Initialization
Computation Reference	From All Zones
Reference Frame	Relative to Cell Zone
Number of Iterations	8000
Minimum nodes	85000
Y+	32.8

In order to ascertain the anatomy of flow exiting the nozzle, the nozzle system was tested at varying internal and ambient conditions that reflect the desired nominal operating parameters. The first iteration involved the nozzle system operating at 4.1 MPa at 1 atm, reflecting the nominal operating conditions at earth sea level. The first iteration allowed for the establishment of the benchmark behavior of the flow exiting the nozzle relative to the related shock formation. Fig. 59 displays the Mach number contour of the initial test, showcasing the exit Mach of 4.16. Fig. 60 displays the following regions' formation within the exhaust plume, the outer jet boundary, envelope shock, recirculation zone, trailing shock, and expansion zone. The formation and position of these characteristics are critical in determining the efficiency of the nozzle design. Thus, the presence and location of these characteristics confirm the nozzles' altitude compensation capability.

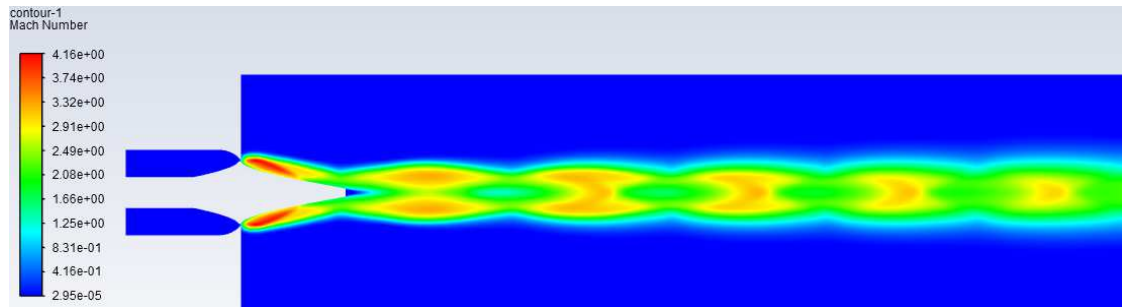


Fig. 59. Mach contours with a chamber pressure of 4.1 MPa at 1 atm.

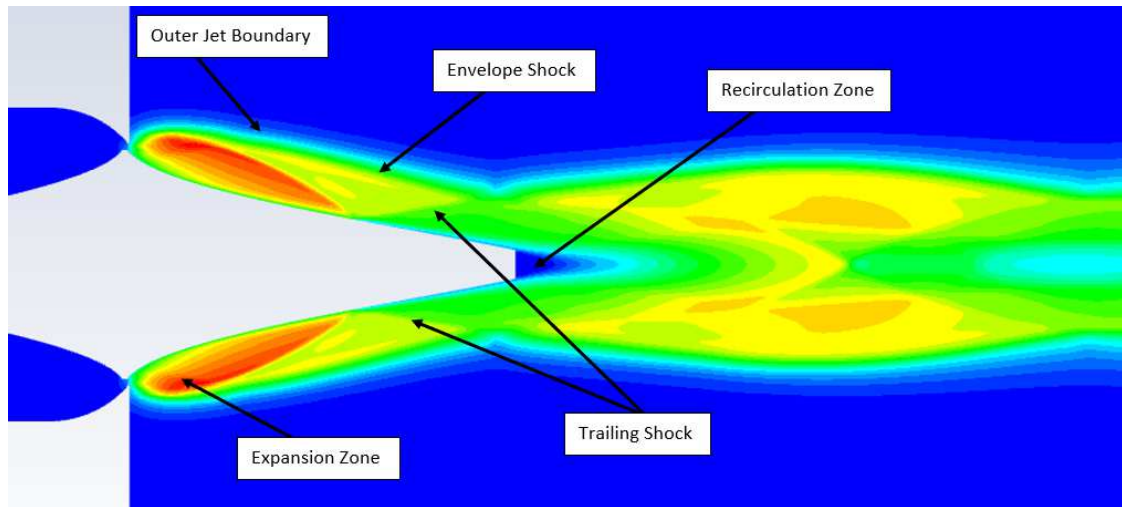


Fig. 60. Anatomy of the aerospike exhaust plume.

The second test iteration of the nozzle system was similar to that of the first; however, the operating pressure was increased to 5.1 MPa, and the incoming flow was increased to the nominal operating temperature of 3000 K. The second test iteration allows the understanding of how the nozzle will perform and behave under high pressure and heat conditions incoming from the annulus reactor system. The increase in pressure and temperature resulted in the increase of the exit Mach number from 4.16 to 4.56. The

increase in Mach number resulted in the flow's detachment following the trailing shock along the nozzle spike. Fig. 61 and 62 depict the Mach contour from the second test iteration along with the temperature contours of the nozzle exhaust plume.

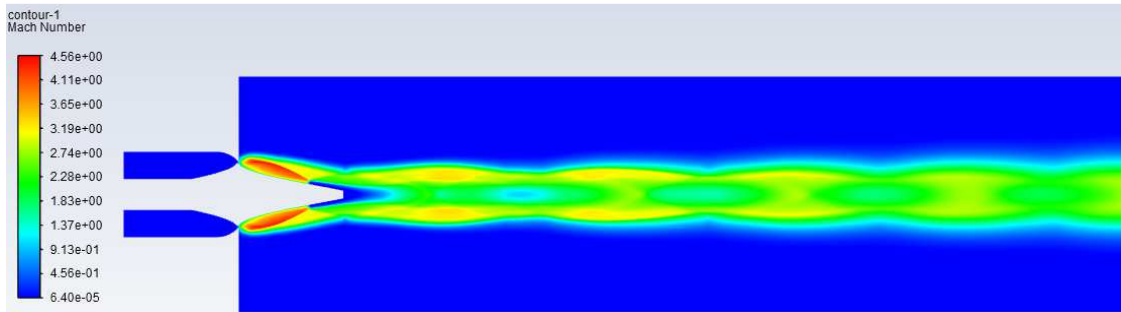


Fig. 61. Mach contours with a chamber pressure of 5.1 MPa at 1 atm.

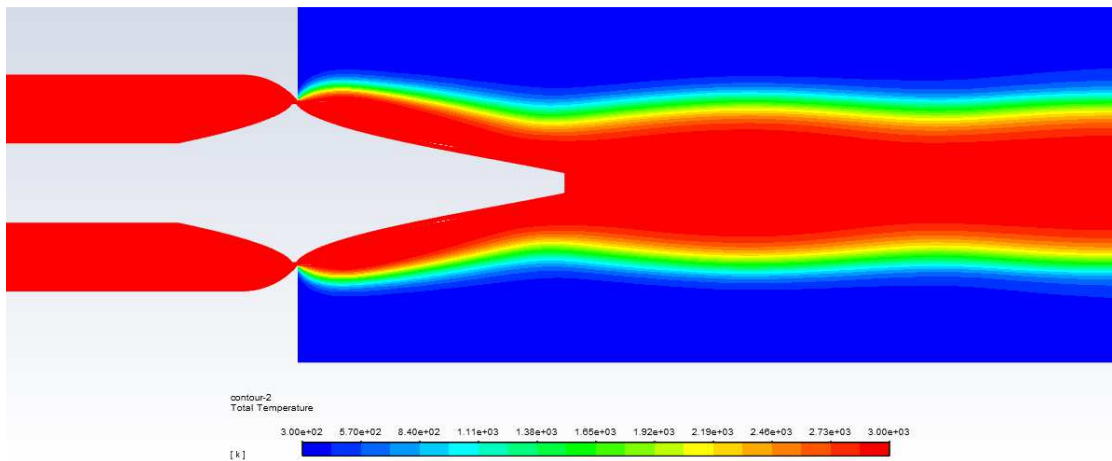


Fig. 62. Temperature contours of the nozzle exhaust plume.

The final test iteration was that of the nozzle system operating under near-vacuum conditions. The incoming operating conditions of the nozzle remained the same from the second test iteration. However, the ambient conditions were set to 5000 Pa, which is the lower limit of the ANSYS software being used. The near-vacuum test iteration was

necessary to determine the nozzles' capability to compensate for changes in ambient pressure conditions and characterization of the flow anatomy under such conditions, as depicted in Fig. 63.

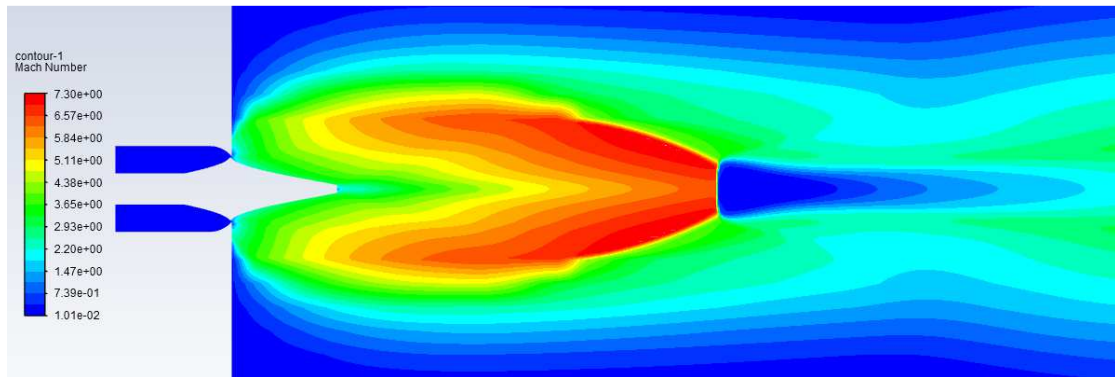


Fig. 63. Mach contours in near-vacuum conditions at a P_c of 5.1 MPa.

Following the data acquisition from each of the simulations, calculations were performed to verify the information. The utilization of Equation 23 allows for calculating the propellant's exit velocity based on gas properties, temperature, and pressure. Using information from the first test iteration, the Nuclear Thermal Propulsion System achieved an exit velocity of 7622.3 m/s while using air as the propellant, as stated previously. The exit velocity value acquisition was necessary to acquire the equivalent velocity from Equation 24 below. Knowing the mass flow rate to be 129 kg/s and the pressure conditions and the nozzle system's exit area allowed for the determination of the equivalent velocity to be 8746.46 m/s. By combining the information from Equations 23 and 24 into Equations 25 and 26, the sea-level Isp of the Nuclear Thermal Propulsion System was determined to be 892s with a thrust of 1.128 MN. Therefore, the vacuum

thrust and Specific Impulse are expected to be substantially more, and the use of hydrogen as the propellant will also cause the Specific Impulse to increase substantially.

$$v_e = \sqrt{\left(\frac{2\gamma}{\gamma-1} \cdot \frac{R}{M_w} \cdot T_c \cdot \left[1 - \left(\frac{p_e}{p_c}\right)^{\frac{\gamma-1}{\gamma}}\right]\right)} \quad (23)$$

$$V_{eq} = v_e + \frac{(p_e - p_a) \cdot A_e}{\dot{m}} \quad (24)$$

$$I_{sp} = \frac{V_{eq}}{g_0} \quad (25)$$

$$F_T = \dot{m} \cdot v_e + (p_e - p_a) \cdot A_e \quad (26)$$

8 DISCUSSION

The resolution level at which the system and subsystem analysis was conducted yielded similar elements to previous generations of nuclear thermal rocket engines. Simultaneously, the system analysis also revealed that a nuclear thermal rocket engine is capable of being reconfigured for an aerospike nozzle without sacrificing key elements. The reconfiguring of the core into a separated fuel puck system produced evidence that the core has the possibility of a wide range of configurations. A theoretical possibility is that the nuclear core could be made smaller while still maintaining equivalent performance levels to that of the current configuration.

The computational fluid dynamics analysis of the annulus reactor and nozzle systems was able to characterize the performance characteristics. In the annulus reactor case with the separated and non-separated fuel rods, configurations produced similar results in regards to the temperature increase of the hydrogen fuel. However, it was observed that across all test iterations and boundary conditions, the separated puck configuration did not yield higher propellant exit temperature values as predicted in the initial design phase. Based on the data, it was determined that the non-separated configuration exhibited exit temperatures close to or exceeding that of our benchmark case. This discrepancy in simulation test performance and predicted performance is likely due to the laminar flow-induced within the separated puck model due to the sequential simulation run configuration. The sequential simulations resulted from the limitation of the computational fluid dynamic software accessible at the time of the analysis. The turbulence between each of the separated fuel pucks lost in this analysis would result in

more significant fluid interaction and heat transfer. Additionally, it was noted that the temperature increase attenuated towards the end of all simulations, indicating that longer fuel rod designs may prove redundant; thus, a noticeably smaller system than initially conceived may be achievable.

9 FUTURE WORK

The research going forward would be on the refinement of the design and analysis of the Nuclear Thermal Propulsion System. The ongoing research would be centered around the propellant feed system and coolant system, with more refinement in the CFD analysis of both the annulus reactor and nozzle systems. The propellant feed system will need to be designed and dimensionalized to understand the size of the NTPS fully. Once the propellant feed system's parameters are solidified, the system will need to be verified through CFD analysis, similar to that of the annulus reactor and the nozzle systems. The coolant system will need to have an extensive CFD analysis to verify and refine the heating and cooling channels within the NTPS. A secondary coolant system CFD analysis will need to be conducted to verify the system will be able to adequately cool the nozzle system while simultaneously gaining the needed energy to drive and heat the propellant feed system. The CFD analysis on the annulus reactor system will need to be revalidated using a non-student version of ANSYS to allow for higher node counts and a larger number of distinct bodies under analysis at one time. A revalidation and refinement of the CFD analysis conducted on the nozzle system are needed, using a non-student version of ANSYS that facilitates hydrogen as a propellant and can aid in establishing the vacuum performance of the NTPS. Lastly, a full system CFD analysis will be needed after completing the four primary systems; this CFD analysis will be the full system validation of the NTPS and establish the full extent of the Nuclear Thermal Propulsion System's capabilities.

10 CONCLUSION

With the systems and computational fluid dynamic analysis performed, it can be concluded that a nuclear thermal propulsion system coupled with an aerospike nozzle can significantly outperform the capabilities of modern high thrust rocket engines. The relative simplicity of the system compared to conventional chemical rockets of similar thrust capabilities, along with the significant improvements in both fuel usage and specific impulse, are strong indicators of the efficacy of the proposed system. The computational fluid dynamic analysis of the Nuclear Thermal Propulsion System components produced data that indicate that the annulus reactor design has the possibility of not only producing higher propellant temperatures but doing so with noticeably less fissile material than that of prior NTR systems. The analysis performed regarding the nozzle system shows that the benefits of an altitude compensating system as a means of accelerating the heated propellant exiting the annulus reactor system stands to produce a much more efficient system than that of a convergent-divergent nozzle. Additionally, it allows for the engine's operation in varied environments from Earth and Martian atmospheric conditions to the vacuum of space, lending a great versatility in mission deployment for the Nuclear Thermal Propulsion System. Implementing such a propulsion system in future exploratory missions would ensure the capability of long planetary journeys in a shorter period and allow them with less fuel consumed. Thus, the proposed Nuclear Thermal Propulsion System would allow humanity to lift more and go further in space than ever before.

BIBLIOGRAPHY

- [1] J. D. Mattingly, *Elements of Propulsion : Gas Turbines and Rockets*. Reston, Virginia: American Institute of Aeronautics and Astronautics, 2012.
- [2] D. H. Huang and D. K. Huzel, *Modern Engineering for Design of Liquid-Propellant Rocket Engines*. American Institute of Aeronautics and Astronautics, 1992.
- [3] P. J. Nolan, *Fundamentals of Modern Physics*. Physics Curriculum & Instruction, 2014.
- [4] P. Papadopoulos, “Advanced Spacecraft Propulsion A.E. 267 (Class Notes).” Periklis Papadopoulos at San Jose State University, San Jose, pp. 1–66, 2019.
- [5] J. A. Dewar, *To the End of the Solar System: The Story of the Nuclear Rocket*. Collector’s Guide Publishing, Inc., 2008.
- [6] D. R. Koenig, *Experience Gained From The Space Nuclear Rocket Program (Rover)*. Los Alamos, New Mexico: Los Alamos National Laboratory, 1986.
- [7] M. Wade, “Titan 1-2,” *www.astronautix.com*, 2019. [Online]. Available: <http://www.astronautix.com/t/titan1-2.html>. [Accessed: 29-Sep-2019].
- [8] W. H. Robbins and H. Finger, *An Historical Perspective of the NERVA Nuclear Rocket Engine Technology Program*, no. July 1991. North Olmsted, Ohio: American Institute of Aeronautics and Astronautics, 1991.
- [9] S. Gunn, *Nuclear propulsion- Historical Perspective*. Moorpark, CA: Elsevier, 2001.
- [10] K. Benensky and A. Ray, *Summary of Historical Solid Core Nuclear Thermal Propulsion Fuels*. Pennsylvania State University, 2013.
- [11] M. Dayah, “Dynamic Periodic Table,” *www.ptable.com*, 2017. [Online]. Available: <https://www.ptable.com/>. [Accessed: 30-Sep-2019].
- [12] M. Wade, “RD-0410,” *www.astronautix.com*, 2019. [Online]. Available: <http://www.astronautix.com/r/rd-0410.html>. [Accessed: 30-Sep-2019].
- [13] M. Wade, “Russian Mars Propulsion - Nuclear Thermal,” *www.astronautix.com*, 2019. [Online]. Available: <http://www.astronautix.com/r/russianmarsnuclearthermal.html>. [Accessed: 30-Sep-2019].

- [14] J. Feldscher, “Push for nuclear power in space sets off proliferation debate,” *Politico*, 2019. [Online]. Available: <https://www.politico.com/story/2019/09/27/nuclear-power-nasa-mars-alan-kuperman-q-and-a-1510896>. [Accessed: 18-Nov-2019].
- [15] M. M. Vucelic, M. A. Faget, D. K. Slayton, O. Maynard, G. Low, and C. Kraft, *CSM/LM Spacecraft Operational Data Book*. National Aeronautics and Space Administration, 1970.
- [16] D. Woods, J. K. Turhanow, and L. Waugh, “The Apollo 13 Flight Journal - Index Page,” 2020. [Online]. Available: <https://history.nasa.gov/afj/ap13fj/index.html>. [Accessed: 01-Nov-2020].
- [17] “Welcome to Shuttle-Mir The U.S. and Russia Share History’s Highest Stage,” *www.history.nasa.gov*. [Online]. Available: <https://history.nasa.gov/SP-4225/diagrams/apollo/apollo-diagram.htm>. [Accessed: 01-Nov-2020].
- [18] D. Marin, “Apollo Spacecraft Diagram,” *danielmarin.naukas.com*, 2019. [Online]. Available: <https://danielmarin.naukas.com/2019/06/13/sexta-entrevista-en-el-podcast-de-la-serie-lunar/sdsdd-2/>. [Accessed: 16-Nov-2019].
- [19] P. D. Wooster, R. D. Braun, J. Ahn, and Z. R. Putnam, “Trajectory Options for Human Mars Missions.”
- [20] R. A. Braeunig, “Basic of Space Flight: Interplanetary Flight,” *www.braeunig.us*, 2013. [Online]. Available: <http://www.braeunig.us/space/interpl.htm>. [Accessed: 11-Nov-2019].
- [21] J. V Bowles, L. C. Huynh, V. M. Hawke, and X. J. Jiang, *Mars Sample Return: Mars Ascent Vehicle Mission & Technology Requirements*. Moffett Field, CA: National Aeronautics and Space Administration, 2013.
- [22] B. G. Drake, J. D. Baker, S. J. Hoffman, D. Landau, and S. A. Voels, “Alternative Strategies for Exploring Mars and the Moons of Mars,” 2010. [Online]. Available: <https://ntrs.nasa.gov/search.jsp?R=20120009026>. [Accessed: 01-Nov-2019].
- [23] D. P. Stern, “Flight to Mars: How Long? And along what path?,” *National Aeronautics and Space Administration*, 2004. [Online]. Available: <https://www.spod.gsfc.nasa.gov/stargaze/Smars1.htm>. [Accessed: 28-Oct-2019].
- [24] E. Musk, “Starship Update,” *SpaceX*, 2019. [Online]. Available: <https://www.youtube.com/watch?v=sOpMrVnjYeY>. [Accessed: 17-Nov-2019].

- [25] “Falcon Heavy | SpaceX,” *SpaceX*. [Online]. Available: <https://www.spacex.com/falcon-heavy>. [Accessed: 17-Nov-2019].
- [26] G. C. Marshall, “National Aeronautics and Space Administration Liftoff Weights & Sizes Payload Thrust/Power Propulsion,” *National Aeronautics and Space Administration*, 2017. [Online]. Available: https://www.nasa.gov/sites/default/files/atoms/files/sls_fact_sheet_final_10112017.pdf. [Accessed: 17-Nov-2019].
- [27] N. Hall, “Thrust to Weight Ratio,” *National Aeronautics and Space Administration*, 2015. [Online]. Available: <https://www.grc.nasa.gov/WWW/K-12/airplane/fwrat.html>. [Accessed: 18-Nov-2019].
- [28] W. J. Larson and J. R. Wertz, *Space Mission Analysis and Design*, Third. Kluwer Academic Publishers and Microcosm Press, 1995.
- [29] P. Papadopoulos, “Advanced Space System Engineering A.E. 210 (Class Notes).” Periklis Papadopoulos at San Jose State University, San Jose, CA, 2018.
- [30] S. J. Kapurch and N. E. Rainwater, *NASA Systems Engineering Handbook*, First. Hanover, MD: National Aeronautics and Space Administration, 2007.
- [31] E. Britannica, “Axial flow centrifugal pump,” *www.britannica.com*. [Online]. Available: <https://www.britannica.com/technology/axial-flow-centrifugal-pump>. [Accessed: 13-Dec-2019].
- [32] E. Britannica, “Centrifugal pump | Britannica,” *www.britannica.com*. [Online]. Available: <https://www.britannica.com/technology/centrifugal-pump>. [Accessed: 13-Dec-2019].
- [33] T. Mai, “Technology Readiness Level,” *National Aeronautics and Space Administration*, 2012. [Online]. Available: https://www.nasa.gov/directorates/heo/scan/engineering/technology/txt_accordion1.html. [Accessed: 13-Dec-2019].
- [34] S. V. Gunn and C. Dunn, *Dual Turbopump Liquid Hydrogen Feed System Experience*. Canoga Park, CA: Rocketdyne, 1967.
- [35] C. Dunn and S. V. Gunn, “Feed System and Nozzles for Phoebus Reactor Experiments,” *J. Spacecr. Rockets*, vol. 6, pp. 769–777, 1969.
- [36] R. R. Gouw, *Nuclear Design Analysis of Square-Lattice Honeycomb Space Nuclear Rocket Engine*. University of Florida, 2000.

- [37] S. H. Nam, P. Venneri, Y. Kim, J. I. Lee, S. H. Chang, and Y. H. Jeong, “Innovative concept for an ultra-small nuclear thermal rocket utilizing a new moderated reactor,” *Nucl. Eng. Technol.*, vol. 47, pp. 678–699, 2015.
- [38] J. Plancher, *Thermal and Fluid Design Analysis of a Square Lattice Honeycomb Nuclear Rocket Engine*. University of Florida, 2002.
- [39] R. Gouw and J. Plancher, *Development of a Robust Tri-Carbide fueled Reactor for Multi-Megawatt Space Power and Propulsion Applications*. Gainesville, FL: University of Florida, 2004.
- [40] J. Sapir and J. D. Orndoff, *Neutronics of the Phoebus 2 reactor*. Los Alamos, New Mexico: Los Alamos Scientific Laboratory of the University of California, 1970.
- [41] J. Hennessy and D. Patterson, *Computer Architecture : A Quantitative Approach*, Fourth Edi. Elsevier, 2007.
- [42] A. Marks, “Physics of Uranium and Nuclear Energy,” *www.world-nuclear.org*, 2018. [Online]. Available: <https://www.world-nuclear.org/information-library/nuclear-fuel-cycle/introduction/physics-of-nuclear-energy.aspx>. [Accessed: 24-Mar-2020].
- [43] N. K. Kumar, M. Gopalsamy, D. Antony, R. Krishnaraj, and C. B. V. Viswanadh, *Design and Optimization of Aerospike nozzle using CFD*. IOP Conference Series: Materials Science and Engineering, 2017.
- [44] R. Masuda, *Optimal Design of Annular Aerospike Engine Nozzle*. California State University. Long Beach, 2002.
- [45] D. J. Grieb, *Design and Analysis of a Reusable N₂O-Cooled Aerospike Nozzle for Labscale Hybrid Rocket Motor Testing*. San Luis Obispo, CA: California Polytechnic State University, 2012.
- [46] K. Samadzadeh, “Supercritical Fluids - Chemistry LibreTexts,” *University of California Davis*, 2020. [Online]. Available: [https://chem.libretexts.org/Bookshelves/Physical_and_Theoretical_Chemistry_Textbook_Maps/Supplemental_Modules_\(Physical_and_Theoretical_Chemistry\)/Physical_Properties_of_Matter/States_of_Matter/Supercritical_Fluids](https://chem.libretexts.org/Bookshelves/Physical_and_Theoretical_Chemistry_Textbook_Maps/Supplemental_Modules_(Physical_and_Theoretical_Chemistry)/Physical_Properties_of_Matter/States_of_Matter/Supercritical_Fluids). [Accessed: 08-May-2020].

- [47] P. M. Sforza, *Theory of Aerospace Propulsion*, Second Edi. Elsevier, 2017.
- [48] “Ansys Fluent,” 2006. [Online]. Available:
<https://www.ansys.com/products/fluids>.
- [49] J. L. Finseth, *Overview of Rover Engine Tests: Final Report*. Huntsville, AL:
National Aeronautics and Space Administration, 1991.

APPENDIX

The following four tables, 33-36, are the critical nomenclature used throughout the above work.

Table 33
Appx. Symbol Nomenclature

Symbol	Definition	Units (SI)
A	Area	m ²
C _F	Thrust Coefficient	-----
D _A	Die Area	m ²
D _{PW}	Dies Per Wafer	-----
g	Acceleration of Gravity	m/s
H ₂	Hydrogen Gas	
I _{sp}	Specific Impulse	sec.
M	Mach Number	-----
M	Mass	kg
\dot{m}	Mass Flow Rate	kg/s
P	Pressure	pa
\mathbb{R}	Gas Constant	J/kg K
t	Time	sec.
T	Temperature	K
W _D	Wafer Diameter	m
Δv	Change in velocity	km/s
L	Length	m
r	Radius	m

Table 34
Appx. Greek Symbols Nomenclature

Greek Symbols	Definition	Units (SI)
δ	Deadweight ratio	-----
γ	Specific Heat ratio	-----
ν	Prandtl -Meyer Angle	-----

Table 35
Appx. Subscripts and Superscripts Nomenclature

Subscripts and Superscripts	Definition	Units (SI)
() [*]	Throat	-----
() _a	Atmospheric	-----
() _{bo}	Burn out	-----
() _c	Chamber	-----
() _e	Exit	-----
() _{inf}	Infinity	-----
() _m	Mars	-----
() _o	Initial	-----
() _p	Propellant	-----
() _{pl}	Payload	-----
() _w	Molecular	-----
() _{cn}	Convergent Nozzle Section	-----
() _{NS}	Nozzle Spike Section	-----
() _i	Maximum Nozzle Spike	-----
() _T	Nozzle Truncation	-----
() _t	Nozzle Throat	-----
() _{AC}	Cowling Convergent Section	-----

Table 36
Appx. Acronym Nomenclature

Acronyms	Definition	Units (SI)
C	Carbon	-----
CAD	Computer-Aided Design	-----
CFD	Computational Fluid Dynamics	-----
ICBM	Intercontinental Ballistic Missile	-----
LEO	Low Earth Orbit	-----
LMO	Low Mars Orbit	-----
MR	Vehicle Mass Ratio	-----
NASA	National Aeronautics and Space Administration	-----
Nb	Niobium	-----
NERVA	Nuclear Engine for Rocket Vehicle Application	-----
NTPS	Nuclear Thermal Propulsion System	-----
NTR	nuclear thermal rocket engine	-----
SDPD	Singular Direct Parallel Drive Propellant Feed System	-----
Ta	Tantalum	-----
U	Uranium	-----
USAF	The United States Air Force	-----
W	Tungsten	-----
Zr	Zirconium	-----